Nucleosynthesis of lighter heavy elements in neutrino-driven winds

Nukleosynthese von leicht schweren Elementen in neutrinogetriebenen Winden
Zur Erlangung des Grades eines Doktors der Naturwissenschaften (Dr. rer. nat.)
genehmigte Dissertation von M.Sc. Julia Barbara Erika Bliss, geb. in Offenbach am Main
Tag der Einreichung: 17. Juli 2017, Tag der Prüfung: 16. Oktober 2017

1. Gutachten: Prof. Dr. Almudena Arcones Segovia
2. Gutachten: Prof. Dr. Hendrik Schatz

TECHNISCHE
UNIVERSITÄT
DARMSTADT

Fachbereich Physik
Theoretische Astrophysik

Nucleosynthesis of lighter heavy elements in neutrino-driven winds
Nukleosynthese von leicht schweren Elementen in neutrinogetriebenen Winden

Genehmigte Dissertation von M.Sc. Julia Barbara Erika Bliss, geb. in Offenbach am Main

1. Gutachten: Prof. Dr. Almudena Arcones Segovia
2. Gutachten: Prof. Dr. Hendrik Schatz

Tag der Einreichung: 17. Juli 2017
Tag der Prüfung: 16. Oktober 2017

Darmstadt 2018 — D 17

Bitte zitieren Sie dieses Dokument als:
URN: urn:nbn:de:tuda-tuprints-75691
URL: http://tuprints.ulb.tu-darmstadt.de/7569

Dieses Dokument wird bereitgestellt von tuprints,
E-Publishing-Service der TU Darmstadt
http://tuprints.ulb.tu-darmstadt.de
tuprints@ulb.tu-darmstadt.de

Ad astra per aspera et per ludum.

Abstract

Neutrino-driven winds following core-collapse supernova explosions are an exciting astrophysical site for the formation of the lighter heavy elements between strontium up to (possibly) silver. Observations of very old stars, so-called ultra-metal poor stars, show scatter in the abundances of these elements, whereas they exhibit a robust abundance pattern for the elements beyond barium. Therefore, the origin of the lighter heavy elements in the universe is associated to the r-process and at least one additional process. Although it is not clear if neutrino-driven winds are neutron- or proton-rich, the necessary astrophysical conditions to synthesize lighter heavy elements are already found in wind simulations. Here, we assume that the missing component corresponds to the weak r-process occurring in slightly neutron-rich winds. Despite the fast progress in theoretical and experimental nuclear astrophysics in the last years, the astrophysical as well as the nuclear physics uncertainties are still very large. In this thesis, we address the impact of the astrophysics and nuclear physics uncertainties on the wind nucleosynthesis. We present possible astrophysical conditions and key reactions in neutron-rich winds.

In the first part of this thesis, we quantify the astrophysical uncertainties in neutrino-driven winds. A systematic study using trajectories from hydrodynamic simulations is from a computational point of view not feasible. In addition, there are still uncertainties in the core-collapse supernova mechanism and the wind evolution. Thus, we calculate steady-state trajectories and investigate the nucleosynthesis. In the final abundances, we identify different nucleosynthesis groups by the different neutron, alpha, and seed abundances. The groups mainly distinguish in the position of the nucleosynthesis path relative to the valley of stability. Each group exhibits characteristic abundance peaks. We show that the abundance patterns are only sensitive to specific reactions if the nucleosynthesis path overcomes the neutron shell closure at $N = 50$.

In the second part of this thesis, we investigate the impact of nuclear physics uncertainties on the wind nucleosynthesis with our main focus on the (α, n) reactions. The (α, n) reactions are essential to redistribute matter and to reach heavier nuclei in neutron-rich winds. The uncertainties of the (α, n) reaction rates arise from the statistical model and its nuclear physics input, mainly the alpha optical potential. In a first sensitivity study, we vary the (α, n) reaction rates by constant factors, which are within their uncertainties, and find a critical influence on the nucleosynthesis evolution. Therefore, we perform a Monte Carlo sensitivity study within the astrophysical uncertainties studied in the first part of this thesis to identify individual critical (α, n) reactions. The key (α, n) reactions are identified by analyzing the correlations between reaction rate modifications and resulting abundance changes. We find that the uncertainties of the $^{82}\mathrm{Ge}(\alpha, \mathrm{n})$, $^{84}\mathrm{Se}(\alpha, \mathrm{n})$, and $^{85}\mathrm{Se}(\alpha, \mathrm{n})$ reaction rates critically affect the nucleosynthesis, and especially the abundances for nuclei with atomic numbers $Z = 36 - 39$. The reduction of these rate uncertainties will significantly decrease the influence of nuclear physics uncertainties on the wind nucleosynthesis. Since the nucleosynthesis path proceeds close to the valley of stability, these reactions can be measured with new radioactive beam facilities like FRIB or FAIR in the near future. Once the nuclear physics uncertainties are reduced by experiments, observations from very old stars will constrain the astrophysical conditions in neutrino-driven winds and improve our understanding of core-collapse supernovae and neutrino-driven winds.

Zusammenfassung

Neutrinogetriebene Winde von Kernkollaps-Supernova-Explosionen sind ein vielversprechendes astrophysikalisches Szenario für die Synthese der leicht schweren Elemente zwischen Strontium und (wahrscheinlich) Silber. Beobachtungen von den ältesten Sternen zeigen Abweichungen in den Häufigkeiten dieser Elemente auf, wohingegen ein universell auftretendes Muster für Elemente schwerer als Barium beobachtet wird. Deshalb wird der Ursprung der leicht schweren Elemente im Universum mit dem r-Prozess und mindestens einem zusätzlichen astrophysikalischen Prozess in Verbindung gebracht. Obwohl nicht klar ist, ob neutrinogetriebene Winde neutronen- oder protonenreich sind, werden die notwendigen astrophysikalischen Bedingungen zur Produktion der leicht schweren Elemente bereits in Windsimulationen gefunden. Wir nehmen im Rahmen dieser Arbeit an, dass die fehlende Komponente der schwache r-Prozess ist, der in leicht neutronenreichen Winden auftritt. Trotz des rasanten Fortschritts in der theoretischen und experimentellen Astrophysik in den letzten Jahren sind die Unsicherheiten in den astrophysikalischen Bedingungen und in den kernphysikalischen Modellen immer noch sehr groß. Im Rahmen dieser Arbeit erforschen wir die Auswirkung der Unsicherheiten in den astrophysikalischen Bedingungen und in den kernphysikalischen Modellen auf die Nukleosynthese in neutrinogetriebenen Winden. Wir präsentieren mögliche Häufigkeitsmuster und Schlüsselreaktionen.

Im ersten Teil dieser Arbeit untersuchen wir systematisch die astrophysikalischen Bedingungen in leicht neutronenreichen Winden. Eine systematische Studie, die auf Trajektorien von hydrodynamischen Simulationen basiert, ist derzeit zu rechenintensiv. Darüber hinaus gibt es noch Unsicherheiten im Kernkollaps-Supernova-Mechanismus und der Entwicklung des neutrinogetriebenen Windes. Daher berechnen wir stationäre Windtrajektorien und analysieren die Nukleosynthese. In den Elementhäufigkeiten identifizieren wir verschiedene Nukleosynthesegruppen anhand der unterschiedlichen Neutronen, Alphateilchen- und Saatkernhäufigkeiten. Die Nukleosynthesegruppen unterscheiden sich hauptsächlich aufgrund der Fortentwicklung des Nukleosynthesepfades relativ zum Tal der Stabilität. Jede Nukleosynthesegruppe weist ein charakteristisches Häufikeitsmuster auf. Wir zeigen, dass die Häufigkeitsmuster nur sensitiv auf spezifische Reaktionen reagieren, falls der Nukleosynthesepfad die magische Neutronenzahl $N = 50$ überschreitet.

Im zweiten Teil dieser Arbeit erforschen wir den Einfluss der Unsicherheiten in den kernphysikalischen Modellen auf die Nukleosynthese im Wind mit dem Hauptaugenmerk auf (α, n) Reaktionen. Die (α, n) Reaktionen sind essentiell zur Umverteilung der Materie im neutrinogetriebenen Wind und zur Produktion schwererer Kerne. Die Unsicherheiten in den (α, n) Reaktionsraten gehen aus dem statistischen Modell zur Berechnung der Reaktionsraten sowie den kernphysikalischen Modellen zur Beschreibung der alpha-optischen Potentiale hervor. In einer ersten Sensitivitätsstudie werden die (α, n) Reaktionsraten mit konstanten Faktoren variiert, die die Unsicherheiten in den Reaktionsraten beschreiben. Wir erkennen, dass die Unsicherheiten in den (α, n) Reaktionsraten einen kritischen Einfluss auf die Entwicklung der Nukleosynthese haben. Deshalb führen wir eine Monte Carlo Sensitivitätsstudie zur Identifizierung einzelner kritischer (α, n) Reaktionen durch. Die (α, n) Schlüsselreaktionen werden durch die Analyse von den Korrelationen zwischen der Variation der Reaktionsraten und der daraus resultierenden Häufigkeitsänderungen identifiziert. Wir schlussfolgern, dass die Unsicherheiten in den $^{82}\mathrm{Ge}(\alpha, \mathrm{n})$, $^{84}\mathrm{Se}(\alpha, \mathrm{n})$, und $^{85}\mathrm{Se}(\alpha, \mathrm{n})$ Reaktionsraten einen entscheidenden Einfluss auf die Nukleosynthese und insbesondere auf die Häufigkeiten der Elemente mit Protonenzahl $Z = 36-39$ haben. Die Reduzierung der Unsicherheiten dieser Reaktionsraten wird den Einfluss der Unsicherheiten in kernphysikalischen Modellen auf die Nukleosynthese im neutrinogetriebenen Wind erheblich verringern. Da der Nukleosynthesepfad nahe dem Tal der Stabilität verläuft, können diese Reaktionen bereits in naher Zukunft mit neuen Beschleunigeranlagen wie FRIB oder FAIR gemessen werden.

Contents

List of Figures

List of Tables

1 Introduction and motivation

Where do nuclei and elements come from? This is one of the fundamental questions in nuclear astrophysics. Observations of the abundances in the solar system as well as observations of very old stars give us hints about the formation of the elements in the universe.

Burbidge *et al.* [1] and Cameron [2] laid the foundation for our understanding of the synthesis of the elements heavier than iron already in 1957. From the solar system abundances, Burbidge *et al.* [1] proposed that the heavy elements were formed by three distinct nucleosynthesis processes, which they named the r-, s-, and p-process. The rapid (*r*-) neutron capture process and the slow (*s*-) neutron capture process produce most of the nuclei heavier than iron. The astrophysical site for the r-process is not known but binary neutron star mergers (see, e.g., Refs. [3–5]) and magnetorotationally driven supernovae (see, e.g., Refs. [6, 7]) are the most promising scenarios. On the contrary, the astrophysical sites for the s-process are well known. The s-process occurs in AGB stars [8–10] and during the He- and C-burning phases of massive stars [11–13]. Furthermore, the p-process synthesizes the neutron-deficient nuclei that are bypassed by the s- and r-process. The neutron-deficient nuclei are probably produced by supernovae (see Ref. [14] and references therein).

Observations of very old stars, having incorporated the fingerprints of only a few nucleosynthesis events, show robust abundance patterns for the elements beyond Ba closely following the solar system r-process abundances (see, e.g., Ref. [15]). Consequently, the r-process must have occurred early in the universe and always behaves in the same way. This implies that the first stars were massive and evolved fast [16–21]. Moreover, very old stars exhibit a star-to-star scatter in the abundances of the elements between Sr and Ag [15, 22] which are also referred to as lighter heavy elements. Therefore, in addition to the r-process, at least one additional nucleosynthesis process or astrophysical site is required to explain the abundances of the lighter heavy elements in very old stars [17, 18, 20, 23]. The authors of Refs. [17, 18, 20, 23, 24] showed that neutrino-driven winds can contribute to the synthesis of the elements between Sr and Ag. Besides, the abundances of the lighter heavy elements in the solar system cannot be obtained by solely adding up the s- and r-process [25, 26]. The authors of Ref. [25] suggested that another primary process, which they named Lighter Element Primary Process (LEPP), contributed to the production of the lighter heavy elements, but they did not specify the astrophysical site. The LEPP can be a non-standard s-process in low-metallicity massive rotating stars (see Ref. [27] and references therein), or charged particle reactions [23, 28, 29] combined with a weak r-process [30] and/or the νp-process [31–33] which occur in neutrino-driven winds.

Neutrino-driven winds follow core-collapse supernova explosions. Core-collapse supernovae mark the end of the life of massive stars with at least eight solar masses and lead to the birth of neutron stars or stellar black holes. After a successful core-collapse supernova explosion, a hot proto-neutron star is born which cools down by neutrino emission. Some of the neutrinos deposit energy in the outer layers of the proto-neutron star which powers a mass outflow with supersonic velocity, the so-called neutrino-driven wind [34]. For a long time, it has been thought that the neutrino-driven wind is the host for the r-process [35], but recent simulations indicate that the conditions in the wind are not sufficient enough [36–39]. However, neutrino-driven winds are an exciting astrophysical site for the formation of the lighter heavy elements because the necessary conditions are already found in current simulations [40, 41].

Before we can conclude that neutrino-driven winds are the astrophysical site for the lighter heavy elements, the astrophysical and nuclear physics uncertainties need to be reduced because they can critically influence the nucleosynthesis in the wind.

The evolution of the astrophysical conditions in the wind varies for different supernova progenitors, explosion energies, anisotropic evolutions of the explosion, and during the time after the explosion (see, e.g., Refs. [36, 37, 39]). Moreover, there are still uncertainties in the core-collapse supernova mechanism [42–44] and the wind evolution [45].

The nuclear physics uncertainties mainly arise from the theoretical reaction rates entering in the nucleosynthesis calculations. In the absence of relevant reactions, most of the reaction rates are computed with theoretical reaction codes based on the statistical Hauser-Feshbach model [46]. Although the reaction codes have been cross-checked with available data from few experiments, the reliability of these codes, especially for nuclei further away from the valley of stability, is not known. In addition, the reaction codes exhibit important differences due to intrinsic technical aspects and nuclear physics inputs [47, 48].

This work deals with the astrophysics and nuclear physics uncertainties. We systematically study possible astrophysical conditions in neutron-rich winds. In order to reduce the nuclear physics uncertainties, we perform sensitivity studies within possible astrophysical conditions and motivate key reactions which influence the nucleosynthesis evolution in the wind. When experiments will have measured the required nuclear properties, nucleosynthesis studies, including relevant experimental data, combined with observations of very old stars will constrain the astrophysical conditions in the wind.

Since the nucleosynthesis path in the neutrino-driven wind evolves close to the valley of stability, the required experimental data will be accessible with new radioactive beam facilities like FAIR (Facility for Antiproton and Ion Research) or FRIB (Facility for Rare Isotope Beams) in the near future. Furthermore, more high resolution observations of very old stars are planned [49, 50]. Consequently, we are close to verify if neutrino-driven winds are the astrophysical site for the lighter heavy elements and therefore better understand neutrino-driven winds and core-collapse supernovae.

The astrophysical background which is necessary to understand neutrino-driven winds and the nucleosynthesis in neutrino-driven is described in Chapter 2. Since nuclear reactions are one of the key ingredients in nucleosynthesis calculations, we give an overview about nuclear reactions in astrophysics in Chapter 3. Afterwards, we study the astrophysical uncertainties in neutron-rich winds based on steady-state wind models and present typical abundance patterns (Chapter 4). In Chapter 5, we investigate the impact of nuclear physics uncertainties on the wind nucleosynthesis due to (α, n) reactions and motivate key which critically affect the nucleosynthesis. Finally, we summarize our results and conclude with an outlook (Chapter 6).

2 Astrophysical background

In this chapter, we will give an overview about the astrophysical background which is necessary to understand the formation of lighter heavy elements (i.e., Sr up to possibly Ag) in neutrino-driven winds. At the beginning, we will shortly describe the origin of elements from hydrogen to uranium (Sect. 2.1). This part follows the book of Ref. [51]. Clues about the formation of the elements in the universe are obtained from observations of very old stars (see Sect. 2.2 which is based on Refs. [15, 52]). These observations indicate that neutrino-driven winds from core-collpase supernovae could be important for the formation of the lighter heavy elements in the universe. Therefore, we will give a short description about core-collapse supernovae in Sect. 2.3 following Refs. [42, 53, 54]. Afterwards, we will focus on the neutrino-driven wind (Sect. 2.4). We will describe the wind dynamics (Sect. 2.4.1) and will give an overview about the nucleosynthesis in the wind (Sect. 2.5). The part about the neutrino-driven wind is based on Refs. [45, 55].

2.1 The origin of elements

The lightest nuclei, i.e., ^{2}H, ^{4}He and small portions of ^{3}H, ^{3}He, ^{7}Li, and ^{7}Be, were already formed in the Big Bang. They were synthesized in an interaction between the four fundamental forces during the first seconds of cosmic time (see, e.g., Ref. [56] for a review about Big Bang nucleosynthesis).

The elements up to the iron group are formed in nuclear burning phases in the interiors of stars by fusion reactions. An introduction to stellar evolution can be found, e.g., in Ref. [57]. Here, we only describe the evolution of massive stars with at least 8 $M_{\odot}$[1].

A massive star spends most of its lifetime burning hydrogen into helium. When the hydrogen in the center of the star is depleted, hydrogen burning continues in a shell around the He core. The core contracts under the influence of gravity and heats up until He is ignited. The new fuel stabilizes the star against its gravity and prevents further contraction. When the He fuel is consumed in the core, He burning continues in a shell beneath the H burning shell. Then, the core contracts until the temperature is high enough that C in the core is ignited. A massive star undergoes several burning stages which proceed similar to the ones described before. When the fuel of one burning phase is consumed, the star contracts under the influence of gravity until the temperature is large enough that the ash of the previous burning step is ignited and becomes the fuel of the next burning step. The burning phases take place in thin regions at the interface of different compositional layers. The burning stages of a massive star are: hydrogen burning, helium burning, carbon burning, neon burning, oxygen burning, and silicon burning (for further information see, e.g., Refs. [57, 58]). After the silicon burning phase, the formation of heavier elements does not release energy, but rather costs energy, and thus the star ends up with an iron core. Then, the star consists of several layers with different compositions and exhibits an onion-like structure (Fig. 2.1). From the core going to the surface, the star consists of Fe, Si, O, Ne, C, He, and H.

Due to the drastically increasing Coulomb barrier, nuclei beyond Fe cannot be synthesized by charged particle reactions. Since there is no Coulomb barrier for neutrons, it is reasonable to assume that the nuclei beyond iron are synthesized by neutron capture reactions on preexisting seed nuclei. Further hints are given by the solar system abundances which refer to the abundance distribution in the solar system at the time of its formation. The solar system abundances are obtained from observations of the photosphere and from the analysis of CI carbonaceous chondrites which are a special class of meteorites (for details how these abundances are received see, e.g., Refs. [59, 60]). Reference [1] already proposed in 1957 that several nucleosynthesis processes are required to explain the solar system abundances. Moreover, at least two different processes are necessary to explain the double-peak structure around $A \sim 130$ and $A \sim 200$ (see Fig. 2.2). These two processes are referred to as slow neutron capture process (s-process) and rapid neutron capture process (r-process) [1]. The s- and r-process differ in the time scales for beta decays and neutron capture reactions. Each of the two processes synthesizes about half of the elements beyond Fe.

The s-process is characterized by small neutron densities $n_{\mathrm{n}} \sim 10^{8}\ \mathrm{cm}^{-3}$ [64]. The time scale for beta decays is much shorter than for neutron capture reactions ($\tau_{\beta^-} \ll \tau_{(\mathrm{n},\gamma)}$) and therefore an unstable nuclide beta decays

---

[1] $M_{\odot} \approx 1.989 \cdot 10^{30}$ kg being the mass of the sun.

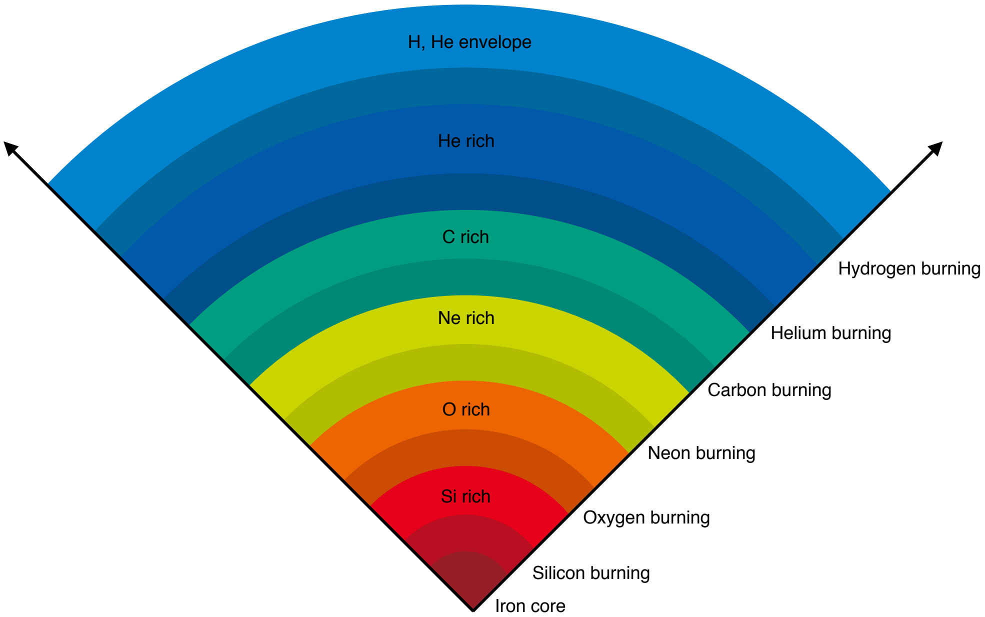

Figure 2.1: A massive star with at least 8 $M_\odot$ at the end of its lifetime. The star exhibits an onion-like structure. The different shell burning phases still occur. Since the binding energy per nucleon has it maximum at $A = 56$, the formation of heavier elements than iron does not release energy. Hence, iron is the final stage of the burning phases in massive stars. The figure is adapted from a figure by C. Mihos [61].

before it can capture a neutron. The s-process starts from some seed nuclei (mainly Fe-group nuclei) and runs along stability (see Fig. 2.3). Hence, most of the properties of the involved nuclei are known [65]. The s-process ends at ^{209}Bi which is the heaviest stable nuclide. Additional neutron captures produce radioactive nuclei which decay by alpha particle emission, and thus heavier nuclei cannot be synthesized. Due to the small neutron capture cross sections before the magic neutron numbers at $N = 50, 82, 126$, the abundances of ^{88}Sr, ^{138}Ba, and ^{208}Pb are large. This causes the large distinct double peaks in the solar system abundance pattern (Fig. 2.2). The s-process

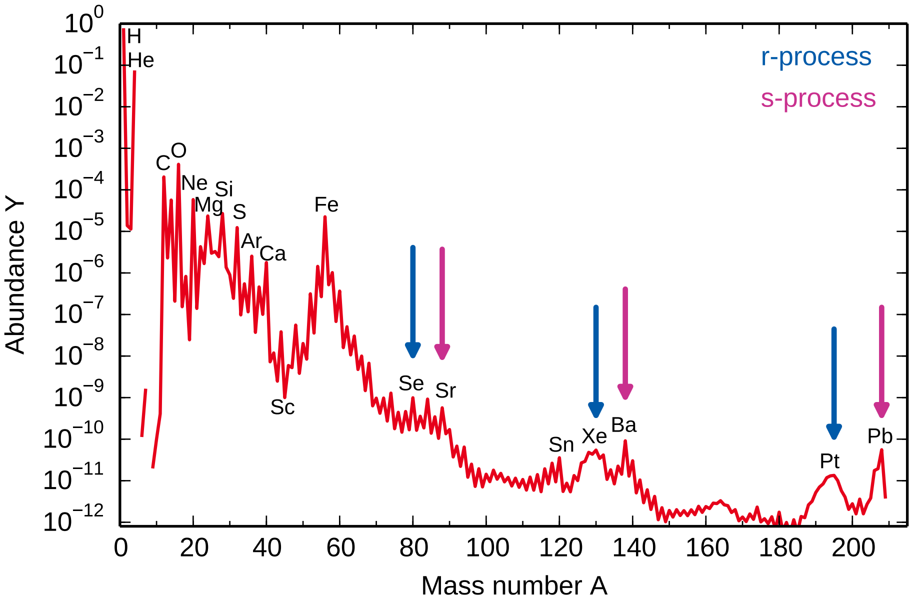

Figure 2.2: Abundances of the nuclei in the solar system at the time of its formation. The abundances are normalized to the number of silicon atoms (Si $= 10^6$). Narrow abundance peaks appear at $A \approx 84$, 138, and 208 which correspond to the neutron magic numbers of $N = 50$, 82, and 126. Broader abundance peaks occur roughly 10 mass units below. The data are taken from Ref. [62].

takes place in the He-burning layers of low-mass asymptotic giant branch (AGB) stars [8–10] and during the He- and C-burning phases of massive stars [11–13]. More information about the s-process are given in Ref. [65] and references therein.

On the contrary, the neutron densities are very large (i.e., $n_\mathrm{n} \gtrsim 10^{24} - 10^{28}$ cm^{-3} [66]) in the r-process. Thus, many successive neutron captures occur before a nucleus is reached that undergoes a beta decay before it captures a neutron ($\tau_{\beta-} \gg \tau_{(\mathrm{n},\gamma)}$). The nucleosynthesis path proceeds along short-lived nuclei close to the neutron drip line (see Fig. 2.3). For long neutron exposures, the r-process can reach the heaviest and neutron-rich isotopes for which the Coulomb barrier is so high that they decay by spontaneous, neutron-, or beta-induced fission. Fission occurs near $A_\mathrm{max} \approx 260$ and $Z_\mathrm{max} \approx 94$ [67, 68]. If the neutron density is still large enough, the fission fragments continue to capture neutrons and eventually give rise to a fission cycle [3, 4]. Once the neutron flux is exhausted, all neutron-rich nuclei undergo a sequence of beta decays along isobaric chains until a stable or very long-lived isotope is attained. The r-process synthesizes elements up to uranium. Since the nucleosynthesis path runs far away from the valley of stability, the properties of the involved nuclei are not known from experiments, and thus have to be estimated using theoretical nuclear models (see, e.g., Ref. [69]).

The large neutron density moves matter far away from stability to the neutron-rich side where the matter accumulates at the neutron magic numbers $N = 50, 82, 126$. Note that the accumulation of matter is correlated with a drop in the neutron separation energy near the neutron magic numbers which leads to a nucleosynthesis path vertically along isotones in the $N = 50, 82, 126$ regions. When the neutron flux is terminated, the neutron magic nuclei beta decay along isobaric chains until a stable nucleus is reached. The neutron magic numbers are at lower A, in contrast to the s-process where they are located close to stability. Consequently, the r-process abundance peaks at $A \sim 80$, $A \sim 130$, and $A \sim 195$ which are referred to as first, second, and third r-process peak, respectively, and are located at mass regions below the corresponding s-process abundance peaks (Fig. 2.2).

The astrophysical site for the r-process is still a mystery, even though the requirements on the site are well known. A possible astrophysical site has to provide very high neutron densities over a short time scale. In addition, the

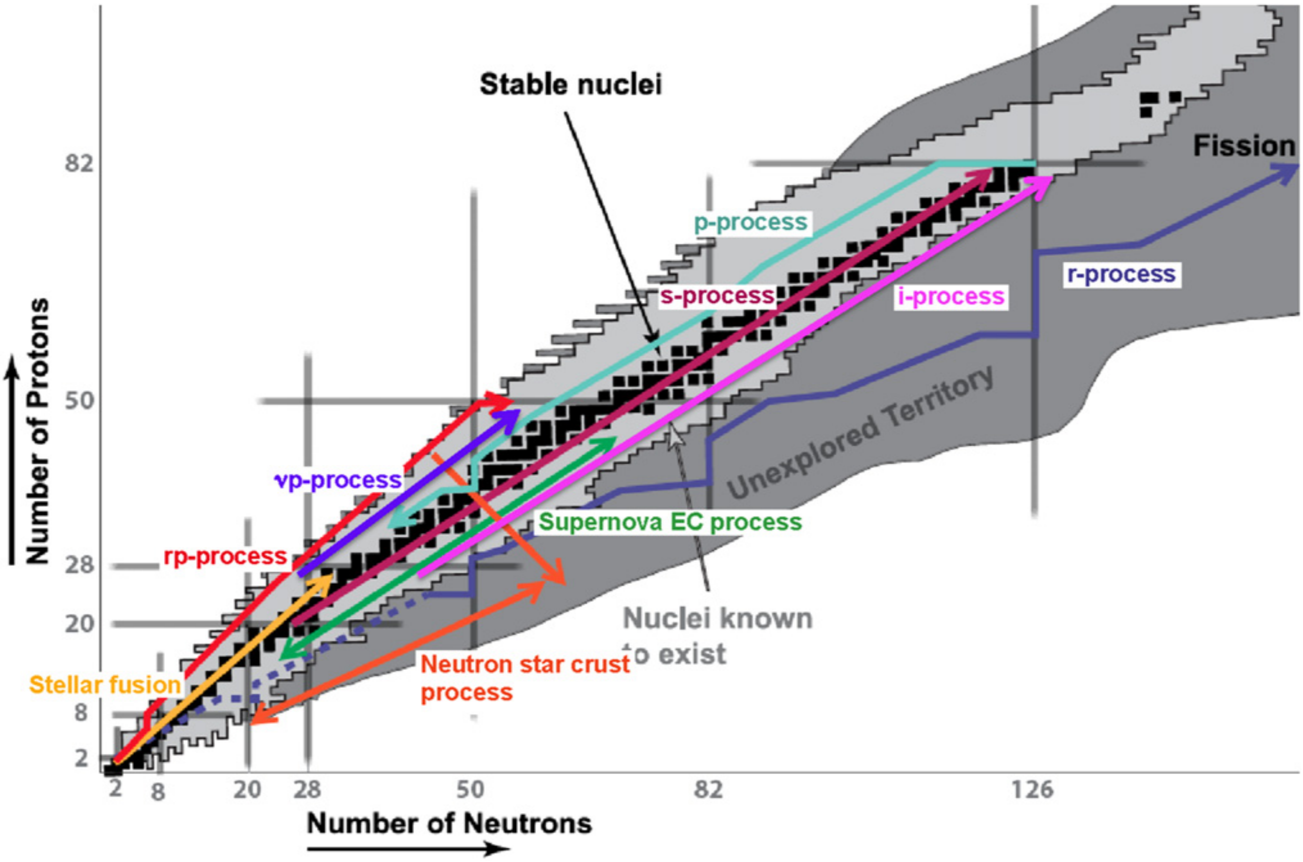

Figure 2.3: Overview of different nucleosynthesis processes in the nuclide chart. Most of the elements beyond iron are synthesized by the s- and r-process but other processes can also contribute. The figure is taken from Ref. [63] and adapted from a figure by F. Timmes.

site has to occur early in the universe (see Sect. 2.2). For a long time it has been thought that the neutrino-driven wind is a host for the r-process but recent simulations show that the conditions are not sufficient (see Sect. 2.5.2). Although the astrophysical environment for the r-process is not known, binary neutron star mergers (see, e.g., Refs. [3–5]) and magnetorotationally driven supernovae (see, e.g., Refs. [6, 7]) are possible scenarios. For further information about the r-process see, e.g., Refs. [70, 71].

Moreover, there exist some neutron-deficient stable nuclei (so-called p-only nuclides) which are bypassed by the s- and r-process. The p-only nuclides have very low abundances in the solar system. Their solar system origin is associated to the p-process (for more information see, e.g., Refs. [14, 72, 73]) but also, e.g., the νp-process (see Sect. 2.5.4) can contribute [31, 33].

Apart from the s- and r-process, other nucleosynthesis processes such as the alpha process [28, 74] or sometimes also referred to as weak r-process [23, 30] (see Sect. 2.5.3), νp-process [31–33] (see Sect. 2.5.4), rp-process [75–77], p-process [72], and i-process [78–80] may also contribute to the abundances of heavy elements but in less scale (see Fig. 2.3).

2.2 Observations from very old stars

In addition to the solar system abundances, further hints about the formation of the elements in the universe can be obtained from observations of very old stars, because they have preserved the chemical signatures of the gas from which they formed in their atmospheres. Moreover, the surface composition of these stars has not been significantly changed by internal mixing processes or by external influences such as accretion of interstellar material (see, e.g., Ref. [52]). Therefore, one can trace back the evolution of the early universe by measuring the surface composition of very old stars. The abundance of an element $\epsilon(\mathrm{A})$ in a star is given logarithmically, relative to that of hydrogen (H):

$$\log_{10}\epsilon(\mathrm{A}) \equiv \log_{10}(\mathrm{N_A}/\mathrm{N_H}) + 12, \tag{2.1}$$

where $\mathrm{N_A}$ and $\mathrm{N_H}$ are the numbers of atoms of A and H, respectively, and by definition $\log_{10}\epsilon(\mathrm{H}) = 12$. The stellar abundances in the literature are usually given relative to their values in the solar system. For two elements A and B one writes:

$$[\mathrm{A}/\mathrm{B}] \equiv \log_{10}(\mathrm{N_A}/\mathrm{N_B})_\star - \log_{10}(\mathrm{N_A}/\mathrm{N_B})_\odot, \tag{2.2}$$

where $\star$ denotes the abundance in the star and $\odot$ in the solar system.

The early universe was largely free from metals[2] and thus we can use the metallicity of a star, i.e., [Fe/H], as an indicator for its age. Consequently, stars with different metallicity content can help us to understand the conditions in the early universe up to the time when the sun formed.

The upper panel in Fig. 2.4 illustrates the abundances of six r-process enriched metal-poor stars with $[\mathrm{Fe/H}] \lesssim -2$ (see Refs. [81–86] for more information). Note that the abundances of all stars except CS 22892-052 are vertically shifted for display purposes. The six stars are compared to the scaled solar system r-process abundances (solid blue lines) which are normalized to the Eu abundance of each star. The solar system r-process abundances are obtained after subtracting the s- and p-process component of the solar system abundances. Therefore, the r-process component is not a real process, but includes residual abundances. The middle and bottom panels show individual relative offsets $\Delta\log\epsilon$ of the stars to the solar system r-process abundances from Ref. [87] and Ref. [8], respectively.

The figure indicates that the abundances beyond Ba are in agreement for all six stars (see Ref. [15] for a review). Besides, the abundances for $Z > 56$ follow closely the solar system r-process abundances. This means that the elements beyond Ba are always synthesized in the same way by a robust r-process. Since four of the stars have very low metallicities (i.e., $[\mathrm{Fe/H}] \sim 3$), and it is assumed that the time interval between the formation of the galaxy and the appearance of these stars was relatively short, the r-process must have occurred early in the universe. This is in agreement with Refs. [16–21] who proposed that the first stars were massive and evolved fast. However, Fig. 2.4 indicates a large star-to-star scatter in the abundances for $38 < Z < 47$ (see also Ref. [22]). Moreover, this abundance scatter increases at lower metallicities and anticorrelates with other abundance ratios. Therefore, Refs. [17, 18, 20, 23, 24] suggested that the origin of the elements between Sr and Ag, also referred to as lighter

---

[2] In astronomy elements with $Z > 2$ are referred to as metals.

heavy elements, is related to the r-process and at least one additional process. Furthermore, Refs. [18, 23, 88] showed that the neutrino-driven wind can be the site producing the lighter heavy elements.

Travaglio *et al.* [25] studied the origin of Sr, Y, and Zr in a galactic chemical evolution model. They could not explain the abundances of Sr, Y, and Zr in the solar system solely by adding s- and r-process contributions. Hence, Ref. [25] suggested that another primary process, which they referred to as Lighter Element Primary Process (LEPP), contributed to these elements but they did not specify an astrophysical site for the LEPP.

Montes *et al.* [26] showed that the nonuniform pattern for $Z \leq 47$ in ultra metal-poor (UMP) stars, i.e., [Fe/H] $\lesssim -4$, can be explained by a combination of r-process and LEPP. They demonstrated that the abundances for $Z \leq 47$ in UMP stars (also referred to as stellar LEPP) agrees with the missing component in the solar system abundances (also referred to as sollar LEPP) [25] within observational errors. However, it is not clear if the stellar and solar LEPP are synthesized in the same nucleosynthesis process. Furthermore, Ref. [89] presented that a solar LEPP might not be necessary.

It is possible that the LEPP is a low metallicity s-process (see Ref. [27] and references therein), or a weak r-process [30] (see Sect. 2.5.3) and/or a νp-process [31–33] (see Sect. 2.5.4). In this thesis, we assume that the LEPP is a weak r-process occurring in neutrino-driven winds following core-collapse supernova explosions.

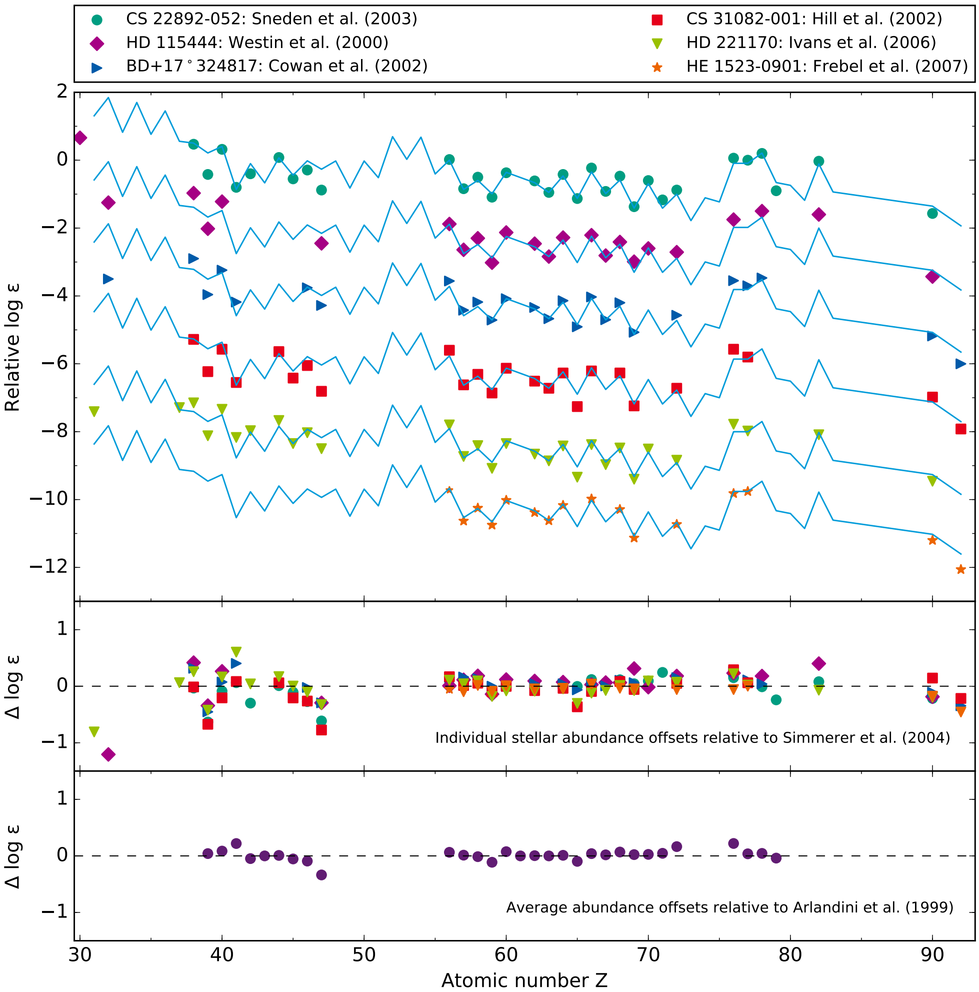

Figure 2.4: Abundances of six metal-poor stars. The upper panel compares the stellar abundances of the stars to the solar system r-process abundances (blue line). For display purposes the abundances of the stars are vertically shifted. The middle and bottom panels illustrate the relative offsets $\Delta\log\epsilon$ of the stars to the solar system r-process abundances from Ref. [87] and Ref. [8], respectively. The figure is adapted from a figure of Ref. [15].

2.3 Core-collapse supernovae

Core-collapse supernovae mark up the end of the life of massive stars with at least 8 $M_\odot$. They lead to the birth of neutron stars or stellar black holes [91–93]. During their lifetime, massive stars gain energy by hydrostatic burning (see Sect. 2.1). Since the formation of nuclei heavier than Fe-peak nuclei does not release energy, but rather costs energy, iron is the final stage of hydrostatic burning. When the hydrostatic burning ends, the star has an onion-like structure created by the previous burning stages (see Fig. 2.1). The star starts to contract because there are no fusion reactions in the core any more which exert outwards pressure. Moreover, the silicon shell burning at the interface of the iron core continuously increases the mass of the core. The electron degeneracy pressure supports the iron core against its gravity. Nonetheless, when the core reaches the Chandrasekhar mass limit of about $M_{\mathrm{Ch}} \approx 1.44\ M_\odot$, electron degeneracy pressure cannot longer stabilize the core and thus it collapses (see upper right part in Fig. 2.5).

The core-collapse is accelerated by two effects. First, as the electron density increases, electron capture reactions on protons (free and in nuclei), i.e., $(\mathrm{e}^-, \nu_\mathrm{e})$, increase and remove electrons which were contributing to the electron degeneracy pressure. Second, the core loses energy which could have provided pressure by photodisintegration reactions of Fe-group nuclei into lighter nuclei, alpha particles, and nucleons.

During the early core-collapse, the most important neutrino interactions are [94]: (neutral current) elastic scattering on nuclei, $(\nu_\mathrm{e}, \nu_\mathrm{e})$; elastic electron-neutrino scattering, $\mathrm{e}^-(\nu_\mathrm{e}, \nu_\mathrm{e})\mathrm{e}^-$; inverse beta decay, $(\nu_\mathrm{e}, \mathrm{e}^-)$; and inelastic scattering on nuclei, $(\nu_\mathrm{e}, \nu_\mathrm{e}')$. When the density in the core reaches $\rho = 10^{12}$ g cm^{-3}, neutrinos are trapped because they interact more often, and thus their diffusion time is longer than the collapse time [95]. The collapse continues until the inner core is compressed to nuclear densities ($\rho = 10^{14}$ g cm^{-3}). Then, the core decelerates and bounces back to respond to further compression. This leads to a shock wave which moves outwards the core into the infalling matter (right part in Fig. 2.5). The shock wave loses energy by photodisintegration reactions of Fe and Ni isotopes as it runs through the outer core and due to neutrino emission.

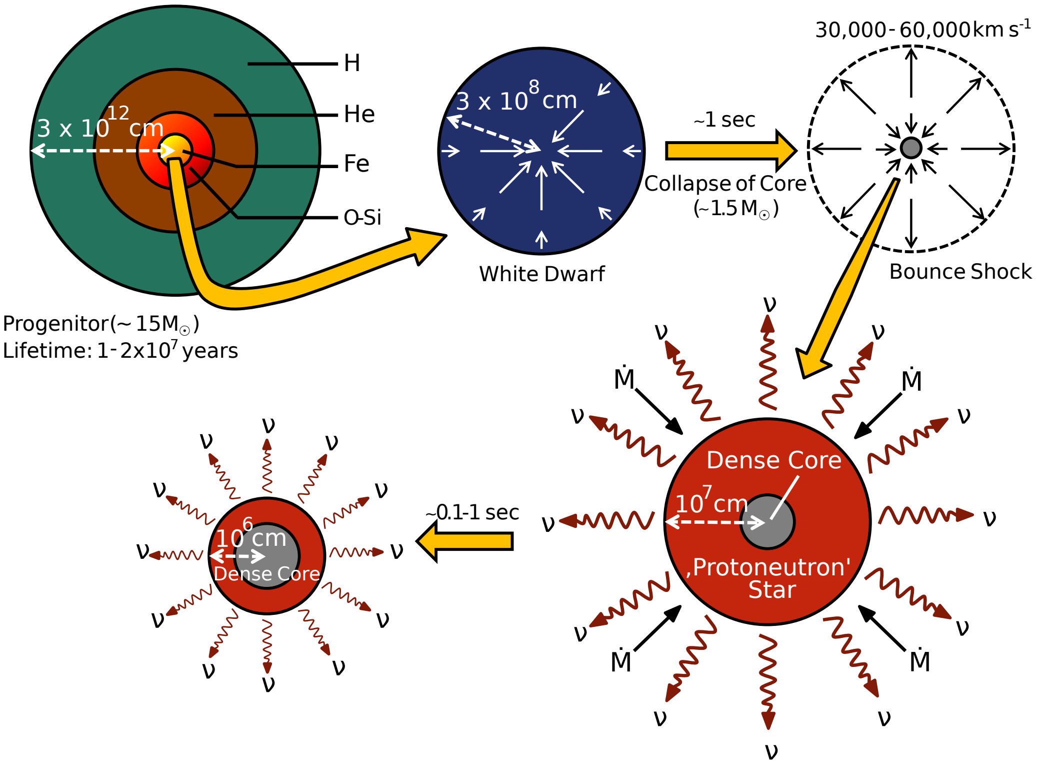

Figure 2.5: Schematic overview of a core-collapse supernova described clockwise beginning from the upper left corner. The iron core of a massive star collapses to a hot proto-neutron star. The hot proto-neutron star cools down by neutrino emission and ends up as a neutron star. Courtesy of Ref. [90] and adapted from Ref. [43].

The questions why and how core-collapse supernovae explode is a central and long-lasting problem in supernova theory [42, 43, 53]. In the past, it was believed that the energy available to the shock wave is large enough to stop the core-collapse and also to explode the outer shells of the star (this explosion mechanism is referred to as prompt mechanism) [96]. However, the shock wave loses most of its available energy by photodisintegration reactions of heavy nuclei into nucleons and alpha particles. Moreover, electron capture reactions on free protons lead to an additional energy loss and giving rise to a strong burst of electron neutrinos. Most of the neutrinos produced by electron capture reactions behind the shock leave the star and carry away energy. Consequently, the shock wave stalls at a radius of $r \sim 100-200$ km in the outer core.

Today, it is believed that the neutrinos which emerge from the hot and dense core revive the shock (this explosion mechanism is referred to as delayed neutrino-heating mechanism [97]). The neutrinos carry most the energy released in the gravitational collapse of the Fe core ($\sim 10^{53}$ erg) [98] and deposit some of their energy before the shock [99]. The revived shock expels the outer layer of the star and leads to a successful explosion. The outgoing shock wave compresses and heats up the layers of different compositions for a short period of time and nuclei up to $Z = 44$ are synthesized during explosive nucleosynthesis (see, e.g., Ref. [40]). After a successful core-collapse supernova explosion a hot proto-neutron star is born. For further information about core-collapse supernovae see, e.g., Refs. [42–44].

2.4 Neutrino-driven winds

During the collapse of a massive star, its gravitational energy is converted into internal energy. Therefore, the initial temperature of the proto-neutron star is high (i.e., $k_B T \approx 30-50$ MeV). The hot proto-neutron star cools down by neutrinos which take away the energy. Since the densities in the hot proton-neutron star are very high (i.e., $\rho \sim 10^{14}$ g cm^{-3}), neutrinos are trapped. They diffuse from the interior of the proto-neutron star and they can flow freely when their mean free path is at the order of the neutron star radius. The neutrinos are emitted from the neutrinosphere which is located at the outer part of the proto-neutron star. Reference [100] showed that in a good approximation the neutrinos are emitted isotropically from the neutrinosphere. Since neutrino-matter interactions are strongly energy dependent, the neutrinosphere is different for every neutrino flavor and energy. Some of the escaping neutrinos deposit energy in the matter at the neutrinosphere, mainly via charged-current reactions:

$$\nu_e + \mathrm{n} \rightarrow \mathrm{p} + \mathrm{e}^-, \tag{2.3}$$

$$\bar{\nu}_e + \mathrm{p} \rightarrow \mathrm{n} + \mathrm{e}^+. \tag{2.4}$$

This causes a significant mass fraction of the outer layers of the proto-neutron star to be blown off in a neutrino-driven wind. The neutrino-driven wind develops after the explosion and lasts for several seconds or even minutes. Reference [34] was the first who addressed the neutrino-driven wind.

2.4.1 Wind dynamics

The neutrino luminosities and energies as well as the neutron star mass and radius change only slowly during the Kelvin-Helmholtz time scale (i.e., the time it takes for a star to radiate away its gravitational energy). Hence, the neutrino-driven wind can be assumed to be a steady-state outflow with boundaries at the neutrinosphere and the shock [34]. Seconds after the explosion the shock wave is already at large radii ($r \sim 10000$ km) and a continuous mass outflow from the surface of the proto-neutron star has begun which allow to study the neutrino-driven wind independently of the supernova mechanism. The neutrino-driven wind has been described as a steady-state outflow by several studies (see Refs. [34, 55, 101–104]). Since the wind arises close to the surface of the neutron star, general relativistic effects have to be included in the steady-state wind models (see Refs. [101–104]). The basic equations for a spherically symmetric steady-state wind in the Schwarzschild geometry are [105]:

$$\dot{M} = 4\pi r^2 \rho u, \tag{2.5}$$

$$u\frac{\mathrm{d}u}{\mathrm{d}r} = -\frac{1}{\rho_{\mathrm{tot}} + P}\frac{\mathrm{d}P}{\mathrm{d}r}\left(1 + u^2 - \frac{2M}{r}\right) - \frac{M}{r^2}, \tag{2.6}$$

$$\dot{q} = u\left(\frac{\mathrm{d}\epsilon}{\mathrm{d}r} - \frac{P}{\rho^2}\frac{\mathrm{d}\rho}{\mathrm{d}r}\right), \tag{2.7}$$

where $\dot{M}$ is the constant mass outflow rate, r is the distance from the center of the neutron star, ρ is the (baryon) mass density, u is the radial velocity, $\rho_{\mathrm{tot}} = \rho + \rho\epsilon$ is the total energy density, ϵ is the specific internal energy, P is the pressure, M is the mass of the neutron star, and $\dot{q}$ is the net heating rate due to neutrino interactions. Note that the Planck constant $\hbar$, the speed of light c, the Boltzmann constant k_{B}, and gravitational constant G are taken to be unity in Eqs. (2.5)–(2.7). A Newtonian approach for a steady-state wind is described, e.g., in Ref. [55]. The heating rate $\dot{q}$ (see Eq. (2.7)) depends on neutrino-matter interactions. For example, Refs [55, 106, 107] took into account five neutrino-processes including three heating processes (i.e., neutrino and antineutrino absorption by free nucleons, neutrino and antineutrino scattering by electrons and positrons, and neutrino-antineutrino annihilation into electron-positron pairs) and two cooling processes (i.e., electron and positron capture by free nucleons and electron-positron annihilation into neutrino-antineutrino pairs). A detailed description of the different contributions to $\dot{q}$ is given in Ref. [102]. In the Schwarzschild geometry the neutrino trajectory is bent which leads to an increase of the heating rate compared to the Newtonian approach. In addition, the redshift affects the neutrino energy but leads to a decrease of the heating rate. Reference [102] showed that relativistic corrections in the neutrino treatment have only a minor effect on the neutrino-driven wind.

There are three types of solutions for the system of Eqs. (2.5)–(2.7) which depend on the mass outflow $\dot{M}$ (see Ref. [45]). These solutions are graphically illustrated in Fig. 2.6. For a large enough mass outflow ($\dot{M} = \dot{M}_{\mathrm{crit}}$), the velocity reaches the speed of sound and remains for $r \to \infty$ (blue line in Fig. 2.6). Then, the shock region and the neutron star are sonically disconnected. This is the wind solution, sometimes also referred to as supersonic solution. If the velocity does not become supersonic, i.e., $\dot{M} < \dot{M}_{\mathrm{crit}}$, we obtain a breeze solution (sometimes also referred to as subsonic solution). The velocity has a maximum and decreases for larger radii (see green line in Fig. 2.6). Both the wind and the breeze solution have a physical meaning. We receive unphysical solutions for $\dot{M} > \dot{M}_{\mathrm{crit}}$ because this would lead to a infinite acceleration of the mass outflow [55]. Note that there is only one physical supersonic solution while one can find infinite breeze and unphysical solutions [45].

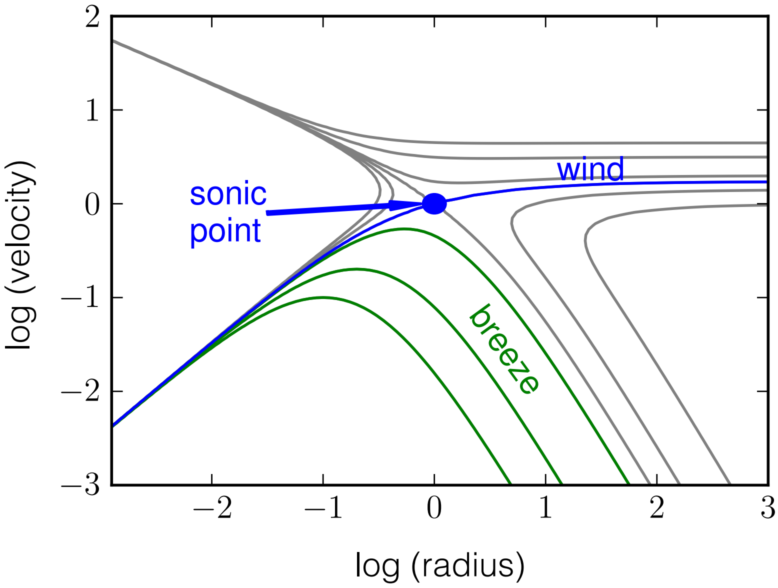

Figure 2.6: Graphical illustration of the solutions of Eqs. (2.5)–(2.7). The blue line indicates the wind solution for which the velocity becomes supersonic. Some of the physical subsonic and unphysical solutions are illustrated by the green and grey lines, respectively. At the sonic point the local sound velocity is equal to the speed of sound. The figure is taken from Ref. [45].

Steady-state wind models have been utilized to better understand neutrino-driven winds and to identify the required conditions for the r-process (we will focus on this in Sect. 2.5.2). Reference [55] showed based on their steady-state wind models, which do not include relativistic effects, that the impact of the neutron star mass (M_{ns}) and radius (R_{ns}) as well as the neutrino luminosity (L_ν) and energy (ϵ_ν) on the mass outflow ($\dot{M}$), entropy (S), and time scale (τ) in the neutrino-driven wind can be described with the following relations:

$$\dot{M} \propto L_\nu^{5/3} \epsilon_\nu^{10/3} R_{\mathrm{ns}}^{5/3} M_{\mathrm{ns}}^{-2}, \tag{2.8}$$

$$S \propto L_\nu^{-1/6} \epsilon_\nu^{-1/3} R_{\mathrm{ns}}^{-2/3} M_{\mathrm{ns}}, \tag{2.9}$$

$$\tau \propto L_\nu^{-1} \epsilon_\nu^{-2} R_{\mathrm{ns}} M_{\mathrm{ns}}. \tag{2.10}$$

Moreover, Ref. [102] demonstrated that relativistic corrections in the steady-state wind models increase the entropy and decrease the time scale of the neutrino-driven wind relative to those in the Newtonian treatment.

2.5 Nucleosynthesis in neutrino-driven winds

Due to the high temperature ($T \geq 10$ GK) close to the surface of the proto-neutron star matter is in nuclear statistical equilibrium (NSE). In NSE, there is a balance (i.e., a chemical equilibrium) between nuclear reactions producing seed nuclei (Z,A) and photodissociation reactions destroying seed nuclei into neutrons and protons: $(Z,A) \longleftrightarrow (A-Z)\mathrm{n} + Z\mathrm{p}$. The nuclear composition is uniquely determined by the temperature, density, neutron and proton abundance during NSE. A detailed derivation of NSE abundances will be given in Sect. 3.2.3. The NSE composition at high temperatures is dominated by alpha particles, neutrons, and protons. We will describe the nucleosynthesis evolution in the wind following Fig. 2.7. The wind material close to the proto-neutron star is very hot ($T \geq 10$ GK), and thus it basically consists of free neutrons and protons, although light cluster (^{2}H, ^{3}H, ^{3}He, ^{4}He) can be also present (see, e.g., Ref. [108]). Weak interactions convert neutrons into protons, and vice versa. As the matter expands, the temperature decreases and the nuclear composition changes. Around $T = 9$ GK, alpha particles are formed, and for further decreasing temperatures alpha particles and nucleons build seed nuclei. Hence, the neutron and proton abundances strongly decrease. When the wind material further expands, it cools down and slower reactions fall out of equilibrium. At the break down of NSE between $T \approx 8-5$ GK alpha particles dominate the nuclear composition. This is the so-called alpha-rich freeze-out. Then alpha particles form ^{12}C by triple-alpha reactions ($3\alpha \rightarrow^{12}$ C), or, if the amount of free neutrons is still large enough, by $^4\mathrm{He}(\alpha\mathrm{n},\gamma)^9\mathrm{Be}(\alpha,\mathrm{n})^{12}\mathrm{C}$ reactions [28]. The synthesis of ^{12}C strongly depends on the density. For fast expansions, the formation of ^{12}C is hindered because the density does not remain for a sufficient long time in the range where the three body reactions are effective (i.e., $\rho \approx 5 \cdot 10^6 \mathrm{g\ cm}^{-3}$) [45]. The production of ^{12}C is followed by a sequence of alpha capture reactions, i.e., (α,n), (α,p), and (α,γ) reactions, in combination with (n,γ), (n,p), and (p,γ) reactions

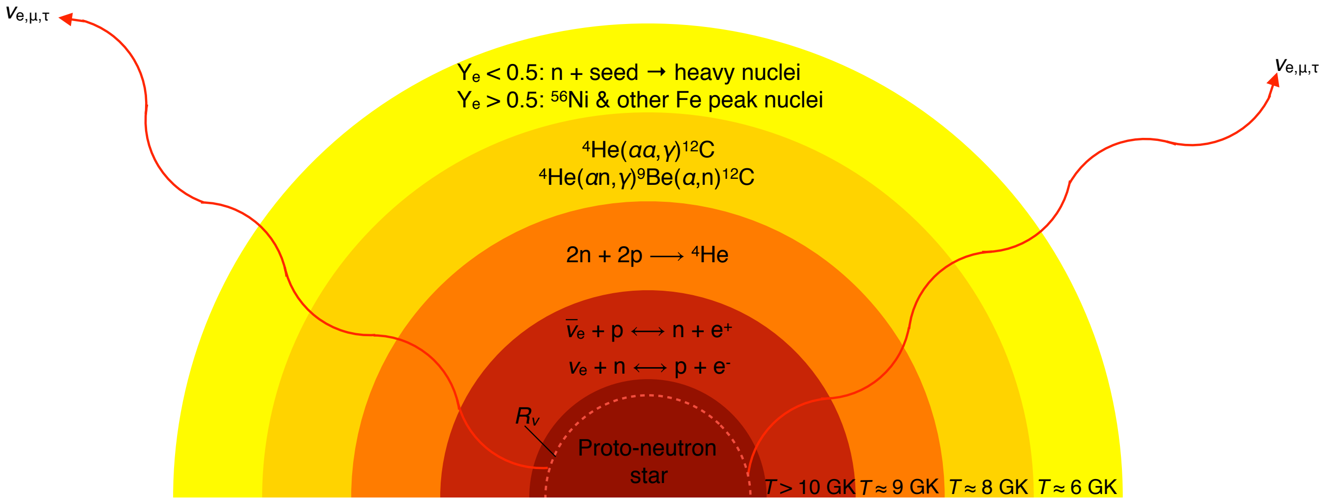

Figure 2.7: Nucleosynthesis evolution in neutrino-driven winds. Close to the surface of the proto-neutron star the wind material is very hot, and thus mainly consists of free neutrons and protons. As the wind expands, nucleons combine into alpha particles, and for further decreasing temperatures alpha particles form ^{12}C. Depending on the electron fraction, the neutron and the alpha abundance, different heavy nuclei are synthesized.

depending on the neutron-richness of the wind. This is the so-called alpha-process [28, 109]. The charged particle reactions freeze out when the temperature is too low to overcome the Coulomb barrier ($T \approx 1$ GK). Then the nuclear composition mainly consists of alpha particles, along with seed nuclei synthesized during the alpha process, neutrons, and protons. The evolution of the nuclear composition strongly depends on the neutron, proton, and seed nuclei abundances (see, e.g., Refs. [29, 55, 103, 110, 111]) which are determined by the wind parameters.

2.5.1 Wind parameters in neutrino-driven winds

The wind parameters which govern the nucleosynthesis in neutrino-driven winds are the entropy, the expansion time scale, and the electron fraction. In a radiation dominated environment the entropy depends on the temperature and the density by $S \propto \frac{T^3}{\rho}$. Thus, high temperatures and low densities result in large entropies. Besides, the entropy is proportional to the photon-to-baryon ratio [74, 110]. High temperatures lead to the existence of energetic photons which destroy seed nuclei into nucleons, and therefore the seed abundance (Y_{seed}) is decreased and the neutron abundance (Y_{n}) is raised. Moreover, at low densities the probability that the three-body reactions $3\alpha \rightarrow^{12}$ C and $^4\mathrm{He}(\alpha\mathrm{n},\gamma)^9\mathrm{Be}(\alpha,\mathrm{n})^{12}\mathrm{C}$ occur is small. Since these reactions mark the beginning of the seed formation, lower densities result in lower Y_{seed}. Hence, high entropies lead to large neutron-to-seed ratios ($Y_{\mathrm{n}}/Y_{\mathrm{seed}}$).

The expansion time scale describes how fast matter expands during the alpha particle and seed nuclei formation at $T = 0.5$ MeV. It is given by [55]

$$\tau = \left.\frac{r}{v}\right|_{T=0.5\ \mathrm{MeV}}, \tag{2.11}$$

where r and v are the radius and velocity, respectively. For fast expansions, i.e., short expansion time scales, the time for the three-body reactions to form seed nuclei is short. Therefore, a small expansion time scale leads to a small Y_{seed}.

The electron fraction (Y_{e}) is defined as the number of electrons per baryon:

$$Y_{\mathrm{e}} = \frac{n_{\mathrm{e}^-} - n_{\mathrm{e}^+}}{n_{\mathrm{b}}}, \tag{2.12}$$

where n_{e^-}, n_{e^+}, and n_{b} are the number densities of the electrons, positrons, and baryons, respectively. Hence, the electron fraction indicates whether the wind is neutron-rich (i.e., $Y_{\mathrm{e}} < 0.5$) or proton-rich (i.e., $Y_{\mathrm{e}} > 0.5$). Since the astrophysical environment is charge neutral, the electron fraction can be written as

$$Y_{\mathrm{e}} = \sum_i Z_i Y_i = \sum_i (Z_i/A_i) X_i. \tag{2.13}$$

The sums in Eq. (2.13) run over all nuclear species i with charge Z_i, mass number A_i, number abundance Y_i, and mass fraction X_i. Equation (2.13) will be derived in Sect. 3.2. We have already mentioned that close to the proto-neutron star the wind mainly consists of nucleons, which implies that $Y_{\mathrm{e}} = X_{\mathrm{p}}$ or $Y_{\mathrm{e}} = 1 - X_{\mathrm{n}}$, where X_{n} and X_{p} are the mass fractions of the neutrons and protons, respectively. As the wind expands, the temperature decreases and alpha particles are formed, leading to $Y_{\mathrm{e}} = X_{\mathrm{p}} + X_\alpha/2$, where X_α is the mass fraction of the alpha particles. Further away from the proto-neutron star heavy nuclei are synthesized and Eq. (2.13) can be rewritten as

$$Y_{\mathrm{e}} = X_{\mathrm{p}} + \frac{X_\alpha}{2} + \sum_{h>4} \left(\frac{Z_h}{A_h}\right) X_h, \tag{2.14}$$

where the sum runs over all nuclei h which are heavier than alpha particles. However, due to the small amount of heavy nuclei when the initial wind electron fraction is calculated, the last term in Eq. (2.14) can be neglected. Since nucleons combine into alpha particles during NSE, the so-called alpha effect (see, e.g., Refs. [112–116]) results in an increase of Y_{e}. A detailed derivation of the electron fraction is given, e.g., in Refs. [113, 117].

The electron fraction is altered by weak reactions. The evolution of the electron fraction, neglecting the alpha process and assuming that the initial wind composition only consists of neutron and protons, is described by

$$\frac{\mathrm{d}Y_{\mathrm{e}}}{\mathrm{d}t} = v(r)\frac{\mathrm{d}Y_{\mathrm{e}}}{\mathrm{d}r} \approx \left(\lambda_{\nu_{\mathrm{e}}} + \lambda_{\mathrm{e}^+}\right) Y_{\mathrm{n}} - \left(\lambda_{\bar{\nu}_{\mathrm{e}}} + \lambda_{\mathrm{e}^-}\right) Y_{\mathrm{p}}, \tag{2.15}$$

where $v(r)$ is the velocity of the matter and λ_x ($x = \nu_\mathrm{e}$, e^+, $\bar{\nu}_\mathrm{e}$, e^-) are the weak rates of the forward and reverse reactions in Eq. (2.3) and Eq. (2.4). Nevertheless, the evolution of Y_e is dominated by electron neutrino and electron antineutrino captures on nucleons. Hence, the electron fraction, which is equal to the proton to nucleon ratio in a charge neutral wind, in equilibrium (i.e., $\dot{Y}_\mathrm{e} = 0$) is described by:

$$Y_\mathrm{e,eq.} = \frac{Y_\mathrm{p}}{Y_\mathrm{p} + Y_\mathrm{n}} = \frac{1}{1 + \frac{\lambda_{\bar{\nu}_\mathrm{e}}}{\lambda_{\nu_\mathrm{e}}}}. \tag{2.16}$$

Reference [55] showed that the equilibrium wind electron fraction is approximately given by :

$$Y_\mathrm{e,eq.} \approx \left[1 + \frac{L_{\bar{\nu}_\mathrm{e}} \left(\epsilon_{\bar{\nu}_\mathrm{e}} - 2\Delta + 1.2\Delta^2/\epsilon_{\bar{\nu}_\mathrm{e}} \right)}{L_{\nu_\mathrm{e}} \left(\epsilon_{\nu_\mathrm{e}} + 2\Delta + 1.2\Delta^2/\epsilon_{\nu_\mathrm{e}} \right)} \right]^{-1}, \tag{2.17}$$

where L_{ν_e}, $\epsilon_{\nu_\mathrm{e}}$ and $L_{\bar{\nu}_\mathrm{e}}$, $\epsilon_{\bar{\nu}_\mathrm{e}}$ denote the luminosities and mean energies of the electron neutrinos and antineutrinos, respectively. The neutron-proton mass difference is $\Delta = m_\mathrm{n} - m_\mathrm{p} = 1.293$ MeV. Therefore, for a neutron-rich wind, the antineutrino and neutrino energies have to approximately fulfill $\epsilon_{\bar{\nu}_\mathrm{e}} - \epsilon_{\nu_\mathrm{e}} \gtrsim 4\Delta \approx 5$ MeV, assuming equal electron neutrino and antineutrino luminosities.

In this section, we have described how the entropy and the expansion time scale influence the neutron-to-seed ratio. Depending on the Y_e and the $Y_\mathrm{n}/Y_\mathrm{seed}$, different nucleosynthesis processes occur in neutrino-driven winds. In the following, we will give an overview about the possible nucleosynthesis processes and describe the development of the neutrino-driven wind as a possible astrophysical site for the r-process.

2.5.2 The neutrino-driven wind as a possible astrophysical site for the r-process: A historical overview

The r-process evolves far away from the valley of stability on the neutron-rich side which requires extreme astrophysical conditions (see Sect. 2.1). For a successful r-process building elements up to uranium, electron fractions below $Y_\mathrm{e} < 0.5$, high entropies and small expansion time scales resulting in a high neutron-to-seed ratio $Y_\mathrm{n}/Y_\mathrm{seed} \gtrsim 100$ are required. For a long time, the neutrino-driven wind has been suggested as a possible host for the r-process. However, the extreme conditions required for a r-process are not found in wind simulations. Even though it is likely that the neutrino-driven wind is not the astrophysical site for the r-process, studies of the wind contributed to identify the necessary conditions for the r-process. Therefore, we will give a historical overview about the development of the neutrino-driven wind as a possible site for the r-process. This overview follows to large extent the one described in Ref. [45].

Bethe and Wilson [99] performed the first delayed neutrino-driven supernova explosions. Based on Bethe and Wilson's supernova explosion, Woosley and Hoffman [28] investigated the nucleosynthesis in the high-entropy wind from the proto-neutron star. Woosley and Hoffman found that the late wind evolution could lead to the high entropy and the low electron fraction required for a successful r-process. Besides, Meyer *et al.* [74] studied the nucleosynthesis evolution based on Bethe and Wilson's supernova explosion for different Y_e. The final abundances composed of the superposition of the trajectories with different electron fractions agreed rather well with the solar system abundances. Furthermore, Woosley *et al.* [35] performed hydrodynamical simulations with the spherically symmetric supernova model of Wilson and Mayle [97] for a 20 $M_\odot$ progenitor and followed the ejecta for 20 s. They obtained the required conditions for a successful r-process, i.e., high entropies of $S \approx 400$ k_B/nuc and electron fractions of $Y_\mathrm{e} \approx 0.35$. In addition, Woosley *et al.* [35] achieved a good agreement with the solar system r-process abundances with only a slight overproduction at $A = 90$. Therefore, Woosley *et al.* [35] concluded that the neutrino-driven wind is the most promising site for the r-process.

However, no other independent group could reproduce the results of Woosley *et al.* [35]. Witti *et al.* [109] also performed hydrodynamical simulations with the supernova model of Wilson and Mayle [97] for a 25 $M_\odot$ progenitor and studied the late evolution of the ejecta. In contrast to Woosley *et al.* [35], they only received entropies below $S \approx 100$ k_B/nuc and electron fractions above $Y_\mathrm{e} \approx 0.45$. For these wind conditions, the r-process did not occur and they found a large overproduction of nuclei with $A = 90$. In a follow-up paper, Takahashi *et al.* [118] showed that the solar system r-process abundances can be reproduced without an overproduction of nuclei at $A = 90$ if the entropy is increased by a factor of 5, i.e., the density is decreased by the same factor.

The neutrino-driven wind was studied based on an analytical model by Qian and Woosley [55]. Since they did not find the necessary conditions for a r-process, they studied the influence of possible missing contributions, i.e., an outer boundary or an extra energy source. Qian and Woosley [55] predicted that any effect which enhances the gravitational potential results in a raised entropy. Hoffman *et al.* [111] generalized the analytical model of Qian and Woosley [55] and put constraints on the wind parameters. Moreover, they demonstrated that for the electron fractions and dynamic time scales revealed by Woosley *et al.* [35], the entropy cannot become $S \approx 400\ k_\mathrm{B}/\mathrm{nuc}$.

Cardall and Fuller [101] included general relativistic effects in the neutrino-driven wind. They found a more compact neutron star and thus a higher entropy than in the Newtonian approach. The advanced studies of Otsuki *et al.* [102] and Thompson *et al.* [103] presented that general relativity effects in neutrino-driven winds increase the entropy up to 40% compared to the Newtonian treatment. Furthermore, Otsuki *et al.* [102] showed that general relativity effects in the neutrino treatment only have a minor effect on the wind.

Figure 2.8 gives an overview which combinations of the wind parameters result in a successful r-process based on the steady-state models of Otsuki *et al.* [102]. The figure presents the relation between the entropy and the time scale for various combinations of the neutron star mass and the neutrino luminosity and $Y_\mathrm{e} = 0.40$. The solid and dashed lines connect the same masses and luminosities, respectively. The blue and red bands indicate the required entropies and time scales for $Y_\mathrm{e} = 0.40$ to synthesize elements up to the second (A=130) and third ($A = 195$) r-process peak, respectively. The necessary conditions are attained for a massive neutron star with a small radius (i.e., a compact neutron star) [102, 103].

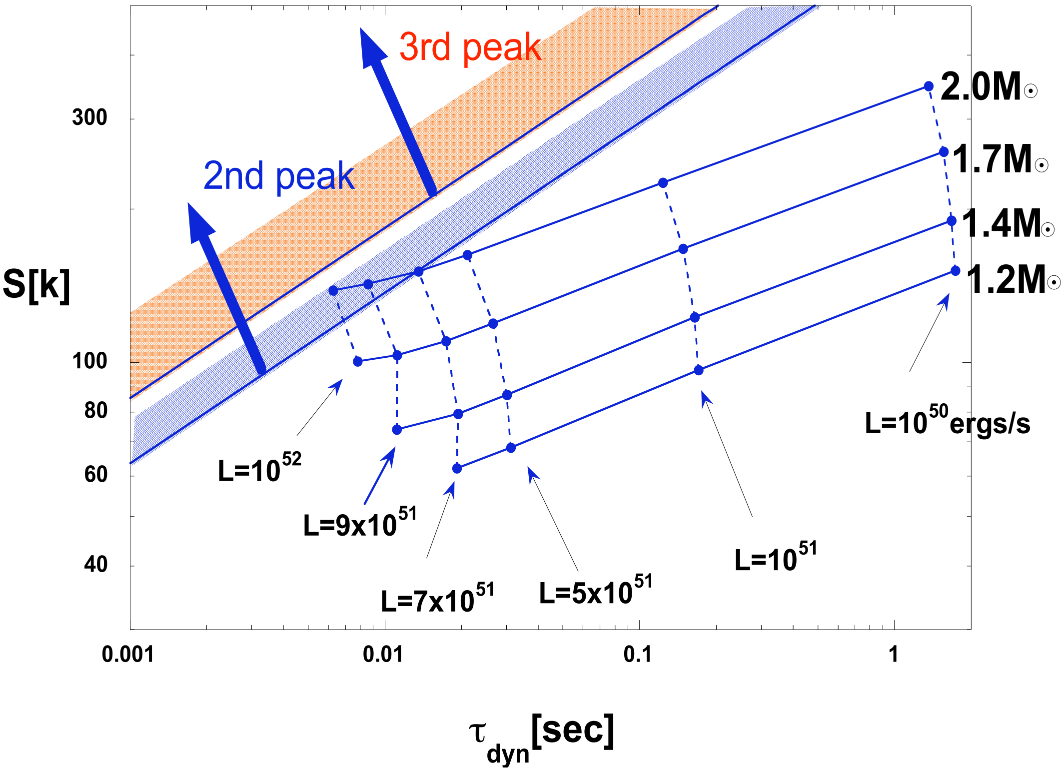

Figure 2.8: Relation between the entropy and time scale for various neutron star masses and neutrino luminosities and $Y_\mathrm{e} = 0.40$. The blue and red band illustrate the required combinations of entropy and timescale leading to the formation of elements up to the second and third r-process peak, respectively. The figure is taken from Ref. [45].

In summary, all parametric studies of the neutrino-driven wind could not reproduce the r-process found by Woosley *et al.* [35]. Besides, first long-time hydrodynamic simulations [36], even in two dimensions [37], do not evince the required conditions for a successful r-process. Furthermore, more sophisticated hydrodynamic simulations using a Boltzmann neutrino transport [38, 39] indicate that the neutrino-driven wind may be proton-rich or turns proton-rich for some time. Nonetheless, even if the neutrino-driven wind is not the astrophysical site for the r-process and is only slightly neutron-rich or proton-rich, it is an exciting site for the formation of the lighter heavy elements. The lighter heavy elements are produced in the neutrino-driven wind either by the weak r-process and/or the νp-process.

2.5.3 Weak r-process

The weak r-process [30] occurs in slightly neutron-rich winds, i.e., $0.40 \lesssim Y_e \lesssim 0.50$. It is sometimes also referred to as charged-particle reaction (CPR) process [23, 28, 29], or alpha process [28] (this name was originally given by Ref. [1] to a process that is referred to as neon burning today). The weak r-process depends on the wind parameters in the same way as the r-process: lower Y_e, higher entropies, and/or smaller expansion time scales lead to larger neutron-to-seed ratios and thus heavier elements are synthesized (see, e.g., Refs. [45, 119]). However, the neutron-to-seed ratio in the weak r-process (i.e., $Y_n/Y_{\text{seed}} \lesssim 20$) is much smaller than in the r-process (i.e., $Y_n/Y_{\text{seed}} \gtrsim 100$). There are main differences between the weak r- and the r-process. As the temperature decreases in the weak r-process, the seed nuclei abundance significantly increases but the alpha particles still dominate the nuclear composition. Due to the low neutron abundance, the nucleosynthesis path proceeds close to the valley of stability on the neutron-rich side. Since the beta decay time scales close to stability are longer than the expansion time scale of the wind, matter moves towards heavy nuclei mainly via alpha capture reactions and especially via (α, n) reactions [28], while in the r-process heavier nuclei are reached by beta decays. Another main difference is that the weak r-process only synthesizes elements below the second r-process peak ($Z < 56$), whereas the r-process builds elements up to uranium. The dominant products in the weak r-process are Sr, Y, and Zr (see, e.g., Refs. [35, 119–121]). Consequently, the weak r-process could have contributed to the formation of the lighter heavy elements between Sr and Ag in the early universe (see Sect. 2.2).

Most of the nucleosynthesis studies in the weak r-process aimed on finding the wind parameters which lead to a good agreement between the calculated and observed abundances of the lighter heavy elements. There exist several combinations of wind parameters which produce lighter heavy elements in slightly neutron-rich winds (see, e.g., Ref. [121]). Nonetheless, neutron-rich winds do not provide robust abundance pattern because slight variations of the wind parameters result in different abundance patterns (see, e.g., Ref. [119]). Besides, there is an overproduction around $A \approx 90$ related to the neutron shell closure $N = 50$ [28, 29, 35, 109, 121, 122]. Therefore, in order not to overproduce elements with $A \approx 90$, only a subset of core-collapse supernovae, or only a small amount of their ejecta can be neutron-rich. Then neutron-rich winds could also contribute to the solar LEPP [121] (see Sect. 2.2). However, before one can make full use of observations to put constraints on the wind parameters and thus on neutrino-driven winds, the impact of nuclear physics uncertainties on the weak r-process has to be reduced.

Although recent supernova simulations indicate proton-rich wind conditions [38, 39, 123], there are still uncertainties in the neutrino physics which could lead to slightly neutron-rich conditions. The authors of Ref. [124] proposed that active-sterile neutrino transformation could influence the electron fraction. They found that the optimal range in neutrino mixing parameters results in a significantly reduced electron fraction. Besides, Ref. [125] showed that the inclusion of active-active collective oscillations and MSW conversions together with active-sterile mixing decreases the Y_e. Furthermore, mean field effects are not yet fully consistently included in supernova simulations [38, 39], although they are non-negligible due to the high densities at the neutrinosphere. The authors of Refs. [126–128] presented that the modification of the charged-current weak interaction processes could lead to electron fractions down to $Y_e = 0.45$. Moreover, a two-dimensional simulation of the explosion of an ONeMg progenitor showed that neutron-rich lumps with electron fractions down to 0.40 are ejected due to the very fast explosion [129].

In this thesis, we assume the additional process which contributes to the formation of the lighter heavy elements corresponds to the weak r-process. However, since the neutrino-driven wind could be also proton-rich, we will also give an overview about the νp-process occurring in proton-rich winds in the following section.

2.5.4 νp-process

As we have mentioned before, some supernova simulations indicated that the neutrino-driven wind is proton-rich, either at very early times [31–33, 39, 130–132], or during a time period up to 20 s [38, 39]. In proton-rich winds, the nuclear composition after the alpha-rich freeze out consists of alpha particles and an excess of protons. The nucleosynthesis path evolves towards heavier nuclei on the proton-rich side of stability by (p, γ), (α, γ), and (α, p) reactions and beta decays (i.e., β^+) once the temperature falls below $T = 3$ GK. The nucleosynthesis path moves up to ^{56}Ni and even up ^{64}Ge which act as bottlenecks. The beta decay half-lifes of ^{56}Ni (i.e., $T_{1/2} = 6.075$ d) and ^{64}Ge (i.e., $T_{1/2} = 64$ s) are long compared to the expansion time scale of the wind and thus matter accumulates there. Since the material in the wind is under a high neutrino flux, antineutrino absorption on protons produces free neutrons ($10^{14} - 10^{15}$ cm^{-3} [31]) for several seconds, when the temperature is between $T = 3 - 1$ GK. These additional neutrons participate in the nucleosynthesis and lead to (n,p) reactions which are faster than beta decays. Note that a (n,p) reaction connects the same pair of nuclides as a beta plus decay. The (n,p) reactions followed by (p,γ) reactions permit the nucleosynthesis flow to overcome the bottlenecks at ^{56}Ni and ^{64}Ge, and therefore to reach heavier elements. This is the so-called νp-process [31–33].

The efficiency to produce additional neutrons strongly depends on the wind parameters and on the neutrino luminosities and energies. The impact of the wind parameters on the νp-process has been discussed by, e.g., Refs. [133, 134]. The entropy influences the neutron-to-seed ratio in the same way as in neutron-rich winds, i.e., higher entropies lead to larger $Y_\mathrm{n}/Y_\mathrm{seed}$. Since neutrons are required to bridge the bottlenecks, the time matter spends at high enough temperatures is also relevant. Shorter expansion time scales result in lower Y_seed but also in smaller Y_n because less neutrons are produced. Therefore, the expansion time scale has only a moderate effect on the nucleosynthesis (see, e.g., Ref. [119]). The electron fraction affects the nucleosynthesis because it determines the proton abundance. Since the initial wind composition is dominated by nucleons, the initial electron fraction describes the amount of protons, i.e., $Y_\mathrm{p} = Y_\mathrm{e}$ and $Y_\mathrm{n} = 1 - Y_\mathrm{e}$. After the initial fast expansion of the wind, neutrons are rapidly captured but also produced by antineutrino absorption on protons. Hence, the neutron abundance is in an equilibrium:

$$\frac{\mathrm{d}Y_\mathrm{n}}{\mathrm{d}t} = \lambda_{\bar{\nu}_\mathrm{e}} Y_\mathrm{p} - \sum_{Z,A} N_\mathrm{n} Y(Z,A) \langle \sigma v \rangle_{(Z,A)} = 0, \tag{2.18}$$

where $\lambda_{\bar{\nu}_\mathrm{e}}$ is the electron antineutrino absorption rate and $\langle \sigma v \rangle_{(Z,A)}$ is the sum of neutron capture rates (i.e., (n,p) and (n,γ)) of a nucleus (Z,A). Rewriting Eq. (2.18) leads to

$$N_\mathrm{n} = \frac{\lambda_{\bar{\nu}_\mathrm{e}} Y_\mathrm{p}}{\sum_{Z,A} Y(Z,A) \langle \sigma v \rangle_{(Z,A)}}, \tag{2.19}$$

which indicates that the neutron abundance increases for higher Y_p (i.e., higher Y_e) and $\lambda_{\bar{\nu}_\mathrm{e}}$. The electron antineutrino absorption rate depends on the electron antineutrino energy ($\epsilon_{\bar{\nu}_\mathrm{e}}$) and the antineutrino number luminosity ($L_{\mathrm{n},\bar{\nu}_\mathrm{e}}$) by $\lambda_{\bar{\nu}_\mathrm{e}} = L_{\mathrm{n},\bar{\nu}_\mathrm{e}} \sigma_{\bar{\nu}_\mathrm{e},\mathrm{p}} \propto L_{\mathrm{n},\bar{\nu}_\mathrm{e}} \epsilon^2_{\bar{\nu}_\mathrm{e}}$ (see, e.g., Ref. [125]). Thus, higher electron antineutrino energies and luminosities lead to a larger production of free neutrons. In sum, the larger the entropy, the Y_e, and the electron antineutrino energies and luminosities, the more efficient is the bridging of the bottlenecks and the heavier nuclei are formed.

The neutrino-driven wind collides with the early slow-expanding supernova ejecta [36, 37, 39, 135–137] leading to a reverse shock. During the collision, kinetic energy is transformed into internal energy which results in an increase of temperature and density. The reverse shock has a significant impact on the nucleosynthesis in the νp-process [133, 134]. Since the reverse shock decelerates the expansion, the time period during which matter stays at high temperatures and high neutrino fluxes is extended. This leads to additional (p,γ) and (n,p) reactions, and thus heavier nuclei are formed.

Note that the νp-process is not terminated by the exhaustion of protons but it ends when the temperature drops below $T \approx 1$ GK and the (p,γ) reactions freeze out. Then (n,p), (n,γ) reactions and beta decays move matter back to stability.

Reference [121] studied the formation of lighter heavy elements in proton-rich winds. They found that lighter heavy elements are formed robustly under small variations of the wind parameters (see also Ref. [119]). However, lighter heavy elements are produced in proton-rich winds only for a successful νp-process, i.e., if the antineutrino energies and luminosities are high enough. Compared to slightly neutron-rich winds, the amount of heavy elements is rather low. Since mainly neutron-deficient isotopes are produced (see also Refs. [31, 132, 133]) proton-rich winds can explain the LEPP elements observed in UMP stars but not the solar LEPP [25].

3 Nuclear reactions in astrophysics

Nuclear reactions are one of the key ingredients in nucleosynthesis calculations where a large number of different types of nuclear reactions are important: emission and absorption of nucleons and nuclei, emission and absorption of photons (γ-rays) and leptons (electrons, neutrinos, and their antiparticles) [138]. Thus, nucleosynthesis calculations involve three of the four fundamental forces, i.e., nuclear strong, electromagnetic and nuclear weak forces. The quantity which is used in nucleosynthesis calculations is the reaction rate. We will explain the basic concepts of nuclear reactions rates in Sect. 3.1, and derive expressions for particle-induced reactions, photodisintegration reactions as well as electron, positron and neutrino captures, and decays. To understand the formation of the elements we have to follow the temporal evolution of the nuclear composition. In Sect. 3.2, we describe the concept of nuclear reaction networks and explain methods to solve the reaction network. In the absence of experiments, most of the reaction rates entering in the nucleosynthesis calculations are calculated with theoretical reaction codes based on the statistical Hauser-Feshbach model. We will give an overview of the determination of theoretical reaction rate based on the compound nucleus theory in Sect. 3.3 and describe different alpha optical potentials which mainly govern the (α, n) reaction rate uncertainties. This chapter follows Refs. [51, 139].

3.1 Basic concepts of thermonuclear reaction rates

A nuclear reaction is a process in which a projectile j interacts with a nucleus i and the interaction products, k and l, have a different identity than the incident particles. The nuclear cross section, σ, is a quantity to the describe the probability of a reaction $i + j \to k + l$, also referred to as $i(j,k)l$. The probability that a target i reacts with an incoming particle j is defined as

$$\begin{aligned} \sigma &\equiv \frac{\#\text{Number of reactions per target per time}}{\text{Flux of incoming particles}} \\ &= \frac{r/n_i}{n_j v}, \end{aligned} \tag{3.1}$$

where n_i and n_j are the number densities (i.e., number of particles N_i and N_j per volume V) of target and projectile, respectively. The second equality in Eq. (3.1) holds only for a constant relative velocity v between target and projectile. Then, the number of reactions per cm^3 and sec, r, can be written as $r = \sigma v n_i n_j$. However, in general, targets and projectiles follow velocity distributions, and then the reaction rate r is given by

$$r_{i,j} = \int \sigma\left(|\vec{v}_i - \vec{v}_j|\right) |\vec{v}_i - \vec{v}_j| \mathrm{d}n_i \mathrm{d}n_j. \tag{3.2}$$

The evaluation of the integral in Eq. (3.2) depends on the involved types of particles and their distributions. In the following, we will derive expressions for the reaction rate for different types of reactions.

3.1.1 Particle-induced reactions

For a projectile i and a target j in an astrophysical plasma, both obeying a thermal distribution described by the Maxwell-Boltzmann distribution, we have

$$\mathrm{d}n_x = n_x \left(\frac{m_x}{2\pi k_\mathrm{B} T}\right)^{3/2} \exp\left(-\frac{m_x v_x^2}{2k_\mathrm{B} T}\right) \mathrm{d}^3 v_x \equiv n_x \phi(\vec{v}_x) \mathrm{d}^3 v_x, \tag{3.3}$$

where m is the mass of the particle $x = (i,j)$, k_B is the Boltzmann constant, T is the temperature of the astrophysical plasma, and v is the velocity of the particle $x = i, j$. Therefore, Eq. (3.2) can be rewritten as

$$r_{i,j} = n_i n_j \int \sigma\left(|\vec{v}_i - \vec{v}_j|\right) |\vec{v}_i - \vec{v}_j| \phi(\vec{v}_i)\phi(\vec{v}_j) \mathrm{d}^3 v_i \mathrm{d}^3 v_j = n_i n_j \langle \sigma v \rangle_{i,j}. \tag{3.4}$$

In Eq. (3.4), $\langle \sigma v \rangle_{i,j}$ is the so-called velocity integrated cross section which is also referred to as reactivity. If we use center of mass and relative coordinates rather than individual ones, the velocity integrated cross section can be expressed as a function of the relative velocity v and the reduced mass $\mu = m_i m_j / \left(m_i + m_j\right)$

$$\langle \sigma v \rangle_{i,j} = \left(\frac{\mu}{2\pi k_\mathrm{B} T}\right)^{3/2} \int v \sigma(v) \exp\left(-\frac{\mu v^2}{2 k_\mathrm{B} T}\right) \mathrm{d}^3 v. \tag{3.5}$$

With $\mathrm{d}^3 v = 4\pi v^2 \mathrm{d}v$ and $E = \frac{1}{2}\mu v^2$ the integral in Eq. (3.5) becomes energy dependent

$$\langle \sigma v \rangle_{i,j} = \left(\frac{8}{\pi\mu}\right)^{1/2} (k_\mathrm{B} T)^{-3/2} \int_0^\infty E \sigma(E) \exp\left(-\frac{E}{k_\mathrm{B} T}\right) \mathrm{d}E. \tag{3.6}$$

Consequently, if the cross section $\sigma(E)$ of a nuclear reaction is experimentally or theoretically known, $\langle \sigma v \rangle_{i,j}$ can be easily determined, assuming that the participating nuclei follow Maxwell-Boltzmann statistics.

3.1.2 Photodisintegration reactions

If the projectile j is a photon, the interaction is a photodisintegration reaction. In a stellar plasma at thermodynamic equilibrium, the number density of photons is not constant, and depends on the stellar temperature and photon energy. Following the general description of $r_{i,j}$ (see Eq. (3.2)) and considering that photons are always moving with the speed of light c, and the target i is a nucleus obeying Maxwell-Boltzmann statistics, we find for the reaction rate of a photodisintegration reaction

$$r_{i,\gamma} = n_i \int_0^\infty c n_\gamma(E_\gamma) \sigma(E_\gamma)\, \mathrm{d}E_\gamma. \tag{3.7}$$

The decay constant, i.e., probability of a decay per nucleus per second, is given by

$$\lambda_{i,\gamma}(T) = \frac{r_{i,\gamma}}{n_i} = \int_0^\infty c n_\gamma(E_\gamma) \sigma(E_\gamma)\, \mathrm{d}E_\gamma. \tag{3.8}$$

The energy density of a photon with frequencies between ν and $\nu + \mathrm{d}\nu$ at a temperature T can be described by Planck's radiation law:

$$u(\nu)\, \mathrm{d}\nu = \frac{8\pi h \nu^3}{c^3} \frac{\mathrm{d}\nu}{\exp(h\nu/(k_\mathrm{B} T)) - 1}. \tag{3.9}$$

Since the energy of a photon is $E_\gamma = h\nu$, Eq. (3.9) can be rewritten as

$$u(E_\gamma)\, \mathrm{d}E_\gamma = \frac{8\pi}{(hc)^3} \frac{E_\gamma^3}{\exp\left(E_\gamma/(k_\mathrm{B} T)\right) - 1}\, \mathrm{d}E_\gamma. \tag{3.10}$$

The number of photons with energies between E_γ and $E_\gamma + \mathrm{d}E_\gamma$ per unit volume at a temperature T is

$$n_\gamma(E_\gamma)\, \mathrm{d}E_\gamma = \frac{u(E_\gamma)}{E_\gamma} \mathrm{d}E_\gamma = \frac{8\pi}{(hc)^3} \frac{E_\gamma^2}{\exp\left(E_\gamma/(k_\mathrm{B} T)\right) - 1}\, \mathrm{d}E_\gamma. \tag{3.11}$$

Therefore, the photodisintegration rate at a given temperature T can be expressed as

$$\lambda_{i,\gamma}(T) = \frac{8\pi}{h^3 c^2} \int_0^\infty \frac{E_\gamma^2}{\exp\left(E_\gamma/(k_\mathrm{B} T)\right) - 1} \sigma\left(E_\gamma\right)\, \mathrm{d}E_\gamma. \tag{3.12}$$

3.1.3 Forward and reverse reactions

The cross section $\sigma_{i,j\rightarrow k,l}$ of the reaction $i+j\rightarrow k+l$ is related to the cross section $\sigma_{k,l\rightarrow i,j}$ of the reverse reaction $k+l\rightarrow i+j$ because the two processes are invariant under time-reversal. For a given total energy, $\sigma_{i,j\rightarrow k,l}$ and $\sigma_{k,l\rightarrow i,j}$ are related by the phase space in the exit channel, or by the number of final states per unit energy interval in each case. The number of states available for momenta between p and $p+\mathrm{d}p$ is proportional to p^2 [140]. Thus, $\sigma_{i,j\rightarrow k,l}\propto p_{k,l}^2$ and $\sigma_{k,l\rightarrow i,j}\propto p_{i,j}^2$. The momentum p and the de Broglie wavelength are related by $\lambda=h/p$. The wave number k of a free particle is defined as $\lambda=2\pi/k$. This leads to $p=mv=\hbar k$. Then, we obtain (see also Ref. [141])

$$\frac{k_{i,j}^2\sigma_{i,j\rightarrow k,l}}{(1+\delta_{ij})}=\frac{k_{k,l}^2\sigma_{k,l\rightarrow i,j}}{(1+\delta_{kl})}. \tag{3.13}$$

This is the so-called principle of detailed balance, also referred to as reciprocity theorem. The factors δ_{ab} prevent the double counting of identical particles in the entrance channel. For identical particles, i.e., $a=b$, $\delta_{ab}=1$, otherwise $\delta_{ab}=0$. If particles with spins are involved, we have to take into account the density of the final states by their statistical weights. For a particle with spin J, there are $g=(2J+1)$ different states available where g is the degeneracy factor of the ground state. In an astrophysical plasma, the excited states of nuclei i and l are populated. To consider the contributions from excited states, g_i and g_j are expressed by the partition functions of these nuclei, i.e., $G_x=\sum_{\mathrm{n}} g_{x,n}\exp(-E_{\mathrm{n}}/(k_{\mathrm{B}}T))$. Hence, we get

$$\frac{k_{i,j}^2 G_i(2J_j+1)\sigma_{i,j\rightarrow k,l}}{(1+\delta_{ij})}=\frac{k_{k,l}^2 G_l(2J_k+1)\sigma_{k,l\rightarrow i,j}}{(1+\delta_{kl})}, \tag{3.14}$$

which can be rewritten as

$$\frac{\sigma_{k,l\rightarrow i,j}}{\sigma_{i,j\rightarrow k,l}}=\frac{G_i(2J_j+1)}{G_l(2J_k+1)}\frac{k_{i,j}^2(1+\delta_{kl})}{k_{k,l}^2(1+\delta_{ij})}. \tag{3.15}$$

Therefore, $\sigma_{k,l\rightarrow i,j}$ can be easily calculated if $\sigma_{i,j\rightarrow k,l}$ is experimentally or theoretically known. Equation (3.15) is valid for particles with rest mass as well as for photons. For particles with rest mass the wave number is given by $k=\sqrt{2\mu E}/\hbar$, and the momentum can be expressed as $p^2=\hbar^2k^2=2\mu E$. Then, we obtain

$$\frac{\sigma_{k,l\rightarrow i,j}}{\sigma_{i,j\rightarrow k,l}}=\frac{G_i(2J_j+1)}{G_l(2J_k+1)}\frac{\mu_{i,j}E_{i,j}}{\mu_{k,l}E_{k,l}}\frac{(1+\delta_{kl})}{(1+\delta_{ij})}, \tag{3.16}$$

where $E_{i,j}$ and $E_{k,l}$ are the center-of-mass energies of the forward and reverse reaction, respectively. For a reaction involving photons, the wave number is defined as $k=E/(\hbar c)$ and the momentum is given by $p^2=\hbar^2k^2=E_\gamma^2/c^2$. Thus, Eq. (3.15) leads to

$$\frac{\sigma_{\gamma,l\rightarrow i,j}}{\sigma_{i,j\rightarrow\gamma,l}}=\frac{G_i(2J_j+1)}{2G_l}\frac{2\mu_{i,j}c^2E_{i,j}}{E_\gamma^2}\frac{1}{(1+\delta_{ij})}, \tag{3.17}$$

using that the photon has only two polarization directions, i.e., $(2J_\gamma+1)=2$.

The forward rate and its corresponding reverse reaction rate involving only particles with rest mass are given by

$$N_{\mathrm{A}}\langle\sigma v\rangle_{i,j\rightarrow k,l}=\left(\frac{8}{\pi\mu_{i,j}}\right)^{1/2}\frac{N_{\mathrm{A}}}{(k_{\mathrm{B}}T)^{3/2}}\int_0^\infty E_{i,j}\sigma_{i,j\rightarrow k,l}\exp\left(-E_{i,j}/(k_{\mathrm{B}}T)\right)\mathrm{d}E_{i,j}, \tag{3.18}$$

$$N_{\mathrm{A}}\langle\sigma v\rangle_{k,l\rightarrow i,j}=\left(\frac{8}{\pi\mu_{k,l}}\right)^{1/2}\frac{N_{\mathrm{A}}}{(k_{\mathrm{B}}T)^{3/2}}\int_0^\infty E_{k,l}\sigma_{k,l\rightarrow i,j}\exp\left(-E_{k,l}/(k_{\mathrm{B}}T)\right)\mathrm{d}E_{k,l}, \tag{3.19}$$

respectively. The kinetic energies are related by $E_{k,l}=E_{i,j}+Q_{i,j\rightarrow k,l}$ where $Q_{i,j\rightarrow k,l}$ denotes the Q-value of the reaction. The Q-value describes the difference in masses (or in kinetics) before and after the reaction. Then, we get (see also Ref. [142])

$$\begin{aligned}\frac{N_\mathrm{A}\langle\sigma v\rangle_{k,l\to i,j}}{N_\mathrm{A}\langle\sigma v\rangle_{i,j\to k,l}} &= \left(\frac{\mu_{i,j}}{\mu_{k,l}}\right)^{1/2}\frac{\int_0^\infty E_{k,l}\sigma_{k,l\to i,j}\exp\left(-E_{k,l}/(k_\mathrm{B}T)\right)\,\mathrm{d}E_{k,l}}{\int_0^\infty E_{i,j}\sigma_{i,j\to k,l}\exp\left(-E_{i,j}/(k_\mathrm{B}T)\right)\,\mathrm{d}E_{i,j}}\\ &= \frac{G_i(2J_j+1)(1+\delta_{kl})}{G_l(2J_k+1)(1+\delta_{ij})}\left(\frac{\mu_{i,j}}{\mu_{k,l}}\right)^{3/2}\cdot\exp\left(-Q_{i,j\to k,l}/(k_\mathrm{B}T)\right).\end{aligned} \tag{3.20}$$

To derive an expression for the relationship between forward and reverse reaction rate if species k is a photon, we start from Eqs. (3.6) and (3.12). From Eq. (3.17) we receive

$$\frac{\lambda_{\gamma,l}}{N_\mathrm{A}\langle\sigma v\rangle_{i,j\to\gamma,l}} = \frac{\frac{8\pi}{h^3c^2}\int_0^\infty \frac{E_\gamma^2}{\exp\left(E_\gamma/(k_\mathrm{B}T)\right)-1}\frac{G_i(2J_j+1)}{G_l(1+\delta_{ij})}\frac{\mu_{i,j}c^2E_{i,j}}{E_\gamma^2}\sigma_{\gamma,l\to i,j}\,\mathrm{d}E_\gamma}{\left(\frac{8}{\pi\mu_{i,j}}\right)^{1/2}\frac{N_\mathrm{A}}{(k_\mathrm{B}T)^{3/2}}\int_0^\infty E_{i,j}\sigma_{i,j\to\gamma,l}\exp\left(-E_{i,j}/(k_\mathrm{B}T)\right)\,\mathrm{d}E_{i,j}}. \tag{3.21}$$

The energies are related by $E_{i,j}+Q_{i,j\to\gamma,l}=E_\gamma$. Besides, most capture reactions have Q-values larger than 0, elsewise nuclei l would be unstable by particle emission. In addition, many capture reactions have large Q-values (i.e., on the order of several MeV), thus the integration over E_γ will not start from zero but from a threshold energy of $E_\mathrm{threshold}=Q_{i,j\to\gamma,l}$. This implies $\exp\left(E_\gamma/(k_\mathrm{B}T)\right)-1\approx\exp\left(E_\gamma/(k_\mathrm{B}T)\right)$ and we obtain from Eq. (3.21) (see also Ref. [142])

$$\begin{aligned}\frac{\lambda_{\gamma,l}}{N_\mathrm{A}\langle\sigma v\rangle_{i,j\to\gamma,l}} &= \frac{\frac{8\pi}{h^3c^2}(k_\mathrm{B}T)^{3/2}\mu_{i,j}c^2}{\left(\frac{8}{\pi m_{i,j}}\right)^{1/2}N_\mathrm{A}}\frac{G_i(2J_j+1)}{G_l(1+\delta_{ij})}\cdot\frac{\int_0^\infty E_{i,j}\exp\left(-(E_{i,j}+Q_{i,j\to\gamma,l})/(k_\mathrm{B}T)\right)\sigma_{i,j\to\gamma,l}\,\mathrm{d}E_\gamma}{\int_0^\infty E_{i,j}\exp\left(-E_{i,j}/(k_\mathrm{B}T)\right)\sigma_{i,j\to\gamma,l}\,\mathrm{d}E_{i,j}}\\ &= \left(\frac{2\pi}{h^2}\right)^{3/2}\frac{\left(\mu_{i,j}k_\mathrm{B}T\right)^{3/2}}{N_\mathrm{A}}\frac{G_i(2J_j+1)}{G_l(1+\delta_{ij})}\exp\left(-Q_{i,j\to\gamma,l}/(k_\mathrm{B}T)\right).\end{aligned} \tag{3.22}$$

3.1.4 Electron, positron and neutrino captures

At high densities electrons become degenerate. The Fermi energy increases with $(\rho Y_\mathrm{e})^{2/3}$, and eventually overcomes the proton-neutron mass difference. Then, the existence of high energy electrons allow for electron capture reactions which are energetically prohibited by a negative Q-value:

$$\mathrm{e}^- + (Z,A)\to(Z-1,A)+\nu_\mathrm{e}. \tag{3.23}$$

Besides, the electron captures lead to a neutronization of the astrophysical plasma. Following again the general definition of a reaction rate (Eq. (3.2)), we obtain for the electron capture reaction rate

$$r_{i,\mathrm{e}^-} = \int \sigma_{\mathrm{e}^-}|\vec{v}_i-\vec{v}_{\mathrm{e}^-}|\mathrm{d}n_i\,\mathrm{d}n_{\mathrm{e}^-}. \tag{3.24}$$

Due to the vast mass difference between electrons (m_e =0.511 MeV) and nuclei ($m_\mathrm{u}\approx 931$ MeV) one can assume that the nuclei is at rest in the center of mass system, and the relative velocity on which the cross section σ_{e^-} depends can be described by the electron velocity. Therefore, similar to the photon-induced reactions where the relative velocity was c, the integral in Eq. (3.24) does not depend on nuclei and $\mathrm{d}n_i$ and can be rewritten as

$$r_{i,\mathrm{e}^-} = n_i\int\sigma_{\mathrm{e}^-}(v_{\mathrm{e}^-})v_{\mathrm{e}^-}\mathrm{d}n_{\mathrm{e}^-} = \lambda_{i,\mathrm{e}^-}(\rho,Y_\mathrm{e},T)\,n_i. \tag{3.25}$$

Note that the decay constant λ_{i,e^-} depends on the temperature, and due to the definition of the electron number density $n_{\mathrm{e}^-}=\rho N_\mathrm{A}Y_\mathrm{e}$ on the density of the astrophysical plasma and the electron fraction Y_e. Once the electron capture cross section σ_{e^-} is known, temperature and density determine whether $\mathrm{d}n_{\mathrm{e}^-}$ is treated as a Maxwell-Boltzmann or a Fermi distribution, which can be partially or fully degenerated, and relativistic.

Positrons are in thermal equilibrium with photons and electrons once the temperature is high enough ($T \gtrsim 1.022$ MeV) for photons to produce electron-positron pairs $\gamma + \gamma \rightarrow \mathrm{e}^- + \mathrm{e}^+$. Then positron captures become possible:

$$\mathrm{e}^+ + (Z,A) \rightarrow (Z+1,A) + \bar{\nu}_\mathrm{e}. \tag{3.26}$$

At high enough densities ($\rho > 10^{12}$ g cm^{-3}), the cross section for neutrino scattering on nuclei is large enough that neutrinos are captured by nuclei and become thermalized. Neutrino capture, i.e., $i + \nu \rightarrow \mathrm{e}^- + l$ or $i + \bar{\nu} + \mathrm{e}^+ + l$, is the inverse process of electron capture. Therefore, the neutrino capture rate $\lambda_{\nu(\bar{\nu})}(\rho Y_\mathrm{e}, T)$ can be calculated from the electron and positron capture rate using the reciprocity theorem, or by integrating over the neutrino distribution (similar to Eq. (3.25)).

Decays

For a beta or alpha decay with a half-life $\tau_{1/2}$, the reaction rate is given by

$$r_i = \lambda_i n_\mathrm{i}. \tag{3.27}$$

The decay constant λ_i and the half-life are related by $\lambda_i = \ln 2/\tau_{1/2}$. If the nucleus is in the ground state the decay half-life is a constant. At higher temperatures, excited states n with different decay constants can also be thermally populated. Then, the temperature dependent total decay constant of a nucleus is

$$\lambda_i(T) = \frac{\sum_n \lambda_{i,n}(2J_n + 1)\exp(-E_n/(k_\mathrm{B}T))}{G_i(T)}, \tag{3.28}$$

where $G_i(T) = \sum_n (2J_n + 1)\exp(-E_n/(k_\mathrm{B}T))$ is the partition function.

3.2 Nuclear reaction networks

Nuclear reaction networks follow the evolution of the composition of a system containing many species of nuclei. In the previous sections, we derived two types of expressions for the number of reactions per cm^3 per sec: 1) $r_{ij} = n_i n_j \langle \sigma v \rangle_{i,j}$ for particle-induced reactions; and 2) $r_i = \lambda_i n_i$ for decays, photodisintegrations, electron captures, etc. In the first expression we have to add a correction term because in a gas of identical particles each of the nuclei is double counted, once as a target and once as a projectile. Then, the number of reactions between particles i and j per cm^3 per sec is given by

$$r_{ij} = \frac{1}{1+\delta_{ij}} n_i n_j \langle \sigma v \rangle_{i,j}. \tag{3.29}$$

The correction term $\frac{1}{1+\delta_{ij}}$ prevents the double counting of reactions between identical particles: if i and j are identical particles $\delta_{ij} = 1$ and the reaction rate is divided by two. For three-body reactions, the correction which prevents double counting is $\Delta_{ijk} \equiv \delta_{ij} + \delta_{jk} + \delta_{ik} + 2\delta_{ijk}$ and without detailed derivation (for a detailed one see Ref. [142]) the reaction rate is given by

$$r_{ijk} = \frac{1}{1+\Delta_{ijk}} n_i n_j n_k \langle \sigma v \rangle_{i,j,k}. \tag{3.30}$$

The changes in the number densities of the involved nuclei in a reaction $i(j,k)l$ due to reactions rather than density changes are described by

$$\begin{aligned} \left(\frac{\partial n_i}{\partial t}\right)_\rho &= \left(\frac{\partial n_j}{\partial t}\right)_\rho = -r_{ij}, \\ \left(\frac{\partial n_k}{\partial t}\right)_\rho &= \left(\frac{\partial n_l}{\partial t}\right)_\rho = +r_{ij}. \end{aligned} \tag{3.31}$$

In an astrophysical plasma, a whole variety of different reactions which produce or destroy a nucleus i can take place simultaneously. Thus, we have

$$\left(\frac{\partial n_i}{\partial t}\right)_{\rho=\mathrm{const}} = \sum_j N_j^i r_j + \sum_{j,k} \frac{N_{j,k}^i}{1+\delta_{jk}} r_{jk} + \sum_{j,k,l} \frac{N_{j,k,l}^i}{1+\Delta_{jkl}} r_{jkl}. \tag{3.32}$$

The three sums on the right hand side of Eq. (3.32) describe the formation or destruction of nucleus i in possible one-, two-, three-body reactions, respectively. The N_i's specify how many nuclei of species i are produced (positive N_i) or destroyed (negative N_i). In most astrophysical environments the density is not constant. Therefore, to avoid changes which are only a result of density changes we use abundances instead of number densities. The abundance Y_i and the number density n_i of a nucleus i are related by

$$Y_i = \frac{n_i}{\rho N_\mathrm{A}}, \tag{3.33}$$

where ρ is the density of the astrophysical environment and N_A is the Avogadro constant. The time derivative of the abundance Y_i is

$$\dot{Y}_i = \frac{\dot{n}_i}{\rho N_\mathrm{A}} - \frac{n_i}{\rho N_\mathrm{A}} \frac{\dot{\rho}}{\rho}. \tag{3.34}$$

The relation between abundance Y_i and number density n_i of a nucleus i is based on the definition of the mass fraction X_i, i.e., the percentage of mass m_i (or density ρ_i) of nuclei of species i with respect to the total mass (density) of the system

$$X_i = \frac{\rho_i}{\rho} = \frac{n_i}{\rho N_\mathrm{A}} m_i N_\mathrm{A} = Y_i A_i. \tag{3.35}$$

The term $m_i N_\mathrm{A}$ is the total mass of a mole of particles i and defines the atomic weight. As a result of the definition of the mass fraction, all mass fractions must add up to one, i.e., $\sum_i X_i = 1$. If we rewrite Eq. (3.32) in terms of abundances we obtain the following set of differential equations

$$\dot{Y}_i = \sum_j N_j^i \lambda_j Y_j + \sum_{j,k} \frac{N_{j,k}^i}{1+\delta_{jk}} \rho N_\mathrm{A} \langle \sigma v \rangle_{j,k} Y_j Y_k + \sum_{j,k,l} \frac{N_{j,k,l}^i}{1+\Delta_{jkl}} \rho^2 N_\mathrm{A}^2 \langle \sigma v \rangle_{j,k,l} Y_j Y_k Y_l, \tag{3.36}$$

which is usually referred to as nuclear reaction network.

3.2.1 Solving the nuclear reaction network

In order to find the solutions of the reaction network one has to solve the system of coupled non-linear differential equations described in Eq. (3.36). Nuclear reaction networks consist of a large number of different reactions. The time scales of the strong, electromagnetic and weak reactions span a wide range, thus reaction networks are extraordinary stiff [138]. A more precise definition of a stiff system of equations $\dot{\vec{Y}}(\vec{Y})$ is that the eigenvalues λ_j of the Jacobian $\partial\dot{\vec{Y}}/\partial\vec{Y}$ obey the criteria

$$\begin{gathered} \Re(\lambda_j) < 0, \quad j = 1, \ldots, N \\ S = \frac{\max|\Re(\lambda_j)|}{\min|\Re(\lambda_j)|} \gg 1, \end{gathered} \tag{3.37}$$

where $\Re(\lambda_j)$ is the real part of the eigenvalue λ_j. The system of reaction rates is integrated with one step, self-starting algorithms. Since the errors in the rates are usually few percent or more, the greater precision of higher order methods does not lead to higher accuracy.

The differential equations constituting the nuclear reaction network present a typical initial value problem. The boundary conditions are given by the initial abundances of all nuclei considered in the network, and we want to find the abundances of these nuclei at a final time, or at some specific points in time. The network equations are integrated along a discrete list of points which is given by the time evolution of the hydrodynamic variables, i.e., temperature and density. The abundances at a future time $\vec{Y}(t+\Delta t)$, where Δt is the time step in the network, are calculated with a finite difference

$$\frac{\vec{Y}(t+\Delta t)-\vec{Y}(t)}{\Delta t}=(1-\theta)\dot{\vec{Y}}(t+\Delta t)+\theta\dot{\vec{Y}}(t). \tag{3.38}$$

For $\theta = 1$, Eq. (3.38) becomes the explicit, forward Euler method which requires the derivatives only at the beginning of the time step. If $\theta = 0$, Eq. (3.38) is the implicit backward Euler method which needs the derivative at the end of the time step. The explicit and implicit Euler methods are first-order accurate in time, thus the accuracy improves inversely proportional to the time step. In case of $\theta = 1/2$, Eq. (3.38) is the semi-implicit trapezoidal method which is second-order accurate in time. For most reaction networks, the implicit Euler method is commonly applied [143], except for big bang nucleosynthesis networks where the implicit trapezoidal method is used [144].

The solution of the backward Euler method is equivalent to finding the zeros of equation

$$\frac{\vec{Y}(t+\Delta t)-\vec{Y}(t)}{\Delta t}-\dot{\vec{Y}}(t+\Delta t)=0. \tag{3.39}$$

This set of nonlinear equations can be solved with the Newton-Raphson method which is a root finding algorithm based on a Taylor series expansion. Applying the Newton-Raphson method leads to

$$\vec{Y}^{\text{new}}(t+\Delta t)=\vec{Y}^{\text{old}}(t+\Delta t)-\mathbf{J}^{-1}\left(\frac{\vec{Y}^{\text{old}}(t+\Delta t)-\vec{Y}(t)}{\Delta t}-\dot{\vec{Y}}^{\text{old}}(t+\Delta t)\right). \tag{3.40}$$

To solve this equation one has to invert the Jacobian $\mathbf{J}$ given by

$$\mathbf{J}\equiv\frac{1}{\Delta t}-\frac{\partial\dot{\vec{Y}}(t+\Delta t)}{\partial\vec{Y}(t+\Delta t)}, \tag{3.41}$$

at each iteration step. The backward Euler method has comparable low computational costs per time step, because one has only to evaluate the right-hand side of Eq. (3.40), perform one matrix inversion and a back substitution. In contrast to higher order computationally more expensive methods, first order methods cannot estimate the accuracy of a time step. As a compensation, we check the mass conservation $\left(\sum_{i=1}^{N}X_i=1\right)$ at every iteration and demand that the difference between the sum over the mass fractions and 1 is less than a certain threshold. Otherwise an additional Newton-Raphson step is performed. If the convergence is not reached within three iteration steps, the time step is cut in half and the time integration starts again with the new time step. To reach convergence as fast as possible the time step is adaptive:

$$\Delta t\leq\eta\frac{Y_i}{\mathrm{d}Y_i/\mathrm{d}t}, \tag{3.42}$$

where η is a positive constant. Moreover, we take into account only abundances that are larger than 10^{-10}. In addition, we demand that the thermodynamic variables, i.e., temperature and density, do not change within 5% and the increase of the time step is not larger than a factor of two compared to the subsequent step. Furthermore, the time step is limited by the time step of the trajectory.

3.2.2 Matrix sparseness

For large networks, $N = 100$–3000 matrix equations must be solved. The general solution of a dense matrix scales with $O(N^3)$ which makes large networks computationally very expensive. In principle, every species reacts with each of the hundreds of others, and thus leading to a dense Jacobian matrix. But the Coulomb term in the nuclear potential ($\propto Z_i Z_j$) causes captures of free neutrons, H and He isotopes to occur much faster than fusions of heavier nuclei. Besides, photodisintegration reactions tend to eject nucleons or alpha particles. Therefore, it is sufficient to consider only about twelve reactions for every species linking it to its neighbors by n, p, α or γ capture and release a different one of the four. An exception are the few heavy ion reactions where the lack of light nuclei causes the heavy ion collisions to dominate (e.g., C and O burning stages). Figure 3.1 illustrates the evaluation of the Jacobian for an example network with 789 nuclei [90]. Matrix elements which are zero are colored in white. Neutrons, protons and alpha particles are linked to almost all other nuclei. Besides, every nucleus is connected to itself which is represented by the non-zero matrix elements on the diagonal. Since nuclei are sorted by elements and reactions involving alpha particles link isotopic chains, the diagonal band width ΔD is approximately 4 times the mean number of isotopes per element. The border width ΔB describes the location of the heaviest fusion partners. The Jacobian matrix is quite sparse, i.e., large fraction of matrix elements is zero. Performing operations on these zero elements during a calculation would be a waste of computational resources. Best results for small matrices (i.e., $N < 100$) are achieved with machine optimized dense solvers (e.g., LAPACK [145]) or matrix specific solvers generated by symbolic processing [146, 147]. For larger networks, generalized sparse solvers, e.g., Intel's PARDISO matrix solver [148], are used.

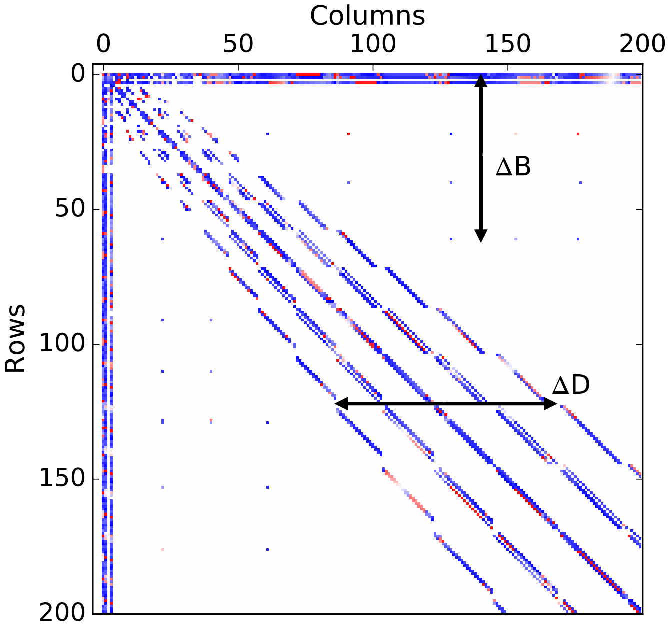

Figure 3.1: Graphical illustration of the sparseness of the Jacobian matrix [90]. The filled squares represent non-zero matrix elements.

3.2.3 Nuclear statistical equilibrium

At high enough temperatures ($T \gtrsim 6$ GK [138, 149]), the strong and electromagnetic reactions are in equilibrium. Then, every nucleus is connected to every other by reactions which proceed in both directions. This is the so-called nuclear statistical equilibrium (NSE). During NSE, the abundances are fully determined by the thermodynamic conditions, i.e., temperature, density, and Y_e. Since the weak interactions are not in equilibrium, we also have to follow their history. The assumption of NSE decreases the number of independent variables which greatly reduces the computational costs of the nucleosynthesis calculation. The NSE abundances also depend on binding energies and partition functions. For stable and particularly for unstable nuclei, these quantities are better known than reaction rates [150]. To derive an expression for the abundances during NSE one can either use chemicals potentials or detailed balance (see, e.g., Refs. [138, 151–154]). We will derive an expression for the NSE abundances using chemical potentials. For NSE conditions, we can apply the following thermodynamic relations

$$\mu(Z,N)+\mu_{\mathrm{n}}=\mu(Z,N+1), \tag{3.43}$$
$$\mu(Z,N)+\mu_{\mathrm{p}}=\mu(Z+1,N), \tag{3.44}$$

which correspond to neutron and proton captures. Let us assume a nucleus (Z,A) which consists of Z protons and $(A-Z)$ neutrons, and is in equilibrium with these free nucleons. For such an equilibrium the nucleus can be created by proton and neutron capture links, equivalent to $(A-Z)$ neutrons + Z protons $\leftrightarrows (Z,A)$ and the chemical potential of the nucleus can be described in terms of the chemical potentials of the free nucleons

$$\mu_{(Z,A)}=Z\mu_{\mathrm{p}}+N\mu_{\mathrm{n}}. \tag{3.45}$$

Since nuclei and nucleons follow Boltzmann statistics, the chemical potentials can be written as

$$\mu_i=m_ic^2+k_{\mathrm{B}}T\ln\left[\rho N_{\mathrm{A}}\frac{Y_i}{G_i}\left(\frac{2\pi\hbar^2}{m_ik_{\mathrm{B}}T}\right)^{3/2}\right]. \tag{3.46}$$

Inserting Eq. (3.46) into Eq. (3.45) leads to the so-called Saha equation

$$Y(Z,A)=G(Z,A)\left(\rho N_{\mathrm{A}}\right)^{A-1}\frac{A^{3/2}}{2^A}\left(\frac{2\pi\hbar^2}{m_{\mathrm{u}}k_{\mathrm{B}}T}\right)^{\frac{3}{2}(A-1)}\exp\left[B(Z,A)/(k_{\mathrm{B}}T)\right]Y_{\mathrm{n}}^{A-Z}Y_{\mathrm{p}}^{Z}, \tag{3.47}$$

with $m_{\mathrm{n}}\approx m_{\mathrm{p}}\approx m_u$, $m_{(Z,A)}\approx Am_{\mathrm{u}}$, and $B(Z,A)=\left((A-Z)m_{\mathrm{n}}c^2+Zm_{\mathrm{p}}c^2-m_{(Z,A)}c^2\right)$. Equation (3.47) expresses that the NSE abundance of a nucleus (Z,A) for a given temperature and density only depends on the abundances of the free neutrons (Y_{n}) and protons (Y_{p}), its binding energy $B(Z,A)$ and partition function $G(Z,A)$. When calculating NSE abundances one has to consider two constraints: mass conservation $\left(\sum_i A_i\cdot Y_i=1\right)$ and charge conservation $\left(\sum_i Z_i\cdot Y_i=Y_{\mathrm{e}}\right)$. Equation (3.47) indicates that high temperatures favor light nuclei, see term $(k_{\mathrm{B}}T)^{-\frac{3}{2}(A-1)}$, because the Planck distribution contains more photons with high energies which photodisintegrate heavy nuclei. The term (ρ^{A-1}) expresses that at high densities large nuclei are favored due to the more occurrent collisions. Besides, the term $\exp\left[B(Z,A)/(k_{\mathrm{B}}T)\right]$ indicates that for intermediate conditions the formation of the most bound nuclei (Fe-group nuclei) is favored. NSE breaks down when the slowest reactions fall out of equilibrium, i.e., $T\approx 6$ GK. But, different regions of the nuclide chart are still in equilibrium and are linked via reactions that are not in equilibrium anymore. This is the so-called quasi-statistical equilibrium (for more information see Refs. [69, 138, 149]).

3.2.4 WINNET reaction network

Our nucleosynthesis calculations are performed with the WINNET reaction network [155, 156]. The nucleosynthesis calculations start at a temperature around $T\approx 10$ GK, and we assume nuclear statistical equilibrium until the temperature drops below $T=8$ GK. The weak rates are considered from the beginning of the calculations, thus allowing Y_e to evolve during the NSE phase. Neutrons and protons dominate the initial abundances and its ratio is described by the initial Y_{e}. We include neutrino reactions on nucleons [31], and we choose the neutrino energies and luminosities, which are also used as network input parameters, so that they are consistent with the initial Y_{e} selected in our calculations (see Ref. [55] for their relationship).

We include 4412 neutron- and proton-rich nuclei as well as stable ones from H to Ir. The nuclear reaction rates are taken from the JINA ReaclibV2.0 [157] reaction rate library. An exception are the (α,n) rates and their inverse for all isotopes with $26<Z<45$ in our sensitivity study (chapter 5), which are calculated with the reaction code TALYS 1.6 [158] (see Sect. 5.2 for more details). We do not fit the (α,n) rates from TALYS following the Reaclib prescription but interpolate them. This prevents artificial divergences in the calculated rates which can influence our sensitivity study. The theoretical weak interaction rates are the same as in Ref. [31].

3.3 Determination of theoretical reaction rates

For most of the nuclei involved in the wind nucleosynthesis, even stable ones, the experimental information are scarce. In addition, experiments are usually restricted to energies which are too high for astrophysical applications. The cross sections can not be used directly but must be extrapolated to lower energies which involves serious difficulties. Therefore, we need reliable theoretical approaches which provide the required information, i.e., reaction rates. In the relevant mass and energy range, the dominant reaction mechanism is the compound nucleus formation (sometimes also referred to as statistical Hauser-Feshbach model) which will be described in Sect. 3.3.1. The reaction codes such as TALYS [158], NON-SMOKER [159], or CIGAR [160], used to calculate theoretical reaction rates, are all based on the compound nucleus theory. Nonetheless, they can exhibit substantial differences due to technical differences in the methods and algorithms used to solve the Hauser-Feshbach equations, different models and/or data bases to extract the nuclear physics inputs entering into the reaction rate calculation, and additional reaction mechanisms going beyond the Hauser-Feshbach formalism (e.g., direct or preequilibrium rates) are included in some reaction codes (see Ref. [48]).

3.3.1 Compound nucleus theory

The nuclear reaction between a projectile and target forming a new compound nucleus can be described by solutions Ψ of the Schrödinger equation. In one dimension, the Schrödinger equation is given by

$$\left[-\frac{\hbar^2}{2m}\frac{\mathrm{d}^2}{\mathrm{d}x^2}+V\right]\Psi = E\Psi, \tag{3.48}$$

where m is the mass of the projectile and V is the potential. The probability of a reaction can be measured by the ratio of the incoming and outgoing flux which is also referred to as transmission coefficient T:

$$T = \frac{j_f}{j_i} = \frac{k_f|\Psi_f|^2}{k_i|\Psi_i|^2}. \tag{3.49}$$

Here, Ψ_i and Ψ_f are the incoming and outgoing wave function, respectively, and k is the wave number. The transmission coefficient for a charged particle with charge Z_i penetrating through the Coulomb barrier of a nucleus with charge Z_j is given by

$$\begin{aligned} T &= \exp(-2\pi\eta), \\ \eta &= \sqrt{\frac{m}{2E}}\frac{Z_i Z_j e^2}{\hbar}, \end{aligned} \tag{3.50}$$

where η is the so-called Sommerfeld parameter. According to Eq. (3.50) the probability that a charged particle reaction occurs becomes smaller for larger charges of projectile and target, and it increases with increasing bombarding energy.

The cross section of a nuclear reaction is related to the sum of transmission coefficients over all possible angular momenta (see, e.g., Ref. [161])

$$\sigma = \frac{\pi}{k^2}\sum_{l=0}^{\infty}(2l+1)\,T_l, \tag{3.51}$$

where l is the angular momentum, $\hbar k$ and T_l are the momentum and transmission coefficients of incoming particles, respectively. Note, that the cross section in Eq. (3.51) is not valid for the ground state of the compound nucleus. The projectile and target create a compound nucleus at the excitation energy $Q+E$, with Q and E being the reaction Q-value and center of mass energy of the projectile, respectively. The excited compound nucleus can again decay via electromagnetic transitions into lower states of the compound nucleus (i.e., γ-decay), or particle emission into another nucleus. For low energy projectiles, γ-transitions will dominate in most cases. Besides, s-waves ($l = 0$) will dominate at low energies which leads to the following approximation of the nuclear cross section:

$$\sigma \approx \frac{\pi}{k^2}T_{l=0}, \tag{3.52}$$

with $k = \sqrt{2\mu E}/\hbar$ and μ being the reduced mass of the target-projectile system. With the approximated charged particle transmission coefficient ($T_0 = \exp(-2\pi\eta)$, see Eq. (3.50)), we can estimate the energy dependence for charged particle reactions at low energies:

$$\begin{aligned}\sigma = \frac{\pi}{k^2}\exp(-2\pi\eta) = \frac{\hbar^2\pi}{2\mu E}\exp(-2\pi\eta) \\ \eta = \sqrt{\frac{\mu}{2E}}\frac{Z_i Z_j e^2}{\hbar}.\end{aligned} \tag{3.53}$$

Consequently, for $l = 0$, the only energy dependence is due to η and E, and the so-called astrophysical S-factor

$$S(E) = \sigma E \exp(2\pi\eta), \tag{3.54}$$

is a constant.

Equation (3.51) has been only derived for particles without spin. Let us now consider a target j and projectile i with spins I_i and I_j which form the channel spin $\vec{S} = \vec{I_i} + \vec{I_j}$. The channel spin can have possible values from $|I_i - I_j|$ to $I_i + I_j$. The total number of possible spin orientations is

$$\sum_{S=|I_i-I_j|}^{|I_i+I_j|}(2S+1) = \frac{(2I_i+1)(2I_j+1)}{1+\delta_{ij}}. \tag{3.55}$$

The latter term takes into account that the wave function is symmetric if two particles are identical. The transmission coefficient describes the probability to form the compound nuclear state (E, J, π) at the excitation energy E, with spin J and parity π via all possible channel spin and angular momentum combinations. It is given by

$$T(E,J,\pi) = \sum_{l=|J-S|}^{J+S}\sum_{|I_i-I_j|}^{I_i+I_j} T_{lS}(E). \tag{3.56}$$

Thus, Eq. (3.51) can be rewritten as

$$\sigma(E) = \frac{\pi}{k^2}\frac{(1+\delta_{ij})}{(2I_i+1)(2I_j+1)}\sum_{J,\pi}(2J+1)T(E,J,\pi). \tag{3.57}$$

If the compound nucleus decays into particle k and additional into nucleus l, we have to take into account the probability of that outgoing channel k, i.e., $P_k = T_k/\sum_\mathrm{n} T_\mathrm{n}$, where n sums over all possible decay channels. If the decay of the compound nucleus is independent of its initial channel, the cross section of these combined reactions is given by

$$\sigma_i(j,k) = \frac{\pi}{k_j^2}\frac{(1+\delta_{ij})}{(2I_i+1)(2I_j+1)}\sum_{J,\pi}(2J+1)\frac{T_j(E,J,\pi)T_k(E,J,\pi)}{T_\mathrm{tot}(E,J,\pi)}. \tag{3.58}$$

This cross section is usually referred to as Hauser-Feshbach formula or statistical model formula.

At low energies, individual resonances can dominate a cross section. The shapes of the individual resonances are characterized by a Lorentz function in the Breit-Wigner resonance formula

$$\sigma(j,k) = \frac{\pi^2}{k_j^2}\frac{(1+\delta_{ij})}{(2I_i+1)(2I_j+1)}\sum_n(2J_n+1)\frac{\Gamma_{j,n}\Gamma_{k,n}}{(E-E_n)^2+(\Gamma_n/2)^2}. \tag{3.59}$$

The partial widths of the individual decay channels sum up to the width, Γ_n, of a resonant state n, i.e., $\Gamma_n = \Gamma_{j,n} + \Gamma_{k,n} + \dots$. The width of a resonant state denotes the stability of the state because a level with a width Γ can only exist for a time interval τ. The quantities Γ and τ are related by the Heisenberg uncertainty principle $\Gamma \approx \hbar/\tau$.

The statistical Hauser-Feshbach model averaging over resonances can be applied for a high level density in the compound nucleus at the appropriate excitation energy. A high level density means that the nucleus can equilibrate in the classical compound nucleus picture. The only required condition is that the number of resonances is large at the appropriate bombarding energies which allows to describe the cross section by average transmission coefficients. The Q-value of an alpha capture reaction is usually larger than the one for a neutron or proton capture reaction. This leads to the formation of the compound nucleus at a high excitation energy and justifies the application of the Hauser-Feshbach formalism for alpha capture reactions that are the focus of my work. Due to the small variation of the Q-value of an alpha capture reaction with the N/Z ratio of a nucleus, the requirements to use the compound nucleus theory are fulfilled near stability as well as the neutron and proton drip lines.

3.3.2 Optical potentials

The averaged transmission coefficients describe the absorption of an incident particle by a nucleus via an optical potential. The optical potential consists of two parts: one covers the elastic scattering part in the reaction, and the other includes all competing non-elastic channels. When solving the Schrödinger equation with a complex optical potential, one obtains a prediction of observables such as the elastic angular distribution and polarisation, the reaction and total cross section, and for low energies the s, p-wave strength functions and the potential scattering radius [158]. If the optical potential determines the nuclear reaction very well, it can reliably predict these observables for energies and nuclei for which no measurements exist. The optical model is defined as (following the descriptions of Ref. [48])

$$U(r,E) = V(r,E) + iW(r,E) + V_c(r,E), \tag{3.60}$$

where $V(r,E)$ and $W(r,E)$ denote the real and imaginary part, respectively, and $V_c(r,E)$ is the Coulomb potential which is described by a uniform charged sphere of a reduced radius $R_c = r_c A^{1/3}$. The real term $V(r,E)$ consists of a volume-central potential $V_v(r,E)$ and a spin-orbit potential $V_{so}(r,E)$ given by

$$V_v(r,E) = -\frac{V_v(E)}{1+\exp([r-R_v]/a_v)}, \tag{3.61}$$

and

$$V_{so}(r,E) = -\left(\frac{\hbar}{m_\pi c}\right)^2 \frac{V_{so}(E)}{r a_{so}} \frac{\exp([r-R_{so}]/a_{so})}{(1+\exp([r-R_{so}]/a_{so}))^2}, \tag{3.62}$$

where m_π is the pion mass. The imaginary part $W(r,E)$ has a volume-central $W_v(r,E)$, a spin-orbit $W_{so}(r,E)$ and a surface-central $W_d(r,E)$ part which are

$$W_v(r,E) = -\frac{W_v(E)}{1+\exp(r-R_v)/a_v}, \tag{3.63}$$

$$W_{so}(r,E) = -\left(\frac{\hbar}{m_\pi c}\right)^2 \frac{W_{so}(E)}{r a_{so}} \frac{\exp(r-R_{so})/a_{so}}{(1+\exp(r-R_{so})/a_{so})^2}, \tag{3.64}$$

and

$$W_d(r,E) = 4W_d(E)\frac{\exp(r-R_d)/a_d}{(1+\exp(r-R_d)/a_d)^2}. \tag{3.65}$$

3.3.3 Alpha optical potentials

In Refs. [48, 162], it has been shown that the uncertainties arising in the theoretical calculation of (α, n) reaction rates are mainly due to different alpha optical potentials for the temperatures relevant for the weak r-process. In the following, we will give an overview about the different alpha optical potentials which are available in TALYS and we use to estimate the (α, n) reaction rate uncertainty in our nucleosynthesis calculations.

- Spherical alpha optical potential

  The global alpha optical potential (see, e.g., Ref. [163]) is given by the spherical proton and neutron optical potentials [164]. The real term of Eq (3.60) is given by the following volume-central potential:

  $$V(r,E) = -2\frac{2\sum_{i=\mathrm{n,p}} V_{\mathrm{v}}^{i}(E/4)}{1+\exp\left([r-R_{\mathrm{v}}]/a_{\mathrm{v}}\right)}. \tag{3.66}$$

  The imaginary part of Eq. (3.60) is composed of a volume-central $W_{\mathrm{v}}(r,E)$ and a surface-central $W_{\mathrm{d}}(r,E)$ term:

  $$W_{\mathrm{v}}(r,E) = -\frac{2\sum_{i=\mathrm{n,p}} W_{\mathrm{v}}^{i}(E/4)}{1+\exp\left(r-R_{\mathrm{v}}\right)/a_{\mathrm{v}}}, \tag{3.67}$$

  $$W_{\mathrm{d}}(r,E) = 4\frac{2\sum_{i=\mathrm{n,p}} W_{\mathrm{d}}^{i}(E/4)\exp\left(r-R_{\mathrm{d}}\right)/a_{\mathrm{d}}}{\left(1+\exp\left(r-R_{\mathrm{d}}\right)/a_{\mathrm{d}}\right)^{2}}. \tag{3.68}$$

  The functions $V_{\mathrm{v}}(E)$, $W_{\mathrm{v}}(E)$, $W_{\mathrm{d}}(E)$, $V_{\mathrm{so}}(E)$ and $W_{\mathrm{so}}(E)$ are described in Eqs. (4.8)-(4.9), and Tabs. 4.1 and 4.2 of Ref. [158] for neutrons and protons, respectively. Note that TALYS uses the global alpha optical potential as default one.

- Alpha optical potential of McFadden and Satchler

  The alpha optical potential of McFadden and Satchler [165] is based on a simplified version of the optical potential which only consists of a volume-central real part, $V_{\mathrm{v}}(r,E)$, an imaginary part, $W_{\mathrm{v}}(r,E)$, and a Coulomb potential term, V_{c}, with $r_{\mathrm{c}} = 1.3$ fm. This alpha optical potential was obtained by adjusting the fit parameters to elastic scattering data of 24.7 MeV alpha particles on a large sample of nuclei, and consequently is limited. The NON-SMOKER code uses this alpha optical potential as default one.

- Alpha optical potential of Demetriou-Grama-Goriely

  In the alpha optical potential of Demetriou, Grama and Goriely [166] the Coulomb term $V_{\mathrm{c}}(r,E)$ assumes a uniform charged sphere with a reduced radius $r_{\mathrm{c}} = 1.25$ fm. The real term $V(r,E)$ is described by

  $$V(r,E) = \lambda V_{\mathrm{DF}}(r,E), \tag{3.69}$$

  where λ denotes a strength parameter and the potential $V_{\mathrm{DF}}(r,E)$ is calculated with the double-folding model of Ref. [167]. The imaginary part of the potential is given by a Wood-Saxon function (see, e.g., Ref. [161]). TALYS offers three different formulations of $W(r,E)$. In one option, $W(r,E)$ consists only of a central volume term with geometrical parameters described in Eq. (17) and Tab. I of Ref. [166]), and an energy dependency given by Eqs. (22)-(24) and Tab. I in Ref. [166]). The second option of $W(r,E)$ is related to the first one but with geometrical parameters described in Eq. (20) and Tab. II of Ref. [166]). The surface term has the same energy dependence as the volume term and is derived from the same Wood-Saxon function but has only 90% of its depth. The third option has in addition to the second one a damping function for the surface term which describes the decrease of the surface absorption with increasing energies (see Ref. [166]).

4 Astrophysical uncertainties in neutron-rich winds

In the following chapter, we want to systematically study the astrophysical uncertainties in slightly neutron-rich winds and present typical abundance patterns. Since a systematic study using trajectories from hydrodynamic simulations is computationally very expensive and there are still uncertainties in the core-collapse supernova and wind evolution, we rely on steady-state wind trajectories. We will give a short overview about the uncertainties in neutrino-driven winds in Sect. 4.1. Afterwards, we will emphasize the importance of studying the impact of astrophysical uncertainties on the nucleosynthesis (Sect. 4.2). The calculation of the steady-state trajectories will be described in Sect. 4.3. Besides, we will compare a trajectory from a hydrodynamic simulation with a steady-state trajectory in Sect. 4.3.2. Finally, we describe and compare the different abundance patterns obtained from the steady-state trajectories (Sect. 4.4). Parts of the content presented in this chapter are published in Bliss *et al.* (2017) [168] and Bliss *et al.* (2018) [169] as results of an ongoing project together with Almudena Arcones, Fernando Montes and Jorge Pereira.

4.1 Uncertainties in the evolution of neutrino-driven winds

The neutrino cooling of the neutron star leads to the evolution of the wind and the consequent variations of the wind parameters (electron fraction, entropy, and expansion time scale). The evolution of temperature and density in neutrino-driven winds varies for different progenitors, explosion energies, anisotropic evolutions of the explosion, and the ejection time after bounce (see, e.g., Refs. [36, 37, 39]). Consequently, to obtain a complete picture of the nucleosynthesis occurring in neutrino-driven winds, one needs a large number of three-dimensional simulations following the core-collapse supernova explosion and the subsequent neutrino-driven wind evolution for few seconds and for different progenitors. This is from a computational point of view far from being possible. Moreover, there are still uncertainties in the core-collapse supernova mechanism [42, 43]. In addition, neutrino matter interactions on the surface of the neutron star [120, 126, 170], neutrino oscillations [115, 124], rotation and magnetic fields [103, 171, 172] have an impact on the wind evolution. In the presence of the uncertainties in the evolution of the neutrino-driven wind, we explore the impact of the wind parameters using steady-state wind trajectories. Even if this cannot determine the integrated nucleosynthesis in the neutrino-driven wind, it helps to understand the dependency of the abundances on the astrophysical conditions and to put constraints on the wind parameters based on observations [121, 133] and chemical evolution [173].

4.2 Impact of wind parameters on the nucleosynthesis in neutron-rich winds

In neutron-rich winds ($0.4 \lesssim Y_\mathrm{e} \lesssim 0.5$), a weak r-process [30] can produce the lighter heavy elements, including Sr, Y, and Zr up to (possibly) Ag [23, 119, 129, 174]. In the following, we want to emphasize why it is important to study the impact of astrophysical uncertainties on the wind nucleosynthesis. Here, we use a trajectory from a hydrodynamic simulation because the electron fraction, entropy, and expansion time scales cannot be varied independently in steady-state models. We vary Y_e because this is the quantity that is more uncertain from hydrodynamic simulations. Furthermore, a variation of entropy and expansion time scale is not fully consistent with the simulations (for a sensitivity study to entropy and expansion time scale see, e.g., Refs. [102, 111, 119]). We use a trajectory obtained from spherically symmetric hydrodynamic simulations of neutrino-driven winds [36]. The trajectory is ejected 9 s after bounce and has an initial entropy of $S \approx 86\ \mathrm{k_B/nuc}$ and an expansion time scale of $\tau = 11$ ms. The variations in the abundance pattern for different electron fractions are illustrated in Fig. 4.1. For all Y_e, the abundance pattern exhibits odd-even effects due to the alpha capture reactions which are the main mechanism to reach heavier elements in neutron-rich neutrino-driven winds. Figure 4.1 indicates that the smaller the Y_e, the heavier elements are formed. For $Y_\mathrm{e} = 0.45$, elements up to silver are synthesized, whereas for $Y_\mathrm{e} = 0.49$ we do not reach heavier elements than zirconium. Note the strong decrease in the abundances beyond $Z = 40$ for $Y_\mathrm{e} = 0.49$. The reason for this is that for an electron fraction close to $Y_\mathrm{e} = 0.50$ the nucleosynthesis path moves close to or even along the valley of stability and reaches the neutron shell closure $N = 50$ at high atomic numbers. There are not enough free neutrons available that the nucleosynthesis path efficiently overcomes the neutron shell closure and evolve further beyond. Therefore, matter accumulates around $N = 50$ until the nucleosynthesis path decays back to stability. This explains the large abundances for Sr, Y, Zr, and the drop in the abundances beyond. For smaller electron fractions, the nucleosynthesis path overcomes $N = 50$ at lower Z. Due to the larger amount of free neutrons the nucleosynthesis path better overcomes the neutron shell closure, and thus heavier elements are reached. But not only the heaviest synthesized element changes, there are also differences at lower atomic numbers. The elemental abundances for atomic numbers up $Z=31$ are largest for $Y_e = 0.49$, whereas for $37 \leq Z \leq 38$ we obtain the highest abundances for $Y_e = 0.47$. Any variation of the nucleosynthesis evolution, i.e., here different Y_e, leads to different abundance patterns (see also Ref. [119]). It is interesting to understand the different patterns for Sr, Y, and Zr since these variations are also observed in the elemental abundances of old stars [15, 24, 173, 175]. In our calculations Sr, Y, and Zr show three typical patterns (see Fig. 4.1):

1. $Y(\mathrm{Sr}) < Y(\mathrm{Y}) < Y(\mathrm{Zr})$,

2. $Y(\mathrm{Sr}) \lesssim Y(\mathrm{Zr})$ and $Y(\mathrm{Sr}) > Y(\mathrm{Y})$,

3. $Y(\mathrm{Sr}) > Y(\mathrm{Y}) > Y(\mathrm{Zr})$.

The third case occurs when the electron fraction is close to 0.5, then the path moves close to or even along stability and Sr, Y, and Zr are the tail of the abundances (see above). For lower Y_e, the abundances reach heavier elements and this explains the trend of $Y(\mathrm{Sr}) \lesssim Y(\mathrm{Zr})$.

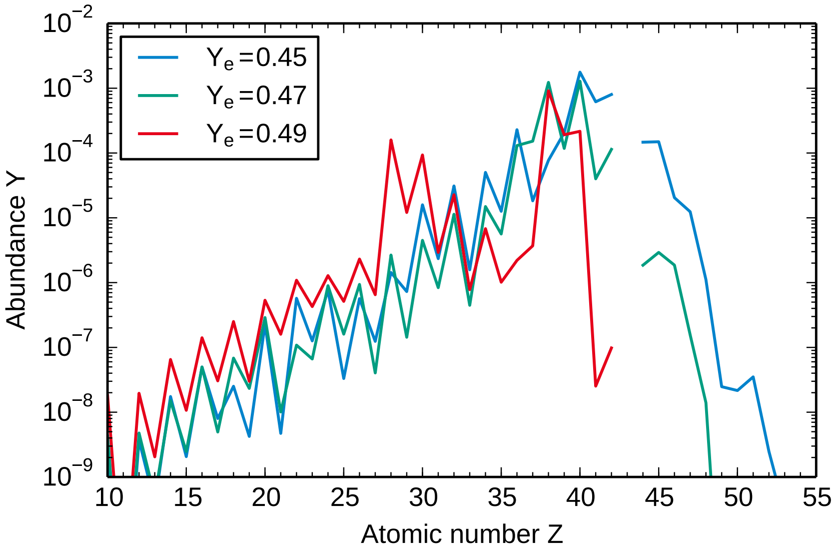

Figure 4.1: Elemental abundances, i.e., $Y(Z) = \sum_A Y(Z,A)$, for a trajectory ejected 9 s after bounce and different $Y_e = 0.45$, 0.47, and 0.49.

4.3 Calculation of the steady-state trajectories

A fully self-consistent study of the uncertainties in the astrophysical conditions requires to analyze all possible wind parameters. We have already explained in Sect. 4.1 that a study based on hydrodynamic trajectories from a computational point of view is not feasible. Thus, our strategy is to explore different astrophysical conditions in neutrino-driven winds with steady-state trajectories (see Refs. [55, 101–104, 111]). The steady state trajectories are calculated with a code written by Maximilian Witt [176] following Ref. [102]. This code includes general relativity corrections. The input parameters in the calculations are the mass (M_{ns}) and the radius (R_{ns}) of the neutron star, and the luminosities $\left(L_{\nu_e}\text{ and }L_{\bar{\nu}_e}\right)$ and the energies $\left(\langle E_{\nu_e}\rangle\text{ and }\langle E_{\bar{\nu}_e}\rangle\right)$ of the electron neutrinos and antineutrinos, respectively.

The relation between the neutron star mass and radius is described by the equation of state (EoS). Commonly used EoSs are that of Lattimer and Swesty [177] and Shen *et al.* [178]. The EoS is a critical and highly uncertain microphysical input in models of core-collapse supernovae [179]. Figure 2 in Ref. [180] shows the mass-radius relation for typical EoSs as black curves. Depending on the EoS the mass-radius relation can strongly vary. Moreover, some combinations of neutron star mass and radius are excluded by causality, finite pressure constraints, and general relativity (see upper left corner in Fig. 2 in Ref. [180]). We vary the neutron star mass and radius between $0.8 \leq M_{\mathrm{ns}}/M_{\odot} \leq 2.0$ and $7.0 \leq R_{\mathrm{ns}}/\mathrm{km} \leq 30.0$, respectively, for the calculation of the steady-state trajectories. With this variation, we cover possible neutron star masses and radii predicted by different EoS, take into account the large uncertainties in the EoS, and consider that the neutron star shrinks when it cools down (see Fig. 13 of Ref. [181] and Figs. 1-2 of Ref. [182]). For comparison, Ref. [102] modified the neutron star mass between $M_{\mathrm{ns}} = 1.2-2.0\ M_{\odot}$ and kept the neutron star radius constant at $R_{\mathrm{ns}} = 10.0$ km, and Ref. [103] varied the neutron star mass and radius between $M_{\mathrm{ns}} = 1.4-2.0\ M_{\odot}$ and $R_{\mathrm{ns}} = 10.0-20.3$ km, respectively.

The energies and luminosities of the neutrinos and antineutrinos determine the electron fraction. In charge equilibrium the electron fraction is equal to the proton to nucleon ratio

$$Y_{\mathrm{e}} = \frac{Y_{\mathrm{p}}}{Y_{\mathrm{p}} + Y_{\mathrm{n}}} = \frac{1}{1 + \frac{Y_{\mathrm{n}}}{Y_{\mathrm{p}}}}. \tag{4.1}$$

The variation of the proton and neutron abundances with time are given by

$$\dot{Y}_{\mathrm{p}} = -\lambda_{\bar{\nu}_{\mathrm{e}}} Y_{\mathrm{p}} + \lambda_{\nu_{\mathrm{e}}} Y_{\mathrm{n}}, \tag{4.2}$$

$$\dot{Y}_{\mathrm{n}} = +\lambda_{\bar{\nu}_{\mathrm{e}}} Y_{\mathrm{p}} - \lambda_{\nu_{\mathrm{e}}} Y_{\mathrm{n}}. \tag{4.3}$$

In case of a weak equilibrium, i.e., an equilibrium of neutron and proton production due to these weak interaction reactions, we have $\dot{Y}_{\mathrm{p}} = \dot{Y}_{\mathrm{n}} = 0$. This leads to

$$\frac{Y_{\mathrm{n}}}{Y_{\mathrm{p}}} = \frac{\lambda_{\bar{\nu}_{\mathrm{e}}}}{\lambda_{\nu_{\mathrm{e}}}} \tag{4.4}$$

and we can rewrite Eq. (4.1) as

$$Y_{\mathrm{e}} = \frac{1}{1 + \frac{\lambda_{\bar{\nu}_{\mathrm{e}}}}{\lambda_{\nu_{\mathrm{e}}}}}. \tag{4.5}$$

The (anti)neutrino capture rates are given by [113, 125]

$$\lambda_{\nu_{\mathrm{e}}} \simeq \frac{L_{\nu_{\mathrm{e}}}}{4\pi r^2 \langle E_{\nu_{\mathrm{e}}} \rangle} \langle \sigma_{\nu_{\mathrm{e}}} \rangle, \tag{4.6}$$

$$\lambda_{\bar{\nu}_{\mathrm{e}}} \simeq \frac{L_{\bar{\nu}_{\mathrm{e}}}}{4\pi r^2 \langle E_{\bar{\nu}_{\mathrm{e}}} \rangle} \langle \sigma_{\bar{\nu}_{\mathrm{e}}} \rangle, \tag{4.7}$$

where $\langle \sigma_{\nu_{\mathrm{e}}} \rangle$ and $\langle \sigma_{\bar{\nu}_{\mathrm{e}}} \rangle$ are the cross sections of the neutrinos and antineutrinos, respectively, and r is the distance from the neutron star. Inserting Eqs. (4.6)–(4.7) into Eq. (4.5) leads to

$$Y_{\mathrm{e}} = \frac{1}{1 + \frac{\langle \sigma_{\bar{\nu}_{\mathrm{e}}} \rangle}{\langle \sigma_{\nu_{\mathrm{e}}} \rangle} \cdot \frac{L_{\bar{\nu}_{\mathrm{e}}}}{L_{\nu_{\mathrm{e}}}} \cdot \frac{\langle E_{\nu_{\mathrm{e}}} \rangle}{\langle E_{\bar{\nu}_{\mathrm{e}}} \rangle}}. \tag{4.8}$$

The (anti) neutrino cross section depends on the (anti)neutrino temperature, and thus on the (anti)neutrino energy $\langle E_{\nu_{\mathrm{e}}, \bar{\nu}_{\mathrm{e}}} \rangle$. Consequently, the electron fraction and the (anti)neutrino luminosity and energy are not independent. For a systematic study of the steady-state trajectories, we keep the energy and luminosity of the electron neutrinos constant, i.e., $\langle E_{\nu_{\mathrm{e}}} \rangle = 16.66$ MeV and $L_{\nu_{\mathrm{e}}} = 2 \cdot 10^{51}$ ergs/s, and adapt the corresponding $\langle E_{\bar{\nu}_{\mathrm{e}}} \rangle$ and $L_{\bar{\nu}_{\mathrm{e}}}$ to cover typical electron fractions in neutron-rich winds between $0.40 \leq Y_{\mathrm{e}} \leq 0.49$ (Refs. [102] and [103] considered electron fractions between $Y_{\mathrm{e}} = 0.43-0.46$ and $Y_{\mathrm{e}} = 0.45-0.495$, respectively). If we assume equal (anti)neutrino number luminosities, i.e., $L_{\nu_{\mathrm{e}}}/\langle E_{\nu_{\mathrm{e}}} \rangle = L_{\bar{\nu}_{\mathrm{e}}}/\langle E_{\bar{\nu}_{\mathrm{e}}} \rangle$, $\langle E_{\bar{\nu}_{\mathrm{e}}} \rangle$ is determined through Eq. (4.8), and thus $L_{\bar{\nu}_{\mathrm{e}}}$ is ultimately defined through the assumption of equal (anti)neutrino number luminosities. Hence, we can systematically change the steady state trajectories. Note that other choices for $\langle E_{\nu_e} \rangle$ and L_{ν_e} do not significantly change the evolution of the steady-state trajectories.

Figure 4.2 illustrates the temperature (left panel) and density (right panel) evolution of the steady-state trajectories calculated with a neutron star radius and mass of $R_{ns} = 30$ km, $M_{ns} = 0.8\ M_{\odot}$ indicated by red lines and $R_{ns} = 9$ km, $M_{ns} = 2.0\ M_{\odot}$ illustrated by blue lines, for $Y_e = 0.40-0.49$. For the same R_{ns} and M_{ns}, smaller electron fractions lead to lower temperatures and densities. There exist no other combinations of R_{ns} and M_{ns} in the considered parameter space which lead to higher or lower temperatures and densities. Note that some combinations of small R_{ns} and high M_{ns} are excluded by causality (see Fig. 2 in Ref. [180]). The general behavior is that smaller neutron star radii and higher neutron star masses lead to lower temperatures and densities. When we vary the neutron star radius and mass between $7 \leq R_{ns}/\text{km} \leq 30$ and $0.8 \leq M_{ns}/M_{\odot} \leq 2.0$, we obtain steady-state trajectories with temperature and density evolutions in the space between the red and blue band in Fig. 4.2. Therefore, we cover a wide range of entropies and expansion time scales which may occur in wind simulations. Note that different steady-state trajectories have different temperature (density) gradients. If a combination of R_{ns} and M_{ns} is not excluded by causality, we only obtain subsonic solutions of the wind equations (see blue line in Fig. 2.6). For even smaller R_{ns} or higher M_{ns}, if the combination is not excluded, $\dot{M} < \dot{M}_{crit}$ and we obtain breeze solutions (see green lines in Fig. 2.6) of the wind equations. On the contrary, for even larger R_{ns} and/or smaller M_{ns}, $\dot{M} > \dot{M}_{crit}$ and we get mathematical solutions without a physical meaning (see gray lines in Fig. 2.6).

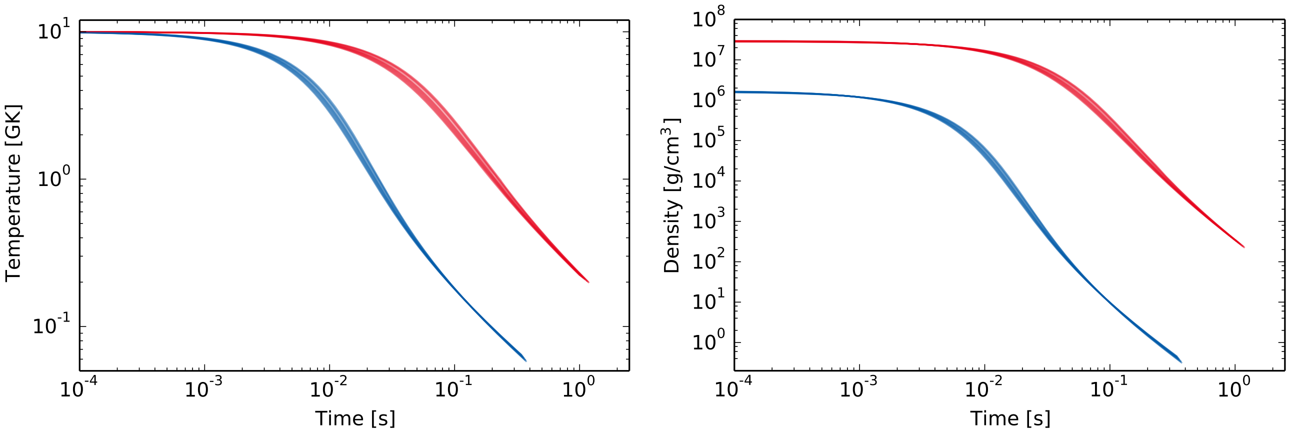

Figure 4.2: Overview of temperature (left panel) and density evolution (right panel) of the steady-state trajectories calculated with $R_{ns} = 30$ km, $M_{ns} = 0.8\ M_{\odot}$ (red lines) and $R_{ns} = 9.0$ km, $M_{ns} = 2.0\ M_{\odot}$ (blue lines) for $0.40 \leq Y_e \leq 0.49$. The spread of the blue and the red lines is due to the different electron fractions.

4.3.1 Impact of parameters in the steady-state model on wind entropy and expansion time scale

The impact of the different input parameters in the steady-state model, i.e., M_{ns}, R_{ns}, $L_{\bar{\nu}}$, on the wind entropy and expansion time scale are illustrated in Fig. 4.3 (for comparison, see also Refs. [102, 103]). In our reference case, the neutron star mass and radius are $M_{ns} = 1.4\ M_{\odot}$ and $R_{ns} = 10$ km, respectively, and the antineutrino luminosity is $L_{\bar{\nu}_e} = 2.82 \cdot 10^{51}$ ergs/s (i.e., $Y_e = 0.45$). We vary one of the three parameters and keep the other two constant. The figure shows that the entropy increases (left panel in first row) and the expansion time scale decreases (right panel in first row) as the neutron star mass increases. Moreover, larger neutron star radii lead to smaller entropies (left panel in second row) and longer expansion time scales (right panel in second row). A more compact proto-neutron star, i.e., more massive and/or smaller radius, ejects slightly less material due to the larger binding (M/R), and provides higher entropies but longer expansion time scales [101, 104]. This is in agreement with the relation between ejected mass $\dot{M}$, entropy S and expansion time scale τ and the neutron star mass and radius, $\dot{M} \propto R_{ns}^{5/3} M_{ns}^{-2}$, $S \propto R_{ns}^{-2/3} M_{ns}$ and $\tau \propto R_{ns}$, of Ref. [55] for a fixed neutrino energy and luminosity in the Newtonian limit. Note that in the Newtonian limit the expansion time scale increases as the mass increases, whereas if general relativity effects are considered, the expansion time scale decreases. The dependence of the entropy and the expansion time scale on the neutron star mass and radius is stronger if general relativity corrections are included (see Refs. [101–104]). The reason for this are the two prefactors on the right-hand side of Eqs. (28, 33, 35) in Ref. [102] which are enlarged by a stronger gravitational force M/r^2 with larger masses and/or shorter radii. Both, wind entropy (left panel in third row) and expansion time scale (right panel in third row) decrease when the antineutrino luminosity is increased. Larger neutrino luminosities cause a higher mass outflow rate $\dot{M}$ due to the more efficient neutrino heating [102]. As a consequence of the more efficient neutrino heating, both the baryon density and the fluid velocity increase. The increase of the baryon density leads to a decrease of the entropy ($S \propto T^3/\rho$), and the expansion time scale becomes shorter when the fluid velocity increases ($\tau = r/v|_{T=0.5\ \mathrm{MeV}}$).

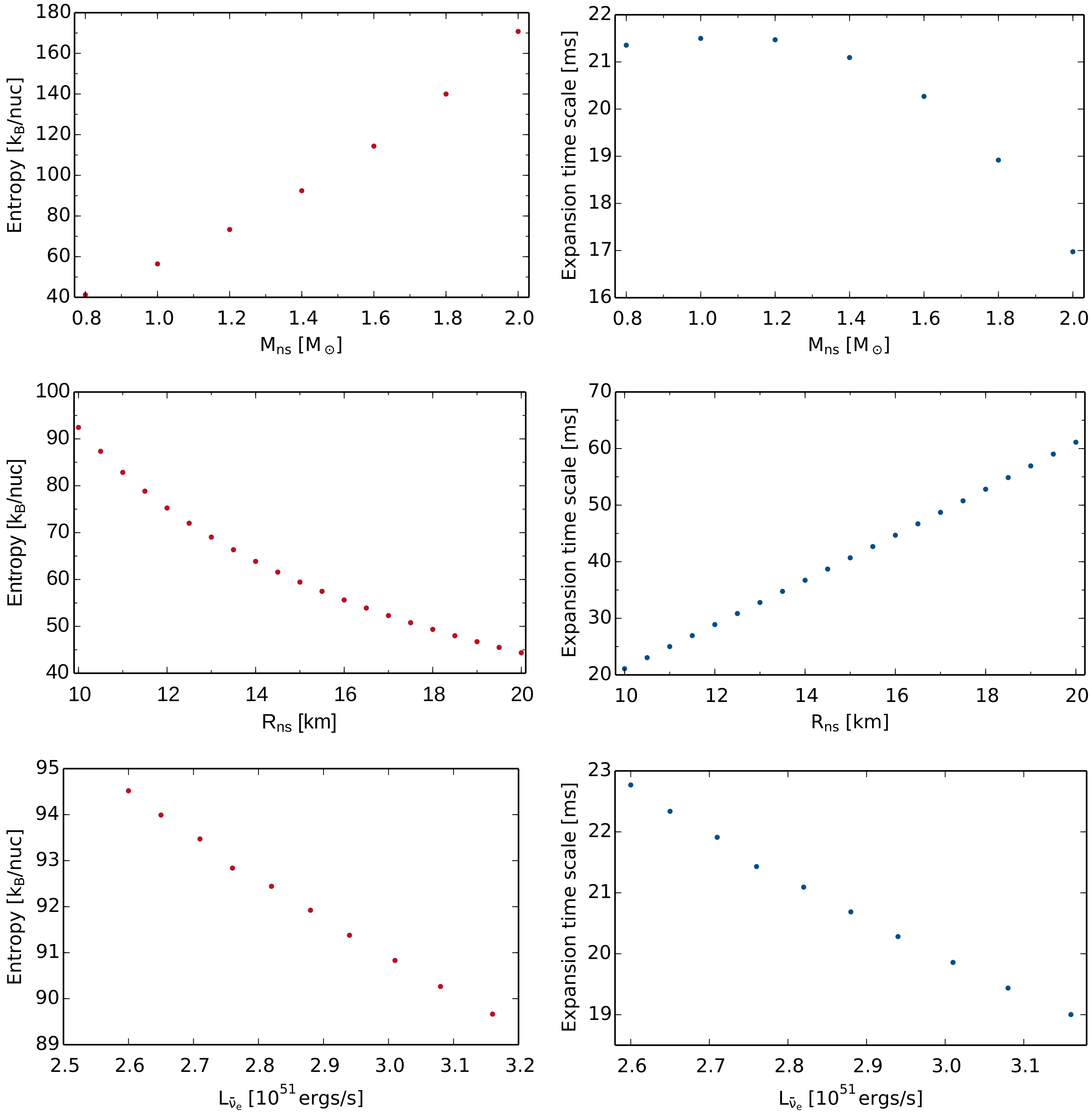

Figure 4.3: Impact of the mass (M_{ns}) and the radius (R_{ns}) of the neutron star, and the electron antineutrino luminosity ($L_{\bar{\nu}_e}$) on the entropy and expansion time scale. The electron antineutrino luminosities of $L_{\bar{\nu}_e}/(10^{51}$ ergs/s)= 3.16, 3.08, 3.01, 2.94, 2.88, 2.82, 2.76, 2.71, 2.65, and 2.60 correspond to the electron fractions Y_e =0.40, 0.41, 0.42, 0.43, 0.44, 0.45, 0.46, 0.47, 0.48, and 0.49.

4.3.2 Comparison of a trajectory from a hydrodynamic simulation with a steady-state trajectory

Figure 4.4 shows how well a trajectory from a hydrodynamic simulation can be represented by a steady-state trajectory. The hydrodynamic trajectory is from the explosion model M15l1r1 (see Ref. [36] for more details) and is ejected 9 s after bounce. The steady-state trajectory describes the trajectory from the simulation very well until the reverse shock occurs at $t \approx 0.24$ s. Several hydrodynamic simulations showed that the neutrino-driven wind expands through the early slow-expanding supernova ejecta [36, 37, 39, 135–137]. If the wind becomes supersonic, the collision of both leads to a reverse shock or wind termination. During the collision, kinetic energy is transformed into internal energy resulting in an increase of temperature and density, and thus raise the entropy and decrease the expansion time scale. If the wind becomes subsonic, the wind velocity naturally decreases [102, 104]. The interaction of the slow-moving supernova ejecta with the wind is not a steady-state phenomenon. In steady-state models the neutrino-driven wind expands freely. Consequently, hydrodynamic simulations are necessary to study the wind in a consistent way.

The radius of the reverse shock depends on the mass outflow and the velocity of the wind, and on the pressure of the slow-expanding supernova ejecta [36]. Besides, the pressure of the supernova ejecta is correlated with the explosion energy and the shock radius [36]. Moreover, convection and anisotropies have a strong impact on the pressure of the supernova ejecta, and thus influence the radius of the reverse shock [37].

However, the main impact of the reverse shock is an increase of temperature and density which can be calculated with the Rankine-Hugoniot conditions (see, e.g., Appendix B in Ref. [45]). The evolution of the density after the shock can be determined from the condition that the mass outflow rate ($\dot{M} = 4\pi r^2 v \rho$) is constant. Nonetheless, due to different possible velocity evolutions, the density is not clearly defined. References [183–185] investigated the impact of the reverse shock on the nucleosynthesis assuming that the r-process occurs in the wind. Moreover, Refs. [133, 134] found that the reverse shock can influence the nucleosynthesis in the νp-process. Due to the uncertainties in the analytical description of the reverse shock, our strategy is to extrapolate the steady-state trajectory, assuming an adiabatic expansion, i.e., constant entropy.

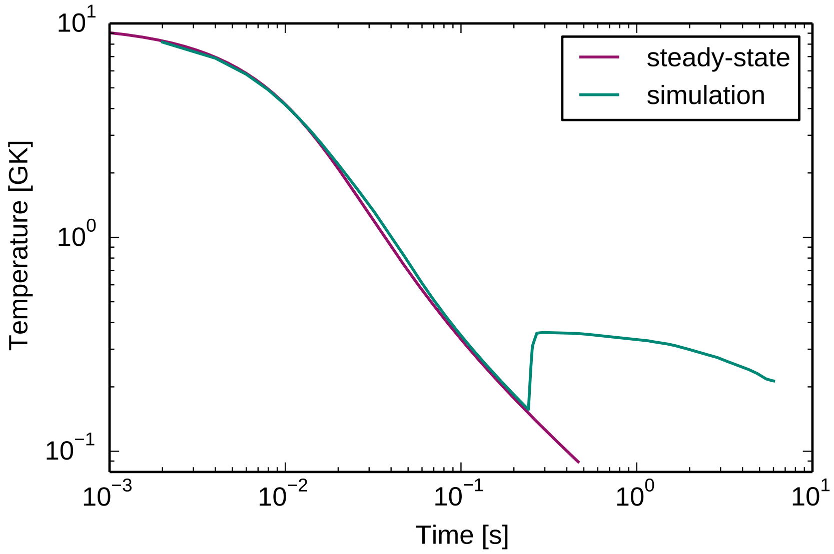

Figure 4.4: Comparison of a trajectory from a hydrodynamical simulation (green line) and a steady-state trajectory (purple line). The hydrodynamical trajectory is from the explosion model M15l1r1 [36] and is ejected 9 s after bounce.

4.4 Types of nucleosynthesis in neutron-rich winds

We have calculated the nucleosynthesis for 2696 steady-state trajectories. In the final abundances we distinguish between four different nucleosynthesis patterns. These four nucleosynthesis groups are identified by the Y_n/Y_{seed}[1] and the Y_α/Y_{seed} at $T \approx 3$ GK, following a similar strategy as in Ref. [40]. The different neutron, alpha, and seed

---

[1] Here, the seed abundance Y_{seed} is defined as the sum of the abundances of all nuclei heavier than helium.

abundances lead to different nucleosynthesis evolutions, and thus to different (final) abundance patterns. Furthermore, for each group, there are different threshold temperatures below which the subsequent nucleosynthesis evolution does not significantly change the abundance pattern. Two abundance patterns are mainly formed during NSE (we will call them NSE1 and NSE2), and the other two are influenced by charged particle reactions (we will refer to them as CPR1 and CPR2). Some steady-state trajectories lead to the formation of elements beyond the second r-process peak, but these cannot be produced in the wind at the current understanding. Therefore, we will not describe them in detail. Note that the nucleosynthesis evolution for steady-state trajectories assigned to the same nucleosynthesis pattern are not identical for each trajectory but the trends are similar. The conditions investigated here are also reached even if the neutrino-driven wind does not form and matter is subsonically ejected while exposed to neutrinos. In the following, we will describe the four different nucleosynthesis groups.

4.4.1 NSE1

At $T = 3$ GK, for $Y_{\mathrm{n}}/Y_{\mathrm{seed}}$ and $Y_{\alpha}/Y_{\mathrm{seed}}$ smaller than 10^{-2} and 10^{-1}, respectively, we find the abundance pattern NSE1. 178 steady-state trajectories lead to this abundance pattern. The initial entropies of these steady-state trajectories are rather low ($15\ k_{\mathrm{B}}/\mathrm{nuc} \lesssim S \lesssim 40\ k_{\mathrm{B}}/\mathrm{nuc}$), and the expansion time scales are rather long ($80\ \mathrm{ms} \lesssim \tau \lesssim 230\ \mathrm{ms}$). We find this abundance pattern for $Y_{\mathrm{e}} = 0.40 - 0.44$. In NSE1, the initial nucleosynthesis evolution is characterized by the sequence of three-body reactions $\alpha(\alpha n,\gamma)^{9}\mathrm{Be}$ and $^{9}\mathrm{Be}(\alpha,\gamma)$, which bypass the 3-$\alpha$ reaction bottleneck [28]. This group is similar to the one identified by Ref. [40] as NSE. Following the nucleosynthesis evolution, around $T = 6$ GK, matter has moved up to the Ca-Zn region, and the nucleosynthesis path evolves close to stability on the neutron-rich side due to the small $Y_{\mathrm{n}}/Y_{\mathrm{seed}}$. When the temperature drops down to $T \approx 5$ GK matter has reached $Z \sim 40$ and the most abundant elements are Fe and Ni (left panel in Fig. 4.5). Between $T \approx 5 - 4$ GK, there is only a redistribution of matter by few charged particle reactions. The nucleosynthesis path cannot overcome the neutron shell closure $N = 50$ because of the small amount of free neutrons and alpha particles, and thus matter accumulates there. Consequently, the major abundance peaks are already formed around $T \approx 5$ GK at the end of NSE, and the subsequent evolution does not significantly change the abundance pattern (middle and right panel in Fig. 4.9, see also Ref. [40]). Note the gap in the abundances between $Z = 3 - 19$ due to the small alpha abundance. The low entropies and the long expansion time scales prevent the existence of larger amounts of free nucleons and alpha particles. At $T \approx 3.5$ GK almost no free neutrons and alpha particles are available. During the decay, the abundance pattern slightly changes. Since the major abundance peaks are already formed at the end of NSE, the abundances are mainly determined by binding energies and partition functions, and are less dependent on specific reactions. For stable nuclei and particularly for unstable nuclei, binding energies and partition functions are better known than reaction rates [150]. Figure 4.6 illustrates the final abundance pattern that exhibits characteristic Ni (not for all trajectories), Zn, and Kr peaks. Elements heavier than $Z \approx 38$ are not synthesized.

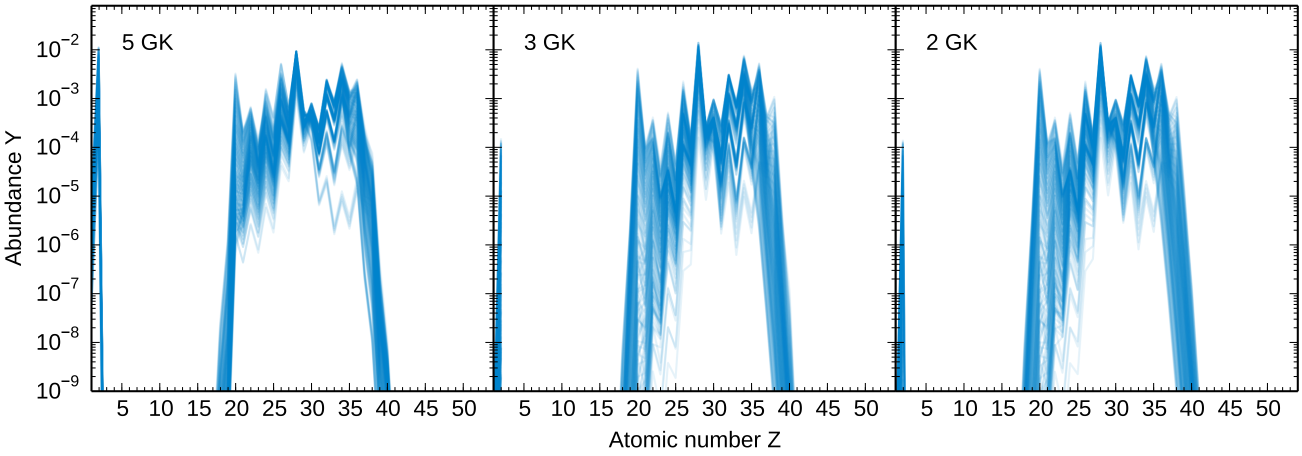

Figure 4.5: Abundance pattern NSE1 at $T = 5$ GK, 3 GK, and 2 GK. The electron fractions, the entropies, and the expansion time scales of the steady-state trajectories vary between: $0.40 \leq Y_{\mathrm{e}} \leq 0.44$, $15\ k_{\mathrm{B}}/\mathrm{nuc} \lesssim S \lesssim 40\ k_{\mathrm{B}}/\mathrm{nuc}$, and $80\ \mathrm{ms} \lesssim \tau \lesssim 230\ \mathrm{ms}$.

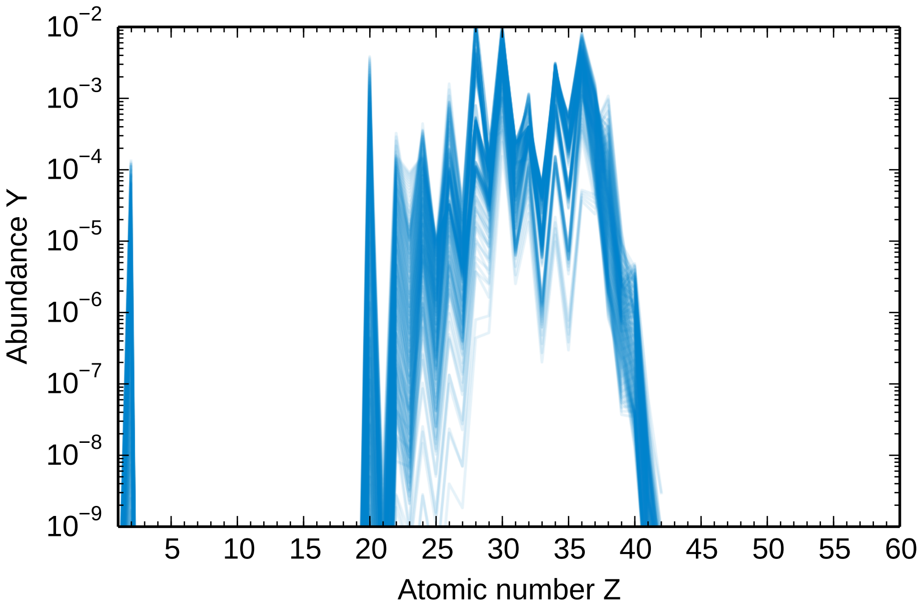

Figure 4.6: Abundance pattern NSE1 after final decay.

4.4.2 NSE2

We find the abundance pattern NSE2 for $Y_n/Y_{\mathrm{seed}} < 10^{-8}$ and $Y_\alpha/Y_{\mathrm{seed}} > 10^{-2}$ at $T = 3$ GK. This criterion is fulfilled by 436 steady-state trajectories. The entropies, the expansion time scales, and the electron fractions of these steady-state trajectories range between $S \approx 15-85\ k_B/\mathrm{nuc}$, $\tau \approx 50-230$ ms, and $Y_e = 0.46-0.49$. In comparison to the nucleosynthesis group NSE1, the upper entropy limit is larger and the lower expansion time scale limit is smaller. Figure 4.7 shows the abundance pattern at $T = 5, 3$, and 2 GK. At $T \approx 5$ GK (left panel in Fig. 4.7) most of the matter is accumulated between $Z = 22-28$. The most abundant elements are Fe and Ni. Only a few free neutrons are left, and thus the nucleosynthesis path moves away from the valley of stability by (p,γ) and (p,n) reactions and evolves on the proton-rich side ($Z = N$). Around $T \approx 4$ GK, matter is shifted from Fe to Ni by (p,γ) and (p,n) reactions but the inverse reactions also occur. For temperatures between $T \approx 4-3$ GK, the nucleosynthesis path reaches Zn, and for some steady-state trajectories even goes beyond (middle panel in Fig. 4.7). Around $T \approx 3.3$ GK, (α,p) reactions also occur but they do not significantly contribute to the nucleosynthesis evolution.

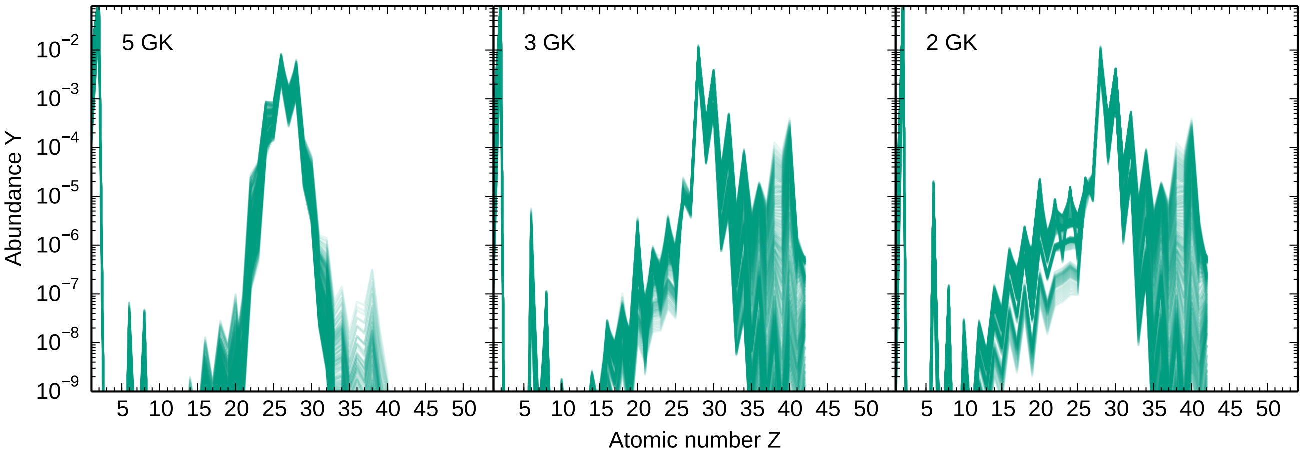

Figure 4.7: Abundance pattern NSE2 at $T = 5$ GK, 3 GK, and 2 GK. The electron fractions, the entropies, and the expansion time scales of the steady-state trajectories range between $0.46 \leq Y_e \leq 0.49$, $15\ k_B/\mathrm{nuc} \lesssim S \lesssim 85\ k_B/\mathrm{nuc}$, and $50\ \mathrm{ms} \lesssim \tau \lesssim 230$ ms.

Nickel and zinc act as bottlenecks in the nucleosynthesis evolution, and thus are the most abundant elements. When the temperature drops down to 2 GK (right panel in Fig. 4.7), there is only a redistribution of matter, and the abundances for $6 \leq Z \leq 27$ increase due to the starting decay from the proton-rich side of stability. The final abundances after decay are illustrated in Fig. 4.8. The final NSE2 pattern exhibits a characteristic abundance peak at $Z = 28$ and for some trajectories also at $Z = 26$ and/or $Z = 30$. Elements heavier than zinc are only formed for $Y_n/Y_{seed} > 10^{-9}$. Although the entropies and the expansion time scales of the steady-state trajectories investigated here are slightly larger and slightly shorter, respectively, compared to the ones of the trajectories assigned to the group NSE1, heavier elements are not synthesized. Hence, the impact of the electron fraction on the nucleosynthesis is more crucial.

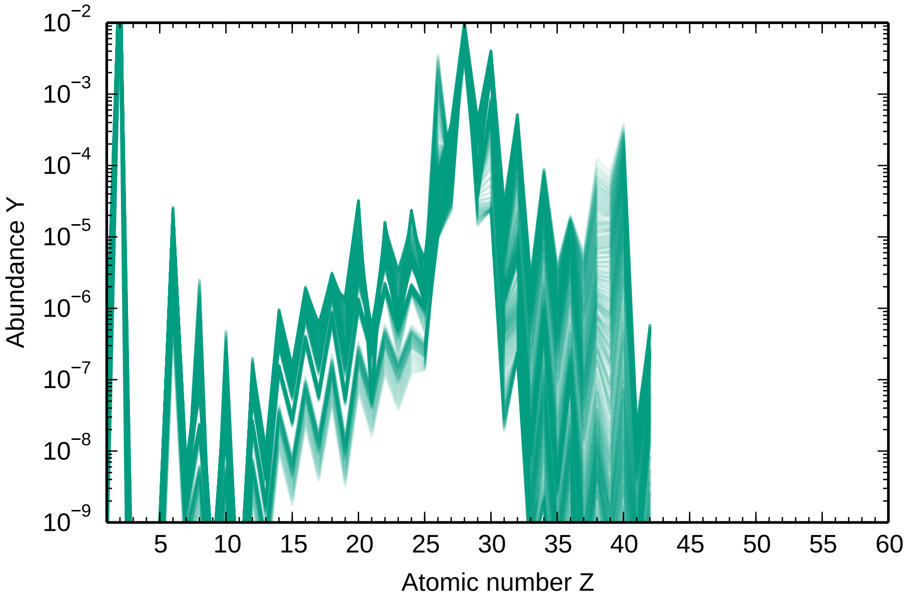

Figure 4.8: Abundance pattern NSE2 after final decay.

4.4.3 CPR1

The conditions leading to the abundance pattern CPR1 are: $10^{-8} \lesssim Y_n/Y_{seed} < 1.5 \cdot 10^{-5}$ and $Y_\alpha/Y_{seed} > 10^{-2}$ at $T = 3$ GK. The entropies and the expansion time scales of the steady-state trajectories (a total of 1022 steady-state trajectories are assigned to the nucleosynthesis group CPR1) span between $15\ k_B/\text{nuc} \lesssim S \lesssim 135\ k_B/\text{nuc}$ and $35\ \text{ms} \lesssim \tau \lesssim 230\ \text{ms}$, respectively. The electron fractions range between $0.40 \leq Y_e \leq 0.49$. When the temperature drops down to $T \approx 6$ GK, the nucleosynthesis path evolves by (α, n) and (p, n) reactions on the neutron-rich side of stability and has already reached the Ca-Zn region. At $T \approx 5$ GK, matter has reached nuclei around $Z = 39$ (left panel in Fig. 4.9). Most abundant are Fe, Ni, and nuclei at $N = 50$. Some (α, n) and (p, n) are frozen out. When the temperature decreases to $T \approx 4$ GK, matter is redistributed by (p, n) and (p, γ) reactions. Most abundant are Fe, Co, Ni, Cu, Zn, and nuclei at $N = 50$. At $T = 3$ GK more matter has accumulated at $N = 50$ but the nucleosynthesis path does not go beyond (middle panel in Fig. 4.9). Even if the neutron abundance is larger compared to the nucleosynthesis groups NSE1 and NSE2, resulting in a nucleosynthesis path further away from the valley of stability on the neutron-rich side, the alpha abundance is not large enough to overcome the negative Q-values of (α, n) reactions for nuclei close to stability at $N = 50$ (see Fig 4.10). For lower temperatures, there is only a redistribution of matter (right panel in Fig. 4.9) and decay to stability. The abundances for $Z = 6 - 20$ are a result of alpha capture reactions due to the larger alpha abundance. The final abundance distribution of the nucleosynthesis group CPR1 is presented in Fig. 4.11. The overall abundance pattern has distinctive peaks at Ni, Zn, and Sr. For some steady-state trajectories, there is also an abundance peak at Kr. Heavier elements than Zr are not formed due to the small Y_α/Y_{seed} and the negative Q-values of some (α, n) reactions at $N = 50$. Thus, the final abundance are mainly determined by the Q-values of (α, n) reactions at $N = 50$ (see also Refs. [33, 40, 186]). The nucleosynthesis group CPR1 describes the transition from the groups NSE1 or NSE2 to the group CPR2.

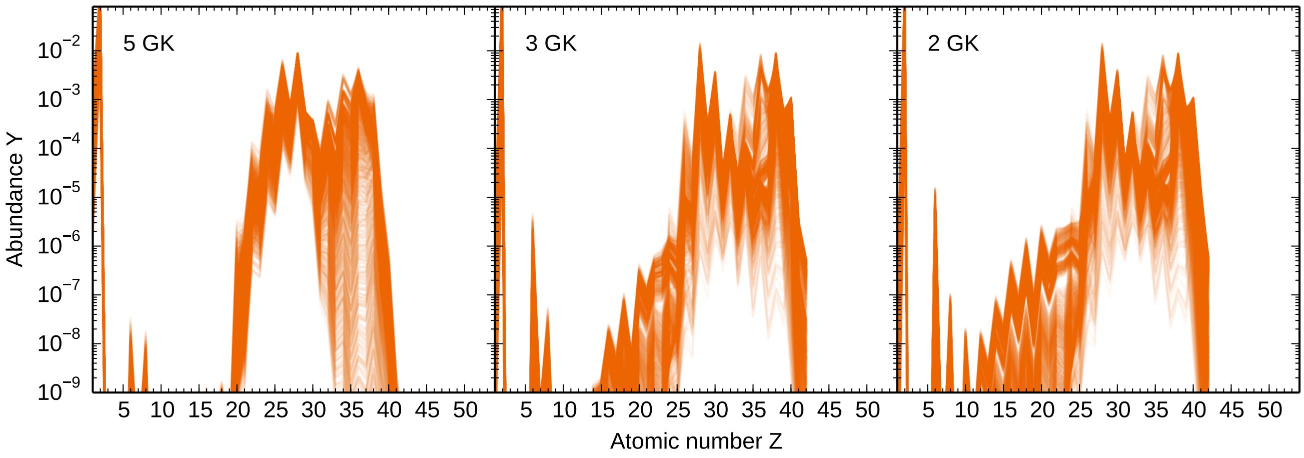

Figure 4.9: Abundance pattern CPR1 at $T = 5$ GK, 3 GK, and 2 GK. The electron fractions, the entropies, and the expansion time scales of the steady-state trajectories are: $0.40 \leq Y_e \leq 0.49$, $15\ k_B/\text{nuc} \lesssim S \lesssim 135\ k_B/\text{nuc}$, and $35\ \text{ms} \lesssim \tau \lesssim 230\ \text{ms}$.

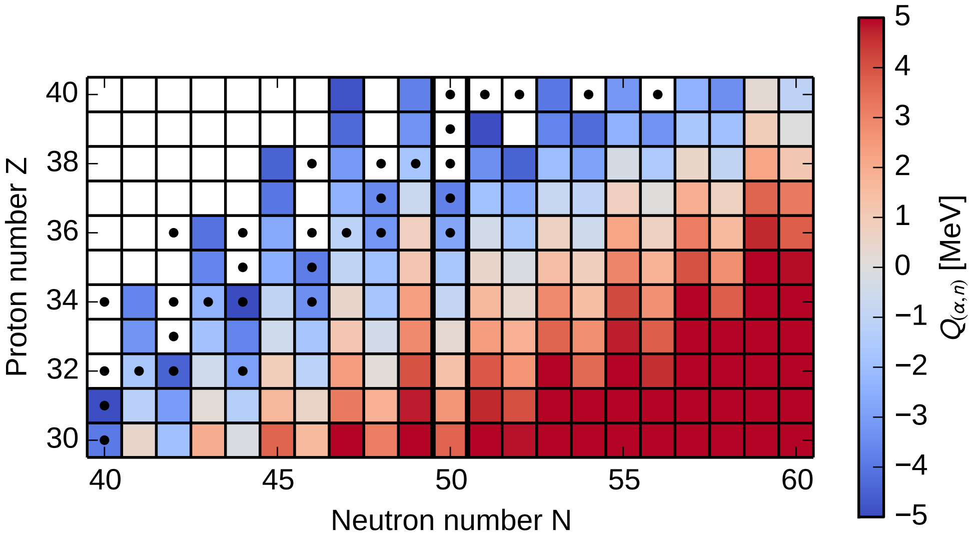

Figure 4.10: Q-value of (α, n) reactions. The black dots denote stable nuclei and the black box indicates the neutron magic number $N = 50$. Q-values smaller than -5 MeV are shown in white.

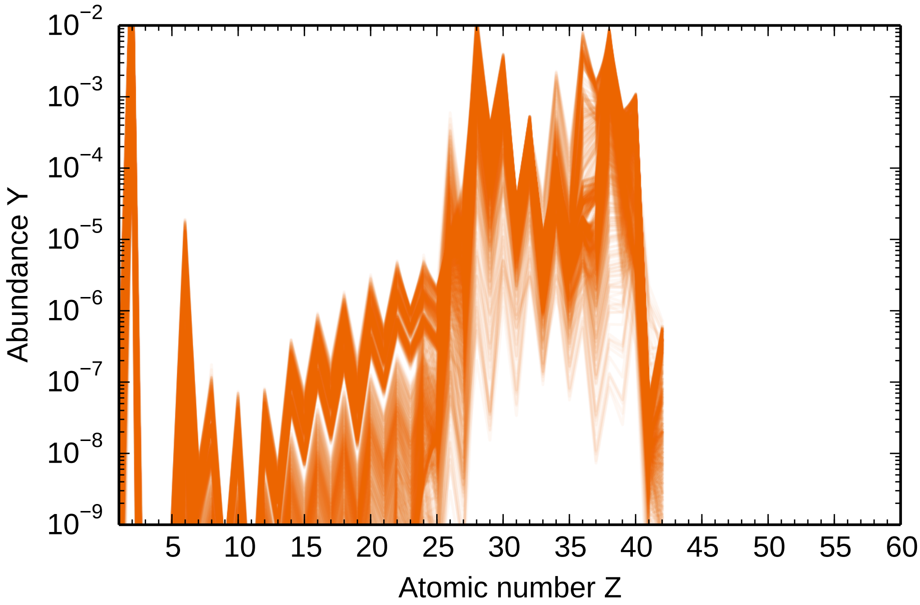

Figure 4.11: Abundance pattern CPR1 after final decay.

4.4.4 CPR2

We find the nucleosynthesis group CPR2 for $1.5 \cdot 10^{-5} \lesssim Y_{\mathrm{n}}/Y_{\mathrm{seed}} \lesssim 20$ and $Y_\alpha/Y_{\mathrm{seed}} \gtrsim 10^{-2}$. The electron fractions, the entropies, and the expansion time scales of the 1060 steady-state trajectories vary between: $Y_{\mathrm{e}} \approx 0.40 - 0.49$, $S \approx 30 - 220$ k_{B}/nuc, and $\tau \approx 25 - 230$ ms. Note that compared to the other nucleosynthesis groups described in Sects. 4.4.1–4.4.3 the lower limit of the entropy is higher. Following the nucleosynthesis evolution of the group CPR2, around $T \approx 6$ GK the nucleosynthesis path proceeds close to stability by alpha capture reactions and especially (α, n) reactions. Most of the matter is accumulated between $Z \approx 20 - 30$. When the temperature decreases to $T \approx 5$ GK, the path has reached Kr and moves away from the valley of stability (left panel in Fig. 4.12). The most abundant nuclei are at the neutron shell closure $N = 50$ or close to. At $T \approx 4$ GK, there are no free protons left. Between $T \approx 4 - 3$ GK, the alpha and the neutron abundance are large enough to overcome the negative Q-value of (α, n) reactions for nuclei close to stability at $N = 50$, and the nucleosynthesis path reaches Mo. The most abundant elements are Kr, Rb, and Sr (see middle panel in Fig. 4.12). However, the abundance pattern

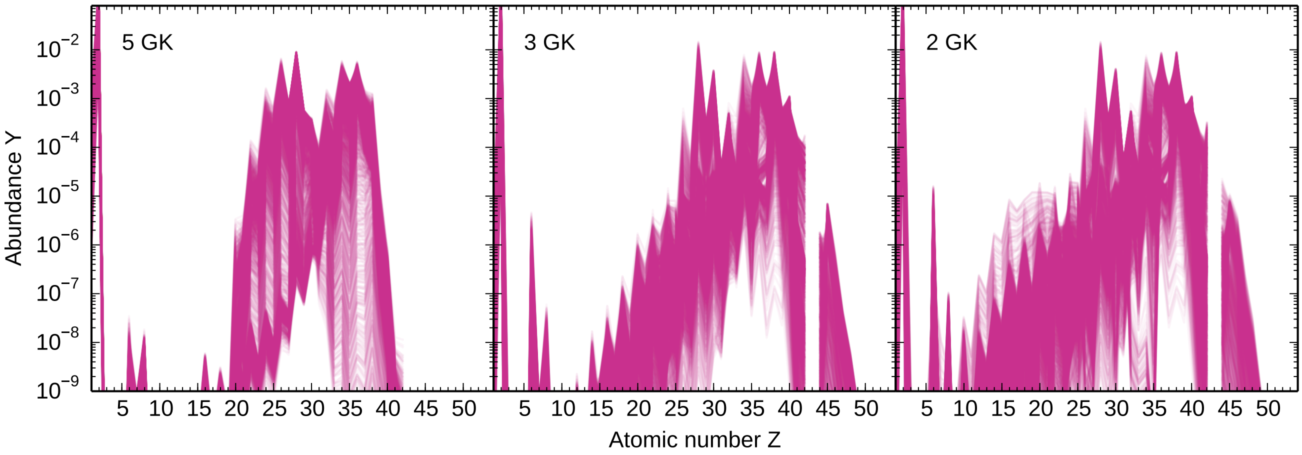

Figure 4.12: Abundance pattern CPR2 at different temperatures, i.e., $T = 5$ GK, 3 GK, and 2 GK. The electron fraction, the entropy, and the expansion timescale range between $Y_{\mathrm{e}} \approx 0.40 - 0.49$, $S \approx 30 - 220$ k_{B}/nuc, and $\tau \approx 25 - 230$ ms.

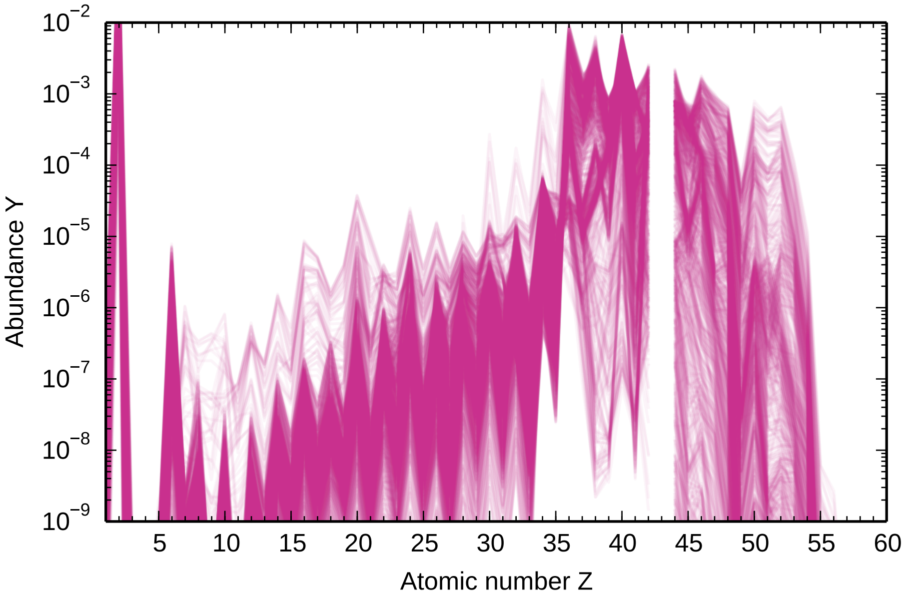

Figure 4.13: Abundance pattern CPR2 after final decay.

varies for different steady-state trajectories (i.e., different $Y_\mathrm{n}/Y_\mathrm{seed}$ and Y_α/Y_seed). Remarkable are the substantial changes in the overall abundance pattern when the temperature decreases from 5 GK to 3 GK. Consequently, nuclear physics uncertainties can influence the nucleosynthesis evolution, and the abundances are not determined by binding energies or Q-values. We will focus on the impact of nuclear physics uncertainties on the abundances in Chapter 5. At $T = 2$ GK, the most abundant elements do not change (right panel in Fig. 4.12) and the abundances are redistributed within isotopic chains. The final abundances after decay are shown in Fig. 4.13. The overall abundance pattern exhibits peaks at Kr (differently pronounced for different steady-state trajectories) and Zr. We find different patterns for Rb, Sr, and Y. This can be relevant when comparing the abundances of Sr and Y with the observations of old stars (see Sect. 4.2). In comparison to the other nucleosynthesis groups, heavier elements are synthesized during the decay (see Figs. 4.6, 4.8, 4.11). In addition, the heaviest elements vary for different steady-state trajectories, and thus depend on Y_α/Y_seed and $Y_\mathrm{n}/Y_\mathrm{seed}$.

4.4.5 Comparison between different nucleosynthesis types

In Sects. 4.4.1–4.4.4 we have shown that the abundance patterns are sensitive to $Y_\mathrm{n}/Y_\mathrm{seed}$ and Y_α/Y_seed. Besides, $Y_\mathrm{n}/Y_\mathrm{seed}$ and Y_α/Y_seed depend on electron fraction, entropy, and expansion time scale (see Sect. 2.5). According to Eq. (20b) in Ref. [111], electron fraction, entropy, and expansion time scale are related by

$$S \propto Y_\mathrm{e} \left(\frac{\tau}{\mathrm{s}}\right)^{1/3}, \tag{4.9}$$

for $Y_\mathrm{e} > 0.38$. This means that the same neutron-to-seed ratio can be achieved for the same initial electron fraction and several combinations of entropy and expansion time scale if the ratio S^3/τ is the same. Figure 4.14 illustrates the four different types of nucleosynthesis (indicated by the same colors as in Sects. 4.4.1–4.4.4) in the $S^3/\tau - Y_\mathrm{e}$ plane. Each dot represents one steady-state trajectory. The nucleosynthesis patterns are basically separated, there is only some overlap at the transitions between two groups. The reason for this is that the classification of each abundance pattern into one nucleosynthesis group based on $Y_\mathrm{n}/Y_\mathrm{seed}$ and Y_α/Y_seed does not exactly work for all steady-state trajectories. As Y_e increases from 0.40 to 0.44, the nucleosynthesis group NSE1 (CPR1) is spread over a shorter (longer) S^3/τ range. Besides, the transition from the nucleosynthesis group NSE1 to CPR1 becomes sharper as Y_e decreases from 0.44 to 0.40. In general, the lower the electron fraction, the larger is the S^3/τ range where CPR2 occurs. For $Y_\mathrm{e} = 0.45$, we only find the nucleosynthesis groups CPR1 and CPR2. As Y_e increases from 0.46 to 0.49, the nucleosynthesis group NSE2 (CPR2) spreads over a longer (shorter) S^3/τ range. Therefore, the larger the electron fraction, the higher entropies and/or expansion time scales are required to obtain an abundance pattern assigned to the nucleosynthesis group CPR2.

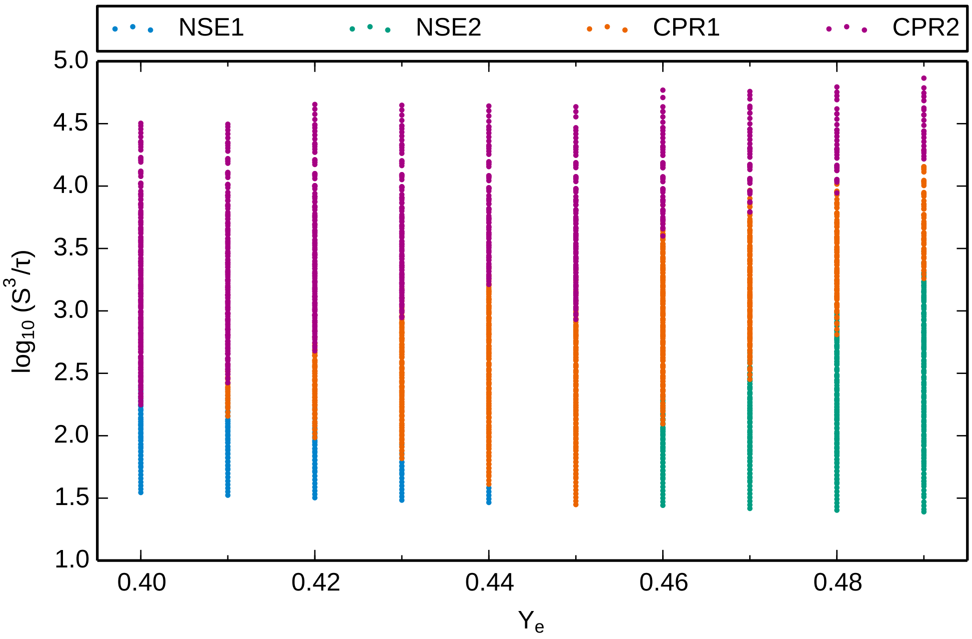

Figure 4.14: Different nucleosynthesis groups in the $S^3/\tau - Y_e$ plane. We apply the same color code to distinguish between the different groups as in Sects. 4.4.1–4.4.4.

If the electron fraction, entropy, and expansion time scale in the hydrodynamic simulation are known, Fig. 4.14 combined with the results discussed in Sects. 4.4.1–4.4.4 can roughly predict the nucleosynthesis evolution and the final abundance pattern without running post-processing nucleosynthesis calculations. This can be very useful when large amounts of trajectories have to be post-processed to get an overview about the synthesized elements. Note that the conditions investigated here are similar to those of supernova ejecta exposed to neutrinos and are reached even if the neutrino-driven wind does not form.

Figure 4.15 illustrates the different nucleosynthesis patterns we have described in Sect. 4.4 in the $Y_\alpha/Y_{\text{seed}} - Y_\text{n}/Y_{\text{seed}}$ plane. Note that post-processing calculations are required to identify the different nucleosynthesis groups based on the Y_α/Y_{seed} and $Y_\text{n}/Y_{\text{seed}}$. We apply again the same color code as in Sect. 4.4. Furthermore, we include Y_α/Y_{seed} and $Y_\text{n}/Y_{\text{seed}}$ which lead to the formation of elements beyond the second r-process peak. We also consider nucleosynthesis patterns for electron fractions between $0.25 \leq Y_e \leq 0.39$. Each chain represents a constant electron fraction in Fig. 4.15. For the calculation of the additional steady-state trajectories with $Y_e = 0.25 - 0.39$, we also vary the neutron star mass and radius between $0.8 \leq M/M_\odot \leq 2.0$ and $7 \leq R_{\text{ns}}/\text{km} \leq 30$, respectively. The black solid and dashed lines mark the constraints of the neutron star masses and radii used in the steady-state model on Y_α/Y_{seed} and $Y_\text{n}/Y_{\text{seed}}$. The dashed line corresponds to $M_{\text{ns}} = 0.8\ M_\odot$ and $R_{\text{ns}} = 30$ km, and the solid one to $M_{\text{ns}} = 2.0\ M_\odot$ and $R_{\text{ns}} = 9$ km. As we have already mentioned in Sect. 4.3, even smaller M_{ns} and larger R_{ns} lead to mathematical solutions of the wind equations without a physical meaning. Thus, we cannot access the lower left site of the $Y_\alpha/Y_{\text{seed}} - Y_\text{n}/Y_{\text{seed}}$ plane. On the contrary, for even larger masses and smaller radii we obtain breeze solutions. For breeze solutions the velocity does not attain the critical sound speed. However, most of the combinations of higher masses and smaller radii are excluded by causality (see Fig. 2 in Ref. [180]). Therefore, the upper right site of the $Y_\alpha/Y_{\text{seed}} - Y_\text{n}/Y_{\text{seed}}$ plane is also not attainable. The dots on the right-hand site of the solid black line are related to trajectories where the temperature and density evolutions initially drop fast, resulting in a large Y_α/Y_{seed} and $Y_\text{n}/Y_{\text{seed}}$ at $T = 3$ GK which are not representative for the nucleosynthesis of these trajectories. The upper left (lower right) side of the $Y_\alpha/Y_{\text{seed}} - Y_\text{n}/Y_{\text{seed}}$ plane can be reached by decreasing (increasing) the electron fraction.

For $R_{\max}$ and $M_{\min}$, Y_α/Y_{seed} decreases and $Y_\text{n}/Y_{\text{seed}}$ increases as Y_e decreases. We find the same behavior for $R_{\min}$ and $M_{\max}$ but it is weakly pronounced. Remarkable is the distribution of Y_α/Y_{seed} and $Y_\text{n}/Y_{\text{seed}}$ due to the different electron fractions. This indicates that rather Y_e than entropy and expansion time scale influences the neutron-to-seed ratio. For $Y_e = 0.46 - 0.49$ and low $Y_\text{n}/Y_{\text{seed}}$ and Y_α/Y_{seed}, the nucleosynthesis mainly proceeds by proton capture reactions along the valley of stability and on the proton-rich side (NSE2). The nucleosynthesis ends around $Z \sim 26 - 30$ when no further nuclei can be synthesized by proton captures. The NSE2 abundance pattern evolves

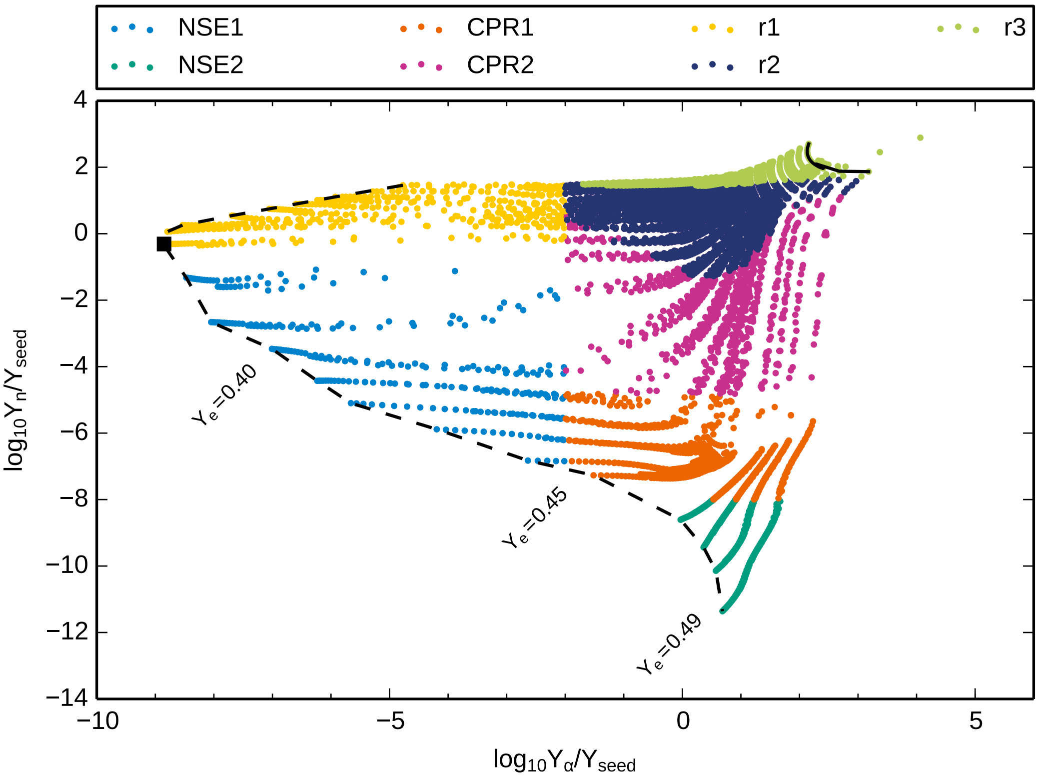

Figure 4.15: Different nucleosynthesis patterns in the $Y_\alpha/Y_{\rm seed} - Y_{\rm n}/Y_{\rm seed}$ plane. The colors describing the different nucleosynthesis groups are the same as in Sects. 4.4.1–4.4.4. The black solid and dashed lines mark the constraints of the neutron star masses and radii used in the steady-state model on $Y_\alpha/Y_{\rm seed}$ and $Y_{\rm n}/Y_{\rm seed}$. The dashed (solid) line corresponds to $M_{\rm ns} = 0.8\ M_\odot$ ($M_{\rm ns} = 2.0\ M_\odot$) and $R_{\rm ns} = 30$ km ($R_{\rm ns} = 9$ km). Each chain represents a constant $Y_{\rm e}$. The black square marks the deviation of the dashed black line for $Y_{\rm e} < 0.38$.

to pattern CPR1 when neutrons and alphas become more abundant at the expense of the proton abundance. For larger $Y_{\rm e}$ the transition from NSE2 to CPR1 occurs at larger $Y_\alpha/Y_{\rm seed}$ and $Y_{\rm n}/Y_{\rm seed}$. Due to the larger amount of free neutrons and protons (CPR1) matter moves away from the valley of stability on the neutron-rich side and heavier nuclei up to $Z \sim 40$ are formed (see Fig. 4.11). For further increasing $Y_{\rm n}/Y_{\rm seed}$ and slightly increasing $Y_\alpha/Y_{\rm seed}$, the nucleosynthesis path overcomes the neutron shell closure $N = 50$ and elements up to $Z \sim 54$ are synthesized (CPR2). The abundances assigned to group CPR2 are very sensitive to $Y_\alpha/Y_{\rm seed}$ and $Y_{\rm n}/Y_{\rm seed}$ and slight variations of these quantities lead to different abundance patterns (see Fig. 4.13). Indeed, not only the heaviest element changes but also the abundances of elements with lower atomic numbers are different. Figure 4.15 indicates that once a sufficient amount of $Y_\alpha/Y_{\rm seed}$ exists the nucleosynthesis evolution only depends on $Y_{\rm n}/Y_{\rm seed}$. Note that the same $Y_\alpha/Y_{\rm seed}$ and $Y_{\rm n}/Y_{\rm seed}$ do not necessarily lead to the same abundance pattern. The reason for this is that $Y_{\rm n}/Y_{\rm seed}$ and $Y_\alpha/Y_{\rm seed}$ are calculated at $T = 3$ GK but the temperature evolution before and after has also an impact on the nucleosynthesis evolution. However, the larger $Y_\alpha/Y_{\rm seed}$ and $Y_{\rm n}/Y_{\rm seed}$, the heavier elements are synthesized (see Sect. 4.2). For even larger $Y_{\rm n}/Y_{\rm seed}$, elements beyond the second r-process peak, $A \sim 130$, are formed (r2, see middle panel in Fig. 4.16). These elements are rather produced by neutron capture reactions than by alpha capture reactions. The conditions in neutrino-driven winds from core-collapse supernovae are not extreme enough to attain such high $Y_{\rm n}/Y_{\rm seed} \sim 100$. The abundance patterns are similar to the ones of neutrino-driven winds from neutron star mergers for $0.25 \leq Y_{\rm e} \leq 0.40$ and low entropies between $S \sim 14 - 23\ k_{\rm B}$/nuc, see upper right and lower left panels in Figs. 5–7 in Ref. [187]. It is remarkable that elements up to the third r-process peak, $A \sim 195$, can be synthesized for $Y_{\rm e} = 0.46 - 0.49$ if $Y_{\rm n}/Y_{\rm seed}$ is large enough (r3, see right panel in Fig. 4.16). Consequently, the neutrino-driven wind could be a host for the r-process for only slightly neutron-rich conditions if the entropy is high enough and/or the expansion time scale is short enough as it was extensively discussed in, e.g., Refs. [74, 111, 118]. For $Y_{\rm e} = 0.45$, the lowest $Y_\alpha/Y_{\rm seed}$ leads to pattern CPR1. As for $Y_{\rm e} = 0.46 - 0.49$, we also find the transition from the nucleosynthesis pattern CPR1 to CPR2, to r2, and to r3 with slightly increasing

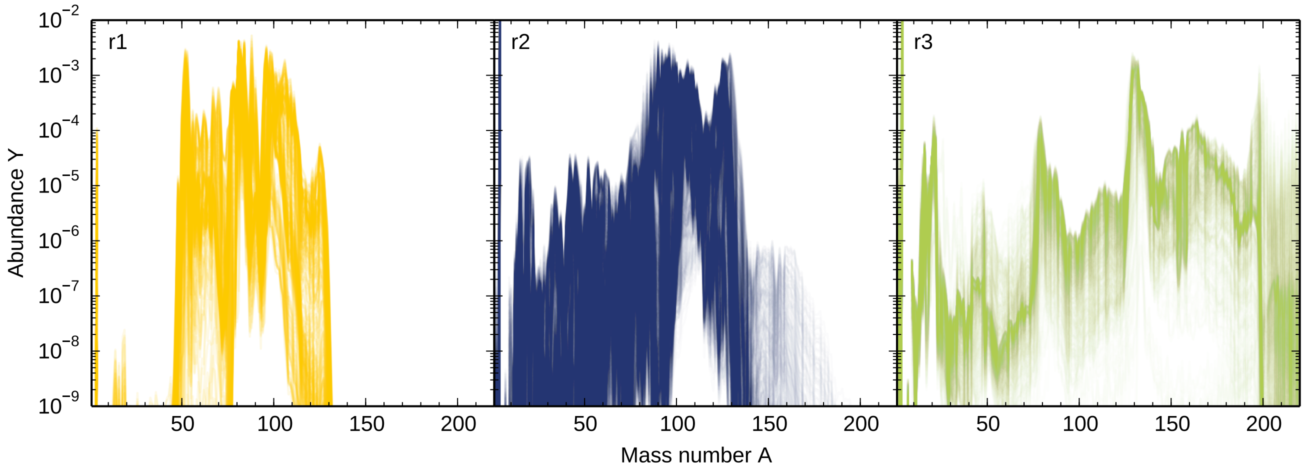

Figure 4.16: Abundance patterns r1 (left panel), r2 (middle panel), and r3 (right panel) after final decay.

$Y_\alpha/Y_{\rm seed}$ and further increasing $Y_n/Y_{\rm seed}$. The transition between the different nucleosynthesis patterns occurs for a smaller $Y_\alpha/Y_{\rm seed}$ compared to $Y_e = 0.46-0.49$. For $Y_e = 0.38-0.44$, the smallest $Y_\alpha/Y_{\rm seed}$ and $Y_n/Y_{\rm seed}$ lead to pattern NSE1. The nucleosynthesis path proceeds close the valley of stability on the neutron-rich side where matter can reach heavier elements only by charged particle reactions because of the long beta decay time scales. Due to the small $Y_\alpha/Y_{\rm seed}$, the alphas are already consumed during the NSE phase, and thus no elements heavier than $Z \sim 40$ are synthesized. With increasing $Y_\alpha/Y_{\rm seed}$, the NSE1 abundance pattern evolves to CPR1. Note that for a given Y_e, the nucleosynthesis groups NSE1 and NSE2 are mutually exclusive. In case of group NSE1 the main mechanism to drive matter towards heavier nuclei are alpha capture reactions, whereas in case of group NSE2 the nucleosynthesis is driven by proton capture reactions. Whether alphas or protons are more abundant depends on the electron fraction. Interesting is the deviation of the dashed black line for $Y_e < 0.38$ which is indicated by the black square in Fig. 4.15. An explanation for this could be that the relation between the wind parameters described in Eq. (20b) in Ref. [111] is not valid for $Y_e < 0.38$. For $Y_e < 0.38$, the electron fraction, the entropy, and expansion time scale are connected by (Eq. (20a) in Ref. [111]):

$$S \propto \left[\frac{1-2Y_e}{[0.33/(Y_e-0.17)]^2-(1/2Y_e)^2}\left(\frac{\tau}{\rm s}\right)\right]^{1/3}. \tag{4.10}$$

The first term leads to a change in the relation between the wind parameters which transfers into $Y_\alpha/Y_{\rm seed}$ and $Y_n/Y_{\rm seed}$. If $Y_e < 0.38$, elements up to $A \sim 130$ (second r-process peak) are synthesized for the lowest $Y_n/Y_{\rm seed}$ and $Y_\alpha/Y_{\rm seed}$ (r1). The abundance patterns are similar to the ones of neutrino-driven winds from neutron star mergers for electron fractions between $0.25 \le Y_e \le 0.40$ and entropies between $S \sim 20-27\ k_B$/nuc, see upper left panels in Figs. 5-7 in Ref. [187]. Therefore, the steady-state model can be also used to describe neutrino-driven winds from neutron star mergers. Due to the small $Y_\alpha/Y_{\rm seed}$, the abundance pattern does not exhibit fingerprints of alpha capture reactions, i.e., abundances for $A \sim 10-50$. The nucleosynthesis pattern r1 evolves to r2 and then to r3 as $Y_n/Y_{\rm seed}$ and $Y_\alpha/Y_{\rm seed}$ increase. Note that there are no smooth transitions between the abundance patterns r1, r2, and r3.

5 Nuclear physics uncertainties in neutron-rich winds

In the following chapter, we want to investigate the impact of nuclear physics uncertainties on the nucleosynthesis in neutron-rich winds. Therefore, we study the nucleosynthesis evolution in neutron-rich winds and inspect which are the main contributing reactions (Sect. 5.1). Afterwards, we discuss and estimate the nuclear physics uncertainties of (α,n) reactions (Sect. 5.2), which mainly move matter towards heavier nuclei in neutron-rich winds. Based on this, in Sect. 5.3, we examine the impact of (α,n) reaction rate uncertainties on the abundances. To identify individual critical (α,n) reactions, we perform a Monte Carlo sensitivity study (Sect. 5.4). The results of the Monte Carlo studies for different astrophysical conditions are presented in Sects. 5.5–5.7. Finally, we combine astrophysical uncertainties and nuclear physics uncertainties and compare to abundance observations of very old stars (Sect. 5.8). The results presented in this chapter are based on an ongoing project together with Almudena Arcones, Fernando Montes and Jorge Pereira. Part of the content presented in this chapter is published in Bliss *et al.* (2017) [168].

5.1 Nucleosynthesis evolution in neutron-rich winds

The nucleosynthesis evolution in neutron-rich winds has been extensively discussed especially for the r-process [74, 111, 118], but also for the weak r-process [45, 119, 121]. Even though both processes consist of neutron captures away from stability, the conditions are significantly different: in the weak r-process the neutron-to-seed ratio is very small, $Y_\mathrm{n}/Y_\mathrm{seed} \lesssim 20$ (see Sects. 4.4.1-4.4.4), compared to the r-process $Y_\mathrm{n}/Y_\mathrm{seed} > 100$. This results in an evolution close to or even along stability for the weak r-process and thus much longer beta decays of the nuclei involved. This is a critical point since beta decays are much slower than the expansion time scale and therefore cannot be the main mechanism to move matter towards higher proton number Z, as in the r-process.

For completeness, we summarize the nucleosynthesis evolution of the weak r-process using a trajectory obtained from spherically symmetric hydrodynamic simulations of neutrino-driven winds [36]. We choose the trajectory ejected 9 s after bounce and an electron fraction $Y_\mathrm{e} = 0.47$, keeping the entropy ($S \approx 86$ $\mathrm{k_B/nuc}$) and expansion time scale ($\tau \approx 11$ ms) as given by the simulation. After the initial NSE phase, various reactions fall out of equilibrium and become important for the final redistribution of matter. Since the wind expansion is faster than beta decays, charged particle reactions are the ones moving matter towards higher Z; these reactions include: (α,γ), (α,n) [1], (p,γ), and (p,n).

In order to analyze this important phase of the weak r-process, one can look at the reaction flows. The flow between two nuclei i and j is defined as

$$F_{ij} \equiv \dot{Y}(i \rightarrow j) - \dot{Y}(j \rightarrow i), \tag{5.1}$$

where $\dot{Y}(i \rightarrow j)$ describes the change in abundance of nucleus i due to all reactions connecting nucleus i with nucleus j. Figure 5.1 illustrates the nucleosynthesis evolution at different temperatures. At $T \approx 5.1$ GK (top panel in Fig. 5.1), the nucleosynthesis path has already reached the Sr, Y, Zr region. In every isotopic chain, the nucleosynthesis path is given by $(\mathrm{n},\gamma)-(\gamma,\mathrm{n})$ equilibrium. Matter reaches higher Z by (α,n) and (p,n) reactions, but (n,α) reactions still occur and carry some matter back to lighter nuclei. Around $T \approx 4.2$ GK (middle panel in Fig. 5.1), (p,n) reactions are less important, while (α,n) reactions keep moving mater towards heavier nuclei. Note that besides increasing the proton number Z by two units, the specific isotope resulting from a given (α,n) channel depends on the number of neutrons emitted in that channel. However, as long as $(\mathrm{n},\gamma)-(\gamma,\mathrm{n})$ reactions are in equilibrium and much faster than (α,n), the isotopic distribution within a given element is ultimately defined by the temperature, neutron density, and neutron separation energy [142]. For typical weak r-process temperatures, the $(\alpha,1\mathrm{n})$ channel dominates the (α,n) reaction flux [48]. In agreement with Ref. [28], we find that in neutron-rich winds (α,n) reactions on Zn, Ge, Se, and Kr are key to shift matter to heavier isotopes.

---

[1] Here (α,n) refers also to alpha captures with the emission of one or more neutrons: $(\alpha,\times\mathrm{n})$, with $\times = 1, 2, 3$.

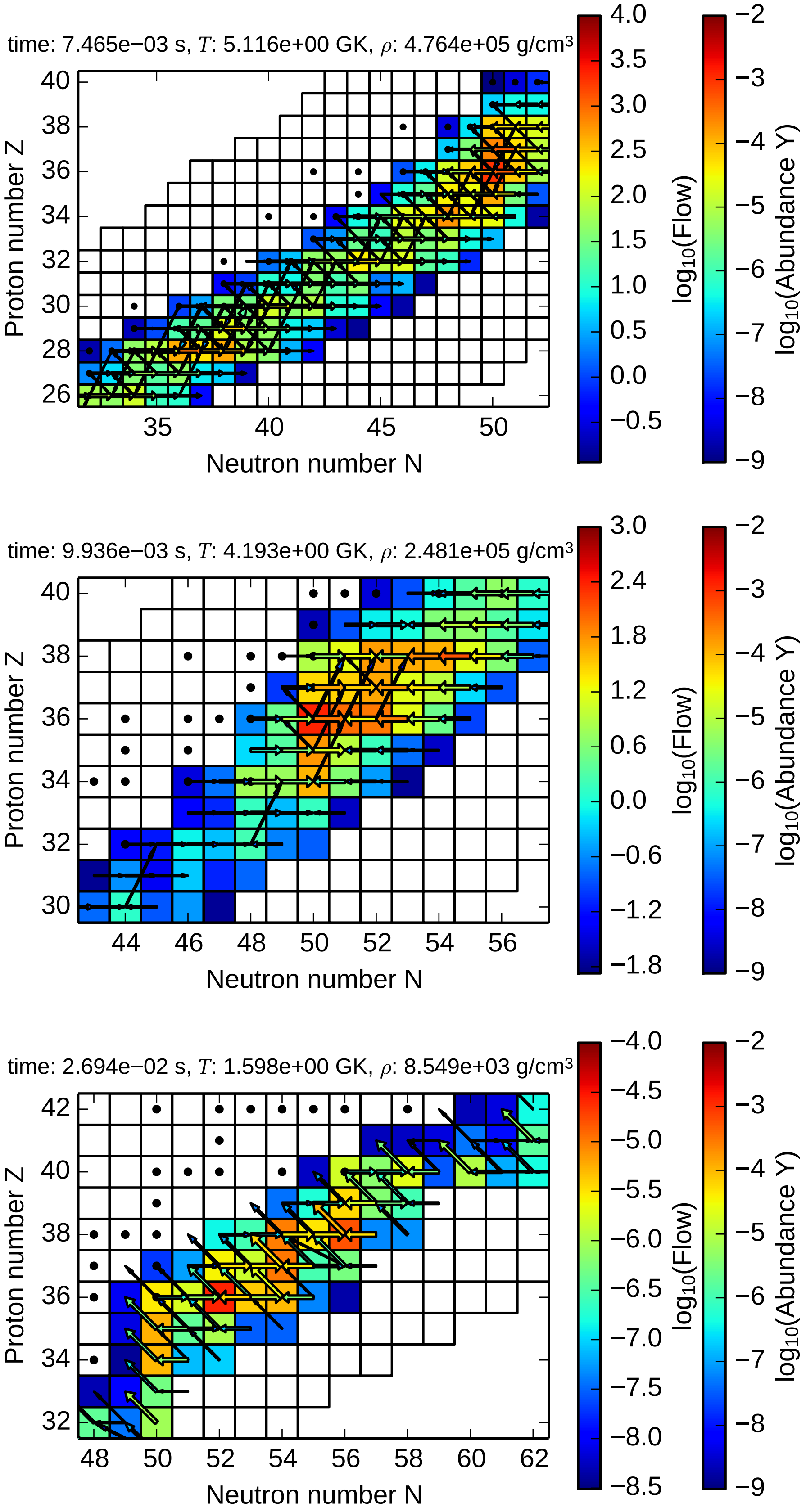

Figure 5.1: The arrows show the flow of the different reactions. The colors and sizes of the arrows are proportional to the flows. The abundances are shown by different colors and stable nuclei are indicated by black dots.

The description of the nucleosynthesis can be completed by considering the averaged time scales, $\langle\tau_x\rangle$, of the most relevant reactions calculated as follows:

$$\frac{1}{\langle\tau_x\rangle} = \frac{\sum_{Z,A}\lambda_x(Z,A)Y(Z,A)}{\sum_{Z,A}Y(Z,A)}, \tag{5.2}$$

where $\lambda_x(Z,A)$ describes the reaction rate of process x on nucleus (Z,A) and $Y(Z,A)$ is the abundance of the nucleus. The averaged time scales for $Z = 26-45$ are presented in Fig. 5.2 versus decreasing temperature. The fastest reactions are (n,γ) and (γ,n) which stay in equilibrium until the temperature drops below $T \approx 1.5$ GK. For temperatures above $T \approx 4.2$ GK, (p,n) reactions are the fastest charged particle reactions. Note that in the fluxes (Fig. 5.1), (p,n) reactions and beta decays are represented in the same way, however considering the time scales it is clear that the driving reactions are (p,n) and not beta decays for $T > 1.9$ GK. Below $T \approx 4.2$ GK, (α,n) reactions become faster than (p,n) reactions and they determine the nucleosynthesis evolution until the temperature drops down to $T \approx 3.3$ GK. At low temperatures (bottom panel in Fig. 5.1), the evolution is driven by beta decays and neutron captures instead of charged particle reactions. There is a temperature range for which a type of reaction is important and this depends on the astrophysical conditions. For example, for $Y_\mathrm{e} = 0.45$, the (α,n) reactions are already very important around $T \sim 4.5$ GK. For only slightly neutron-rich conditions ($Y_\mathrm{e} \sim 0.49$), the nucleosynthesis path stays close to stability and both (p,γ) and (α,γ) reactions become more important to reach heavier nuclei, while (α,n) reactions play a minor role.

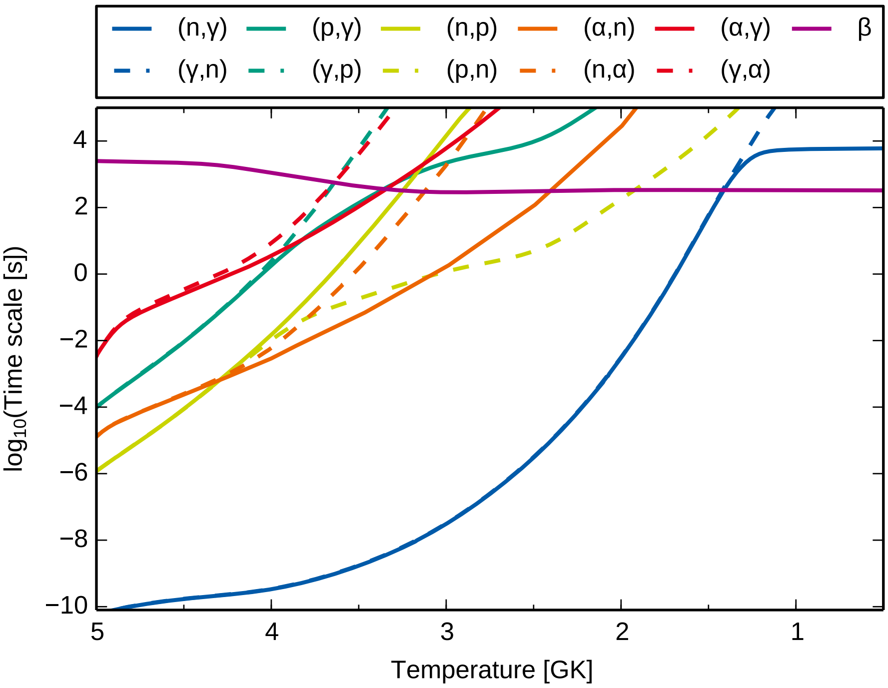

Figure 5.2: Averaged time scales of important reactions as a function of temperature. This correspond to the trajectory ejected 9 s after bounce with an initial electron fraction of $Y_\mathrm{e} = 0.47$.

5.2 Uncertainties in the (α,n) reaction rates

The reaction flows (Fig. 5.1) and the temperature evolution of the averaged reaction time scales $\langle\tau_x\rangle$ (Fig. 5.2) emphasize that (α,n) reactions are important for the weak r-process nucleosynthesis. Unfortunately, none of the relevant (α,n) reactions has been measured in the energy (temperature) range relevant for the astrophysical conditions discussed here. Therefore, one needs to use reaction codes, such as TALYS [158] or NON-SMOKER [188], to calculate all the reaction rates entering into our nucleosynthesis network. Although these codes are based on the Hauser-Feshbach model [46], they can include important differences related to 1) intrinsic technical aspects and 2) nuclear physics inputs [47, 48]. This arbitrariness in the treatment of the reaction leads to variations in the calculated rates. In a recent study [48], the theoretical uncertainty of a selected group of (α,n) reactions relevant for the weak r-process was investigated. According to that work, $(\alpha,1n)$ is by far the most important $(\alpha,\times n)$ channel at temperatures relevant for the weak r-process between $T\simeq 2-5$ GK (see also Ref. [162] for further information about $(\alpha,\times n)$ channels). Moreover, at these temperatures, the uncertainty in the calculated rates arises from the different models used to determine the alpha optical potential. In particular, the rates calculated using these different models can disagree by more than a factor 10 at temperatures $T\simeq 2$ GK [48, 162]. This is illustrated in Fig. 5.3 for the reactions ^{69}Ga$(\alpha,\mathrm{n})^{72}$As, ^{84}Se$(\alpha,\mathrm{n})^{87}$Kr, ^{94}Sr$(\alpha,\mathrm{n})^{97}$Zr, and ^{100}Mo$(\alpha,\mathrm{n})^{103}$Ru. We include here also ^{69}Ga and ^{100}Mo because we use them later to compare experimental and theoretical cross sections (Fig. 5.4).

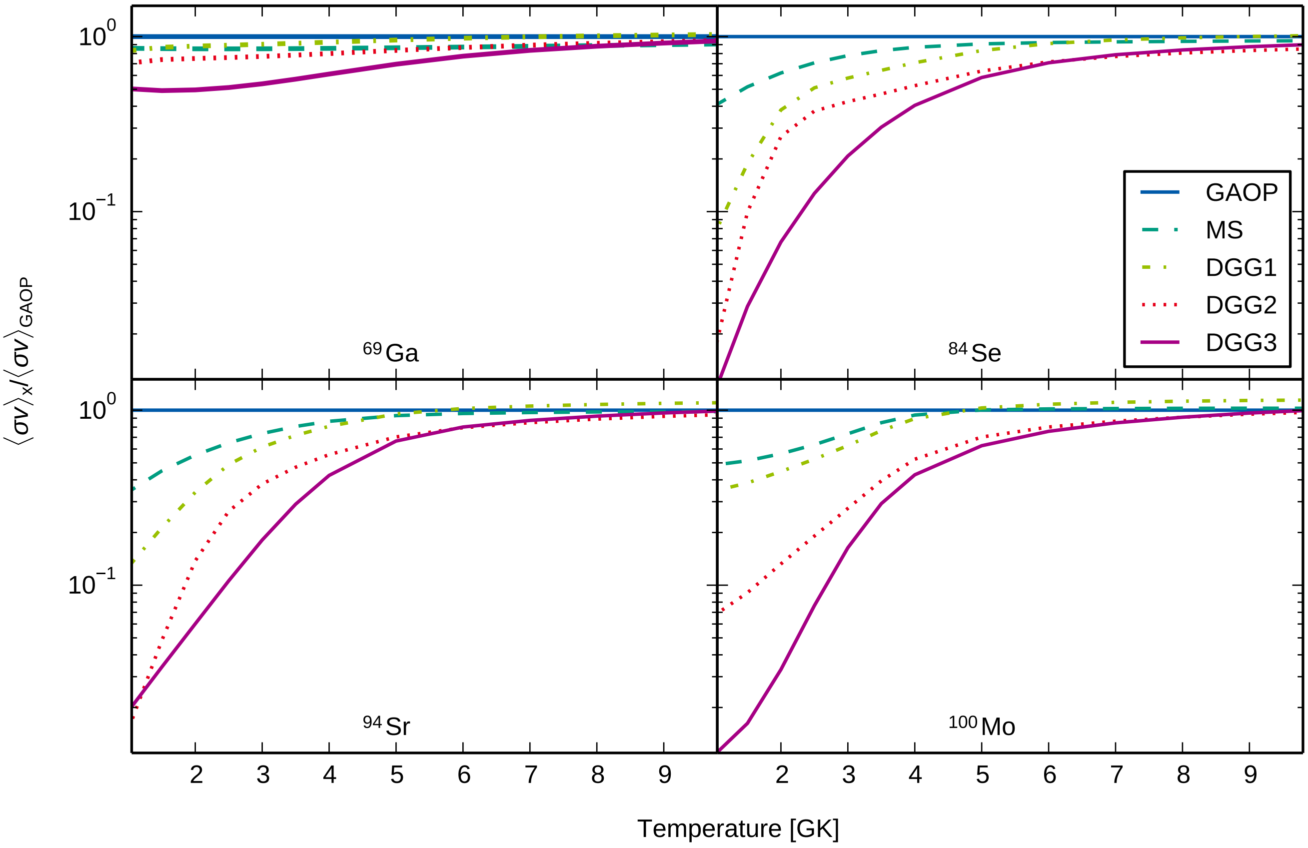

Figure 5.3: Theoretical ^{69}Ga$(\alpha,\mathrm{n})^{72}$As, ^{84}Se$(\alpha,\mathrm{n})^{87}$Kr, ^{94}Sr$(\alpha,\mathrm{n})^{97}$Zr, and ^{100}Mo$(\alpha,\mathrm{n})^{103}$Ru reaction rates using the alpha optical potentials: global alpha optical potential (GAOP) [158, 164], phenomenological fit of McFadden and Satchler (MS) [165], three different versions of the model of Demetriou-Grama-Goriely (DGG1-3) [158, 166] (the other nuclear inputs are determined from the default set of sources given in [48], with the exception of masses, which were taken from Ref. [189] if available, or from the FRDM mass model [190] otherwise). The reaction rates are normalized to the ones calculated with the GAOP model.

While ambiguities in the alpha optical potentials govern the theoretical uncertainty at $T\simeq 2-5$ GK, there are other aspects (e.g., level densities and binning of excitation energy) contributing to the theoretical uncertainty of the (α,n) reaction rates [48]. Although these aspects were found to have a rather limited impact in the calculated rates, larger discrepancies (of the order of ∼10) can be found between calculations and measurements at temperatures above the weak r-process regime, as shown in Fig. 5.4 for some (α,n) reactions. Notice that we compare with measurements of stable nuclei in absence of relevant experiments for the weak r-process where mainly unstable nuclei are involved.

In the light of the conclusions discussed in Ref. [48] and the results shown in Fig. 5.4, it is reasonable to assume that the reliability of the calculated (α,n) rates is not better than a factor 10. In the following, we will investigate the sensitivity of abundances to (α,n) uncertainties. We first calculate weak r-process abundances taking the (α,n) TALYS 1.6 reaction rates calculated with the packet of models TALYS 1 (see Table II of Ref. [48]) except for masses, which were taken from the mass table of Ref. [189] if available, or from the FRDM mass model [190] otherwise. Then, we repeat the network calculations using the TALYS rates multiplied and divided by different factors, namely 5, 10, and 50.

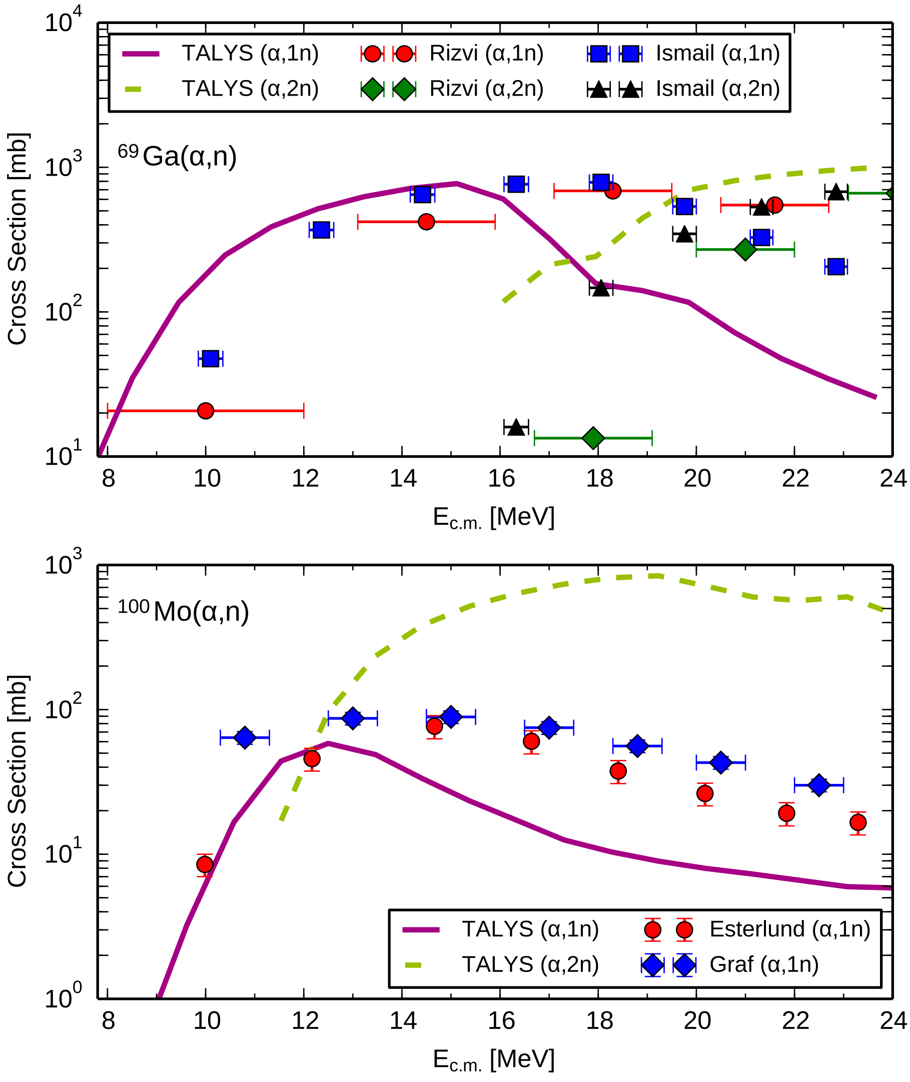

Figure 5.4: Comparison of experimental and calculated cross sections for the reactions ^{69}Ga$(\alpha, 1\mathrm{n})$, ^{69}Ga$(\alpha, 2\mathrm{n})$ [191] (upper panel), and ^{100}Mo$(\alpha, 1\mathrm{n})$, ^{100}Mo$(\alpha, 2\mathrm{n})$ [192] (lower panel). The calculations were done with TALYS using the global alpha optical potential (GAOP).

5.3 Impact of (α, n) reaction rate uncertainties on the abundances

We study the impact of (α, n) reaction rate uncertainties on the abundances based on the trajectory introduced in Sect. 5.1 for different Y_e as discussed in Sect. 4.2. We focus here on three initial electron fractions, i.e., $Y_e = 0.45$, 0.47, and 0.49 and vary the (α, n) reaction rates by constant factors (see Sect. 5.2). Since the forward and reverse reactions are connected by the principle of detailed balance (see Eq. (3.20)), we have to vary the corresponding (n, α) rates by the same factors. Figure 5.5 (left panels) shows the final abundances for $Y_e = 0.47$ when the (α, n) and (n, α) reaction rates are multiplied (upper panel) and divided (lower panel) by factors of 5, 10, and 50 for all isotopes between Fe and Rh. The relative abundance changes compared to the reference case are shown in the right panels of Fig. 5.5. All scaling factors have significant impact on the abundances. When the (α, n) reactions become the fastest charged particle reactions, the most abundant species are within the range $26 \lesssim Z \lesssim 40$ (Figs. 5.1-5.2) and their abundances become thus sensitive to (α, n) reaction rates within this range (see also Ref. [28]).

When the (α, n) rates are reduced (bottom panels, Fig. 5.5), less efficient alpha captures prevent nuclear matter from moving towards heavier nuclei, and thus the abundances stay higher between $27 < Z < 38$ compared to the reference case. This is clearly visible in the relative changes of abundances shown in the right bottom panel of Fig. 5.5. The abundances for $Z < 38$ increase proportionally to the reduction factor used for the (α, n) reactions. As less matter is moved beyond $Z = 38$, the abundance for nuclei heavier than Zr decreases as indicated by the negative values of the relative changes. The opposite behavior is found for the increase of the rates (upper panels,

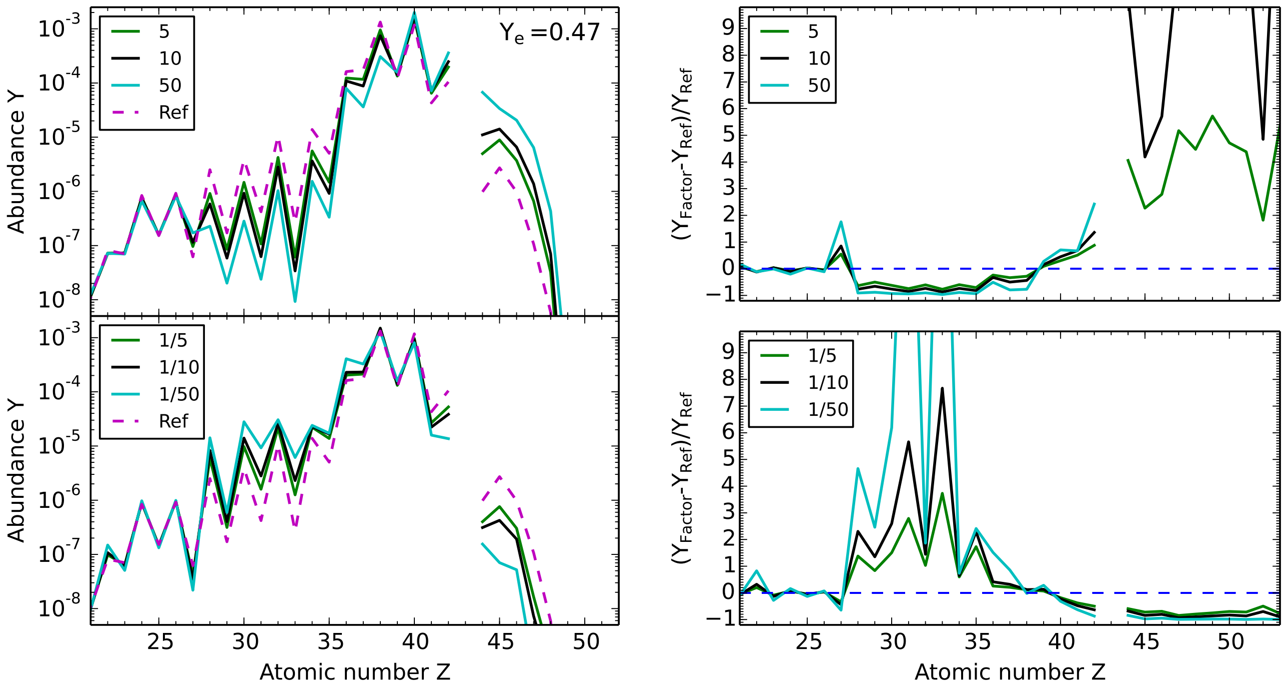

Figure 5.5: Left panels: Elemental abundances when multiplying (upper panels) and dividing (lower panels) the (α,n) reaction rates by factors 5, 10, and 50 for $Z = 26-45$. The reference case corresponds to the 9 s trajectory with $Y_e = 0.47$ with the original TALYS-calculated (α,n) rates. Right panels: Relative changes of the abundances compared to the reference.

Fig. 5.5), where the abundances of these nuclei become larger compared to the reference case. The relative changes (upper, right panel) are now negative for $Z < 38$ indicating the reduction of abundances for such nuclei. The more efficient (α,n) reactions move matter towards heavier nuclei as shown by the large and positive values (that go up to ~ 100) for the relative abundance change.

Notice that the impact of (α,n) uncertainties on Y and Zr is relatively small (see right panels Fig. 5.5). For these conditions, there are almost no (α,n) reactions above Kr as shown by the reaction flows (Fig. 5.1). The (α,n) reactions on Kr isotopes are very important because they influence the abundances of the Sr isotopes directly. The flow from Sr isotopes towards heavier ones is mainly driven by (α,n) reactions on Zr, (p,n) reactions, and beta decays.

We have described the general trends of the abundances when varying the (α,n) reaction rates for the trajectory with $Y_e = 0.47$. The trend is the same for $Y_e = 0.45$ (Fig. 5.6). The main difference is the large variation in the abundance of Sr and the heaviest elements mainly due to (α,n) reactions on Rb and Sr isotopes. For both conditions $Y_e = 0.45$ and 0.47, there are also the changes in the abundances for $Z < 26$ nuclei, whose (α,n) rates are not scaled in our study. The change of these abundances is due to neutron captures that occur on all isotopes and are affected by the amount of neutrons available including the ones produce after (α,n) reactions. For $Y_e = 0.49$, there is almost no effect when changing the (α,n) reactions. Here, the nucleosynthesis path moves along the valley of stability where (p,γ), (p,n) and few strong contributing (α,γ) reactions move matter towards heavy nuclei.

After studying the impact of different nucleosynthesis evolutions (various electron fractions) and of nuclear physics input due to (α,n) reactions, we can combine these two uncertainties and compare to abundance observations of metal-poor stars. In Fig. 5.7, we show abundance ratios between pairs of lighter heavy element abundances in observations compared to our results. For the observations, we use metal-poor stars with typical r-process robust pattern (CS22892-052 [193]) and with low-enrichment of heavy elements (HD122563 and HD88609 [194]) which are illustrated by pink and blue stars, respectively. For a detailed discussion about these representative patterns see Ref. [24]. In Fig. 5.7, the horizontal lines indicate the value of the abundance ratio between a given pair of elements A and B using the reference TALYS (α,n) rates discussed in Sect. 5.2 (thicker line) and varying this by factors 10 and 0.1. Different colors of the horizontal lines corresponds to different electron fractions (i.e., different nucleosynthesis paths). For $Y_e = 0.45$, there are large variations in the Zr/Sr, Nb/Sr, and Ag/Zr abundance ratios

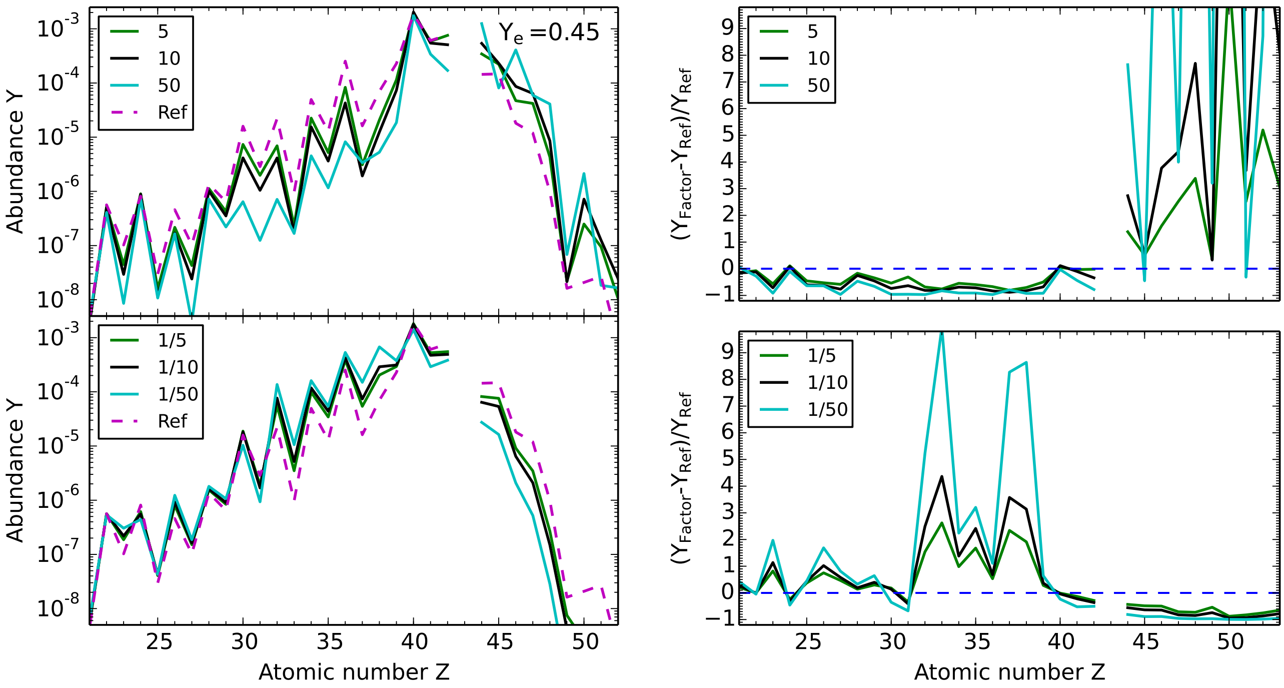

Figure 5.6: Same as Fig. 5.5 for $Y_e = 0.45$.

owing to the strong influence of (α, n) rates on the abundances of Sr and Ag (Fig. 5.6). For ratios including heavier elements, i.e., Ru or Ag, there is more scatter due to the low abundances that rapidly drop for increasing proton number. In the case of $Y_e = 0.47$, the variations in the Zr/Sr and Nb/Sr ratios can be explained by the impact of (α, n) reactions on Sr and Nb abundances (Fig. 5.5). For $Y_e = 0.49$ we only show the Zr/Sr and Zr/Y abundance ratios because the final abundances do not reach nuclei heavier than $Z \sim 40$ (Fig. 4.1). Due to the small influence

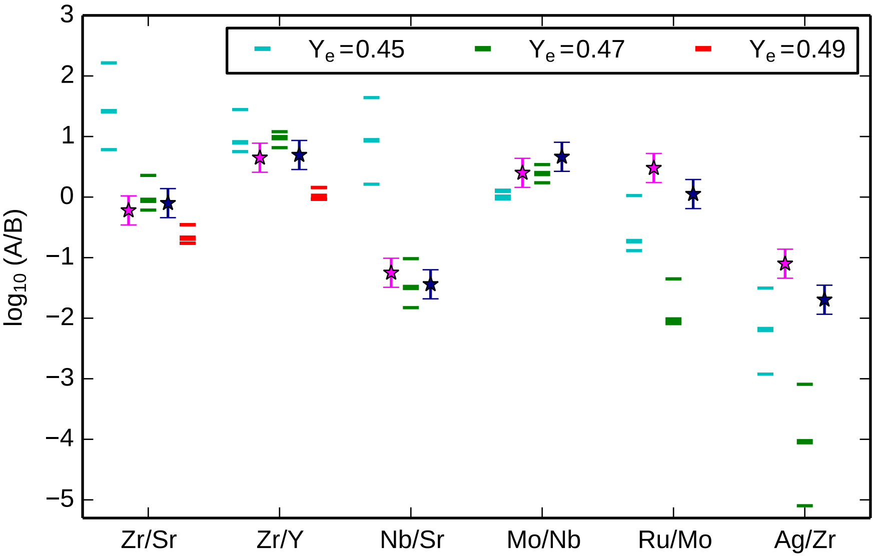

Figure 5.7: Elemental abundance ratios compared to observations from averaged HD122563 and HD88609 (blue stars), and CS22892-052 (pink stars) for different electron fractions. Note that we only illustrate the Zr/Sr and Zr/Y abundance ratios for $Y_e = 0.49$ because the final abundances do not reach nuclei heavier than $Z \sim 40$ (Fig. 4.1). The horizontal lines indicate the abundance ratio of the pair of elements: the thicker lines correspond to the reference TALYS rates, whereas the thin lines correspond to the reference rates scaled by factors of 10 and 0.1.

of (α,n) rates for $Y_\mathrm{e}=0.49$, the abundance ratios do not differ much when changing the rates. As Fig. 5.7 shows, it is clear that to make full use of the metal-poor observations when comparing to astrophysical models, nuclear physics uncertainties need to be reduced. In general, the various nucleosynthesis evolutions given by different values of Y_e fail to reproduce the trend from Zr/Sr through Ag/Zr. Our aim here is not to find the exact astrophysical conditions that reproduce observations, but to combine astrophysics and nuclear physics uncertainties to show that both are critical to understand the production of lighter heavy elements. Once experiments reduce the nuclear physics uncertainties, observations of ultra-metal poor stars combined with nucleosynthesis studies will contribute to understand the post-explosion conditions. In the following sections, we will describe our Monte Carlo sensitivity study within astrophysical uncertainties in neutron-rich winds to motivate key (α,n) reactions which will reduce the impact of nuclear physics uncertainties on the nucleosynthesis.

5.4 Monte Carlo approach

The sequential variation of a set of reaction rates by the same factor gives an overview if the rate uncertainties have an impact on the abundances. For large networks containing several thousands of nuclei or complicated reaction flows, the modification of the reaction rate by the same factor may (partially) suppress important reactions or point out reactions which are not relevant. Therefore, this method is not recommended to identify key reactions. Moreover, the identification of key reactions by inspection of the reaction flows may be feasible for small networks with a well defined nucleosynthesis path (e.g., Big Bang nucleosynthesis networks) but not if many reactions contribute to the nucleosynthesis evolution. For larger networks, only a Monte Carlo approach allows to identify which individual reaction rate uncertainty contributes to the abundance change of a given nuclei. Besides, only Monte Carlo studies take into account combined reaction rate uncertainties.

In a Monte Carlo sensitivity study, random numbers are applied to a set of reaction rates to independently vary them within their uncertainties. The reaction rate uncertainties are mapped on the abundances via the reaction network. In each Monte Carlo run, new random numbers are drawn to the set of reaction rates. Today's fast computers make it possible to perform a sufficient amount of Monte Carlo runs, even for large reaction networks containing several thousands nuclei. Note that the required computational time is rather independent of the number of modified reaction rates but largely depends on the time to solve the reaction network. For a sufficient amount of Monte Carlo runs, the key reaction rates are identified by analyzing the correlations between the variations of the rates and the resulting abundance changes. We will describe in detail the variation of the reaction rates and the identification of key reactions in Sects. 5.4.1–5.4.2.

The Monte Carlo method of drawing random numbers to reaction rates has been already used for several astrophysical applications. For example, Ref. [195] has performed a Monte Carlo sensitivity study for the nucleosynthesis in Type I X-ray bursts and Refs. [196, 197] in nova explosions. Besides, e.g., Refs. [198] and [199] have done Monte Carlo studies for the p- and s-process nucleosynthesis, respectively, and Ref. [200] for the r-process nucleosynthesis, especially reverse engineering [201]. Furthermore, thermonuclear reaction rates have been evaluated based on Monte Carlo techniques by Refs. [202–205].

We will use the Monte Carlo approach to examine which (α,n) reaction rate uncertainties lead to changes in the abundance pattern in neutron-rich winds.

5.4.1 Variation of reaction rates

In our Monte Carlo study, we consider 909 (α,n) reactions on stable and neutron-rich nulei between Fe and Rh. We again use the reference (α,n) reaction rates calculated with TALYS 1.6 using the packet of models TALYS 1 (see Table II of Ref. [48]) except for masses, which were taken from the mass table of Ref. [189] if available, or from the FRDM mass model [190] otherwise. In each Monte Carlo run, the (α,n) reaction rates are varied simultaneously and independently by applying a set of random rate variation factors on them. The rate variation factors follow a lognormal distribution which is given by

$$f(x;\mu,\sigma)=\frac{1}{\sqrt{2\pi}\sigma x}\exp\left[\frac{-(\ln x-\mu)^2}{2\sigma^2}\right], \tag{5.3}$$

where μ and σ are the mean value and the standard deviation on $\ln x$, respectively. Note that if x is lognormally distributed, $\ln x$ is normally distributed. Thus, the parameter μ describes the maximum of the Gaussian distribution for $\ln x$ and the parameter σ represents the width of the distribution. The lognormal density function is only defined for $x \geq 0$. Consequently, the rate variation factors are always positive and we do not obtain unphysical, negative reaction rates. Since the forward and the reverse reaction are connected by detailed balance, the reverse (n,α) reaction rate has to be varied by the same factor (see Eq. (3.20)).

For a data sample $\{p_1, p_2, ..., p_n\}$ which is lognormally distributed, the geometric mean μ^* and the geometric standard deviation σ^* are described by

$$\mu^* \equiv \sqrt[n]{p_1 \cdot p_2 \cdot ... \cdot p_n} = e^{\mu} \quad \text{and} \quad \sigma^* \equiv \exp\left[\sqrt{\frac{1}{n}\sum_{i=1}^{n}\left(\ln\frac{p_i}{\mu^*}\right)^2}\right] = e^{\sigma}, \tag{5.4}$$

respectively. Thus, the median of the lognormal distribution is given by e^{μ}. For a coverage probability of 68.3 % , i.e., a point x is located within 1σ of the mean $(\mu - \sigma < x < \mu + \sigma)$, the lower and upper bounds are determined by $\mu^*/\sigma^* = e^{\mu-\sigma}$ and $\mu^* \cdot \sigma^* = e^{\mu+\sigma}$, respectively (see, e.g., Ref. [202]). Therefore, for a coverage probabilbity of 68.3 %, the rate variation factor p with respect to the median is given by $p = e^{\mu+\sigma}/e^{\mu} = e^{\mu}/e^{\mu-\sigma}$ (see, e.g., Refs. [202, 204]). Consequently, to generate a rate variation factor between 0.1 and 10, modifying the (α,n) reaction rates within their uncertainties (see Sect. 5.2), we set $\mu = 0$ and $\sigma = 2.3$. As an example, Fig. 5.8 illustrates the distribution of the rate variation factors applied to the $^{84}\mathrm{Se}(\alpha,\mathrm{n})$ reaction rate. The solid, dashed and dashed-dotted lines indicate the median, one standard deviation and two standard deviations, respectively, of the rate variation factor distribution. Figure 5.8 shows that approximately 68.3 % of all rate variation factors are within a factor of 10 up and down, and 95.5 % are within a factor of 100 up and down. Unlike Refs. [198, 199], we assume that the rate variation factor is independent of the temperature. Note that there is only a small range of temperatures where an (α,n) reaction is relevant for the weak r-process.

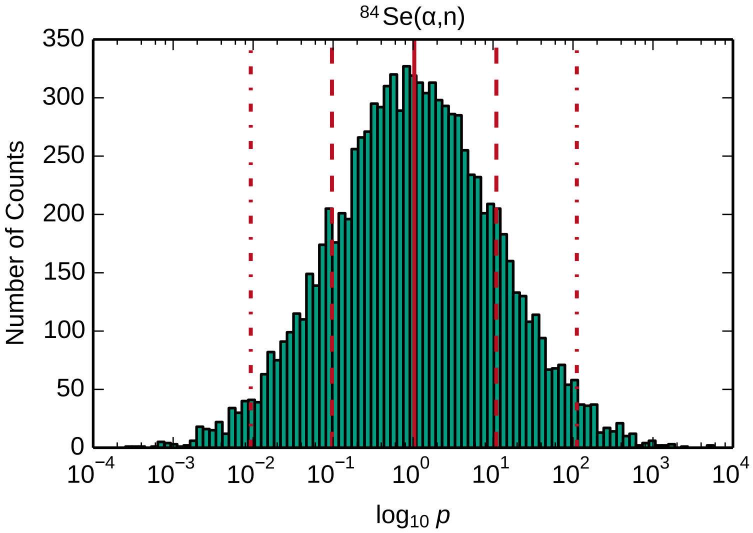

Figure 5.8: Distribution of the rate variation factors applied to the $^{84}\mathrm{Se}(\alpha,\mathrm{n})$ reaction rate. The solid, dashed, and dashed-dotted lines display the median, one standard deviation, and two standard deviations, respectively.

5.4.2 Identification of key reactions

We have already mentioned that for larger networks it is not sufficient to only consider reaction flows or to compare the impact of few varied reaction rates on the abundances to identify key reactions. From each Monte Carlo run we have stored the rate variation factor of each modified (α,n) reaction and the final abundances. Thus, for each nuclei in the network we can investigate the impact of each modified (α,n) reaction on its abundance using a correlation factor. Most senstivity studies (see, e.g., Refs. [198, 199]) use Pearson's r [206] to quantify the correlations between the rate variation factors and the final abundances. The Pearson correlation coefficient is defined by

$$r_{\mathrm{corr}} = \frac{\sum_{i=1}^{n}(x_i - \bar{x})(y_i - \bar{y})}{\sqrt{\sum_{i=1}^{n}(x_i - \bar{x})^2}\sqrt{\sum_{i=1}^{n}(y_i - \bar{y})^2}}, \tag{5.5}$$

for two data sets $\{x_1, x_2, ..., x_n\}$ and $\{y_1, y_2, ..., y_n\}$ of n values and the corresponding arithmetic mean values $\bar{x} = \left(\sum_{i=1}^{n} x_i\right)/n$ and $\bar{y} = \left(\sum_{i=1}^{n} y_i\right)/n$. The variables x_i and y_i are related to the rate variation factors and the final abundances, respectively. The parameter n in Eq. (5.5) denotes the number of rate variation factors applied to a reaction rate, i.e., the number of Monte Carlo runs. The values of r_{corr} range between $-1 \leq r_{\mathrm{corr}} \leq +1$. If the relation between the rate variation factors applied to a reaction rate and the final abundances of a given element is exact a linear one with positive slope, $r_{\mathrm{corr}} = +1$, and for a negative slope, $r_{\mathrm{corr}} = -1$. A negative value of the correlation factor describes an anticorrelation, i.e., as the rate variation factor increases the abundance decreases and vice versa. If r_{corr} is close to 0, there is no correlation between the rate variation factors and the final abundances. Note that the values of the correlation factor hold independently of the magnitude of the slope. Besides, the value of the correlation factor will be larger the fewer reactions contribute to the abundance uncertainty.

Pearson's r is a measure for linear correlations, but Monte Carlo sensitivity studies frequently show non-linear relations between variations of reaction rates and abundance changes (see, e.g., Fig. 6 in Ref. [204]). Thus, we use the Spearman's correlation coefficient [207]. The Spearman rank-order coefficient quantifies how well the relation between two variables is described by a monotonic function. To obtain Spearman's r, one replaces x_i and y_i in Eq. (5.5) by their actual ranks. A Spearman correlation factor of $+1$ (-1) indicates a perfectly increasing (decreasing) monotonic function. Reference [204] has shown that Spearman's r is more robust than Pearson's r in terms of outlier (see Fig. 6 in Ref. [204]). It is more robust in a similar sense as the median value of a data set is more robust towards outlier than the mean value.

Note that in general correlation factors cannot be used directly to rank the important reactions. The reason for this is that the value of the correlation factor is independent of the absolute abundance change. Therefore, the strategy to identify key reactions is: 1) inspect which abundances vary most in the Monte Carlo study; 2) investigate which reaction rate variations strongly correlate with the abundance changes. We have found that 10000 Monte Carlo runs are sufficient to identify the key reactions. Moreover, we have identified that a correlation factor value $|r_{\mathrm{corr}}| \geq 0.40$ indicates a strong relationship between the modified reaction rate and the abundance change of a given element. In a few cases, a correlation factor describing an important relation can be slightly smaller than $|r_{\mathrm{corr}}| = 0.40$.

5.4.3 Representative astrophysical conditions for the Monte Carlo sensitivity study

Our goal is to get a comprehensive picture of the nuclear physics uncertainties which influence the nucleosynthesis in neutron-rich neutrino-driven winds. Therefore, one needs all possible wind parameters which may occur in neutron-rich winds. In Chapter 4, we have systematically studied the astrophysical uncertainties in neutron-rich winds based on the steady-state wind models of Ref. [102]. We have identified four different nucleosynthesis groups (NSE1, NSE2, CPR1, CPR2) due to the $Y_{\mathrm{n}}/Y_{\mathrm{seed}}$ and the $Y_{\alpha}/Y_{\mathrm{seed}}$ at $T = 3$ GK (see Sects. 4.4.1-4.4.4). These groups distinguish in the nucleosynthesis evolution and thus lead to different final abundances. We have demonstrated that within the groups NSE1, NSE2, CPR1 the nucleosynthesis evolution is similar and therefore results in similar final abundances. For the steady-state trajectories of the nucleosynthesis groups NSE1, NSE2, and CPR1, the nucleosynthesis path does not proceed towards heavier nuclei when the temperature decreases below 3 GK. The reason for this is that the main abundance peaks are already formed during NSE or QSE, and thus the abundance pattern is rather sensitive to binding energies or Q-values of (α, n) reactions than to specific reactions (see Sects. 4.4.1–4.4.3). Moreover, we have shown that the nucleosynthesis evolution leads to substantial changes in the abundance pattern after the temperature drops below 3 GK only for the steady-state trajectories assigned to the nucleosynthesis group CPR2. For the steady-state trajectories of the group CPR2, any variation of the $Y_{\mathrm{n}}/Y_{\mathrm{seed}}$ and the $Y_{\alpha}/Y_{\mathrm{seed}}$ results in a different abundance pattern (see Fig., 4.13). Hence, the abundance patterns of the group CPR2 are very sensitive to specific reactions, and thus to uncertainties in the reaction rates. Consequently, we will select representative steady-state trajectories of the group CPR2 for the Monte Carlo sensitivity study. Since slight variations of the $Y_{\mathrm{n}}/Y_{\mathrm{seed}}$ and the $Y_{\alpha}/Y_{\mathrm{seed}}$ lead to different abundance patterns, it is rather difficult to select representative trajectories. However, the final abundances of the nucleosynthesis group CPR2 (Fig. 4.13) exhibit three characteristic Kr-Rb-Sr-Y-Zr patterns which are illustrated by different colors in Fig. 5.9. Note that the different abundance patterns are especially apparent for Sr. We will refer to the three abundance patterns as MC

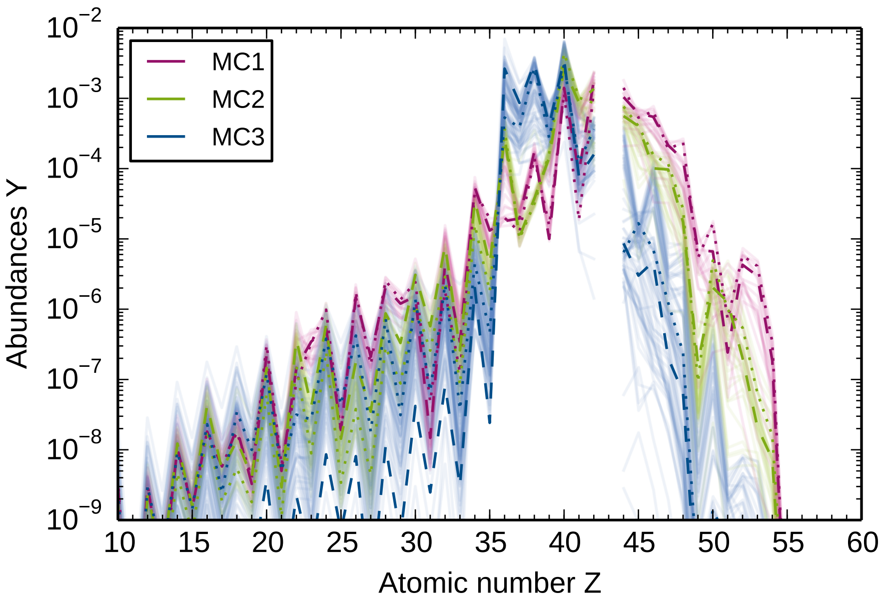

Figure 5.9: Three characteristic Kr-Rb-Sr-Y-Zr patterns in the final abundances of the nucleosynthesis group CPR2 (see Fig. 4.13) indicated by different colors. The different Kr-Rb-Sr-Y-Zr patterns are used to identify representative astrophysical conditions for the Monte Carlo sensitivity study. We perform Monte Carlo studies for the trajectories assigned to the abundance patterns indicated by dashed (reference Monte Carlo studies) and dotted lines (control Monte Carlo studies).

one, MC two, and MC three. We will perform a Monte Carlo study with a representative trajectory of each of the three abundance patterns. The abundances of the corresponding trajectories are indicated by the dashed lines in Fig. 5.9. Since the abundance patterns of the same group can be different for $Z < 36$ and $Z > 41$, we will perform a control Monte Carlo study for each group (dotted lines in Fig. 5.9) to investigate if the abundance deviations lead to different key (α, n) reactions.

5.5 Results of Monte Carlo study one

Figure 5.10 illustrates the impact of the (α, n) reaction rate uncertainties for Fe-Rh on the elemental abundances using the representative trajectory of group MC one (purple dashed line in Fig. 5.9). The purple band shows the 2σ elemental abundance variations from 10000 Monte Carlo runs and the black line denotes the median elemental abundances. The distributions of the elemental abundances closely follow lognormal distributions. This is due to the error multiplication effect occuring when several reactions are contributing to the total uncertainty in the abundance, even if the rate variation factors are not lognormally distributed (see Ref. [198]). The (α, n) reaction rate uncertainties have the largest impact on the abundances for $Z = 36-39$, and especially on yttrium (up to a factor of 95).

To investigate which (α, n) reaction rate uncertainties lead to changes in the elemental abundances, we have calculated the correlation factor for each combination of element abundance and varied (α, n) reaction rate in the 10000 Monte Carlo runs (see Sect. 5.4.2). Compared to other Monte Carlo sensitivity studies (see, e.g., Refs. [198, 199]), we calculate the correlation factors for variations in the reaction rates and changes in the elemental abundances instead of changes in the isotopic abundances. Elemental abundances are most useful for comparison to observations of stars which only provide information on elemental abundances. In Tab. 5.1, the computed correlation factors are given in descending order for $|r_{\mathrm{corr}}| \geq 0.40$. The correlation factors indicate that the uncertainties in the ^{82}Ge(α, n), ^{94}Sr(α, n), ^{84}Se(α, n), ^{90}Kr(α, n), ^{85}Se(α, n) reaction rates strongly correlate with the abundance variations of several elements.

In order to test the reliability of the correlation factor to identify a relationship between the variation of an (α, n) reaction rate and the change in the abundance of a given element, we look at the reaction flows (Fig. 5.11). At $T \approx 3.7$ GK, the most abundant elements are $Z = 34-38$. There an (α, n) reaction occurs on ^{82}Ge, i.e., at the neutron shell closure $N = 50$. Table 5.1 indicates that the modification of this (α, n) reaction rate strongly correlates with the abundances of Se and Kr. Since ^{82}Ge and ^{82}Se are linked by beta decays along the isobaric

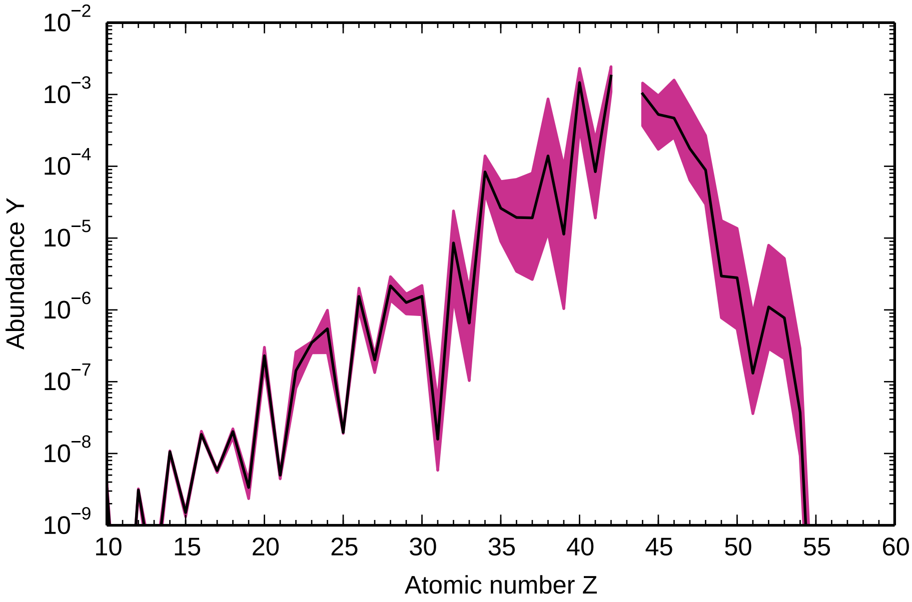

Figure 5.10: Resulting 2σ abundance pattern variations from 10000 Monte Carlo runs using the representative trajectory of group MC one (dashed purple line in Fig. 5.9). The (α, n) reaction rates for $Z = 26 - 45$ are varied by rate variation factors pulled from a lognormal distribution. The black line indicates the median elemental abundances.

Element	Reaction	r_{corr}
Se	$^{82}\mathrm{Ge}(\alpha,\mathrm{n})^{85}\mathrm{Se}$	−0.63
Ag	$^{94}\mathrm{Sr}(\alpha,\mathrm{n})^{97}\mathrm{Zr}$	+0.62
Kr	$^{82}\mathrm{Ge}(\alpha,\mathrm{n})^{85}\mathrm{Se}$	−0.62
Pd	$^{94}\mathrm{Sr}(\alpha,\mathrm{n})^{97}\mathrm{Zr}$	+0.61
Sr	$^{84}\mathrm{Se}(\alpha,\mathrm{n})^{87}\mathrm{Kr}$	−0.57
Zr	$^{90}\mathrm{Kr}(\alpha,\mathrm{n})^{93}\mathrm{Sr}$	−0.57
Ru	$^{94}\mathrm{Sr}(\alpha,\mathrm{n})^{97}\mathrm{Zr}$	−0.57
Rb	$^{84}\mathrm{Se}(\alpha,\mathrm{n})^{87}\mathrm{Kr}$	−0.54
Sr	$^{85}\mathrm{Se}(\alpha,\mathrm{n})^{88}\mathrm{Kr}$	−0.53
Rb	$^{85}\mathrm{Se}(\alpha,\mathrm{n})^{88}\mathrm{Kr}$	−0.50
Y	$^{84}\mathrm{Se}(\alpha,\mathrm{n})^{87}\mathrm{Kr}$	−0.49
Cd	$^{94}\mathrm{Sr}(\alpha,\mathrm{n})^{97}\mathrm{Zr}$	+0.49
Ga	$^{90}\mathrm{Kr}(\alpha,\mathrm{n})^{93}\mathrm{Sr}$	−0.49
Y	$^{85}\mathrm{Se}(\alpha,\mathrm{n})^{88}\mathrm{Kr}$	−0.48
Cu	$^{90}\mathrm{Kr}(\alpha,\mathrm{n})^{93}\mathrm{Sr}$	−0.48
Zn	$^{90}\mathrm{Kr}(\alpha,\mathrm{n})^{93}\mathrm{Sr}$	−0.47
Ni	$^{90}\mathrm{Kr}(\alpha,\mathrm{n})^{93}\mathrm{Sr}$	−0.46
Fe	$^{90}\mathrm{Kr}(\alpha,\mathrm{n})^{93}\mathrm{Sr}$	−0.46
Rh	$^{90}\mathrm{Kr}(\alpha,\mathrm{n})^{93}\mathrm{Sr}$	+0.42
Co	$^{90}\mathrm{Kr}(\alpha,\mathrm{n})^{93}\mathrm{Sr}$	+0.41
Mo	$^{84}\mathrm{Se}(\alpha,\mathrm{n})^{87}\mathrm{Kr}$	+0.41
In	$^{94}\mathrm{Sr}(\alpha,\mathrm{n})^{97}\mathrm{Zr}$	+0.40

Table 5.1: Correlation factors (third column) describing the relationships between the variation of the reaction rates (second column) and the change of the elemental abundances (first column) in the Monte Carlo study one. A positive (negative) correlation factor indicates that the elemental abundance raises (decreases) as the (α, n) reaction rate increases.

chain $A = 82$, the change of the ^{82}Ge(α, n) reaction rate directly affects the Se abundance. The variation of the ^{82}Ge(α, n) reaction rate indirectly influences the Kr abundance, i.e., only in combination with (n, γ) reactions and beta decays. When the temperature drops down to $T \approx 3.3$ GK the ^{82}Ge(α, n) reaction stops. Besides, we find (α, n) reactions on ^{84}Se and ^{85}Se which also correlate strongly with the abundances of several elements. Both reactions, ^{84}Se(α, n) and ^{85}Se(α, n) correlate with the abundances of the same elements but the correlation with the slightly more abundant ^{84}Se is always stronger. Besides, ^{84}Se(α, n) competes with ^{84}Se(p, n). The correlation factors indicate a clear relationship between the modification of the ^{84}Se(α, n) and ^{85}Se(α, n) reaction rates and the variations in the final abundances of Sr, Y, and to a lesser extent of Mo. In addition, the reaction flows exhibit the reaction ^{86}Se which only weakly correlates (i.e., $|r_{\mathrm{corr}}| = 0.20$) with the Sr abundance. A possible explanation is that an increase of the (α, n) reaction rates on the more abundant ^{84,85}Se isotopes moves more material away from the Se isotope chain, and thus the reaction ^{86}Se(α, n) does not occur. This explanation is confirmed by that the fact that we only find correlations between the modifications of the ^{84,85}Se(α, n) reaction rates and the changes of the Sr, Y, and Mo abundances if these (α, n) rates are raised. Both, ^{84}Se(α, n) and ^{85}Se(α, n) freeze out at $T \approx 3.5$ GK, whereas ^{86}Se(α, n) appears until the temperature drops down to $T \approx 3.1$ GK. Since ^{88}Kr and ^{88}Sr are connected by beta decays along the isobaric chain $A = 88$, the variation of the ^{85}Se(α, n)^{88}Kr reaction rate directly influences the Sr abundance, whereas the modifications of the ^{84,85}Se(α, n) reaction rates affect the Y and Mo abundances only combined with (n, γ) and (p, n) reactions, and beta decays. Material is shifted from ^{84,85,86}Se to the krypton isotopes by (α, n) reactions. The most abundant Kr isotope is ^{90}Kr, thus the nucleosynthesis path has overcome $N = 50$. According to Tab. 5.1, the final abundance of Kr is strongly correlated with the ^{82}Ge(α, n) reaction rate uncertainty. Since the ^{82}Ge(α, n) reaction rate only influences the Kr abundance in combination with (n, γ) reactions and beta decays, this is an indirect impact. Note that the reaction ^{84}Se(α, n) has no influence on the krypton abundance, although ^{84}Se and the stable ^{84}Kr are linked by beta decays. There are several (α, n) reactions on Kr isotopes, i.e., ^{88,89,90}Kr, and each of these (α, n) reactions competes with a (p, n) reaction. However, only the ^{90}Kr(α, n) reaction rate correlates ($|r_{\mathrm{corr}}| \geq 0.40$) with the abundances of several elements, i.e., Zr, Ga, Cu, Zn, Ni, Fe, Rh, and Co in descending order. An explanation for this is that the increase of the (α, n) reaction rate of the most abundant Kr isotope, ^{90}Kr, moves material away from the Kr isotopes, and thus the reactions ^{88,89}Kr(α, n) do not occur. The ^{90}Kr(α, n) reaction ends at $T \approx 3.1$ GK, whereas the ^{88,89}Kr(α, n) reactions already freeze out around $T \approx 3.6$ GK. Only the abundance of ^{90}Zr is directly affected by the variation of the ^{90}Kr(α, n) reaction rate. The elements with lower atomic numbers than krypton are influenced due to the altered neutron abundance caused by the variation of the ^{90}Kr(α, n) reaction rate. The nucleosynthesis path evolves from Kr to Sr where we only find one (α, n) reaction,

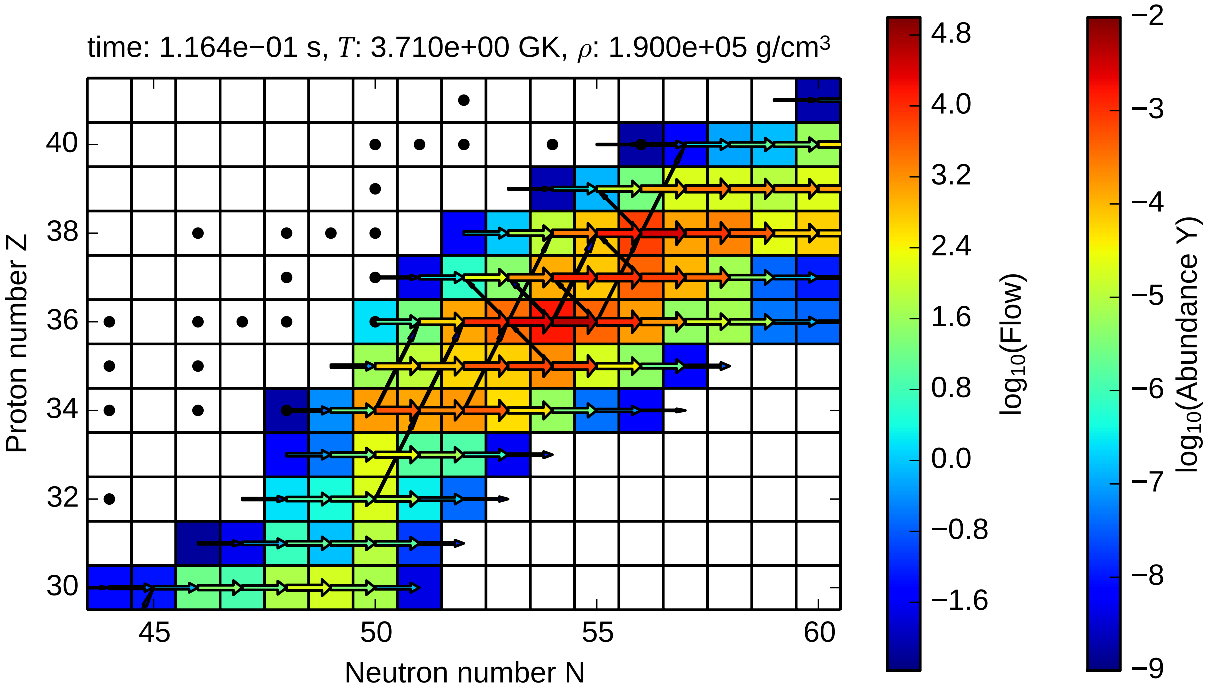

Figure 5.11: Nucleosynthesis evolution at $T \approx 3.7$ GK for the representative trajectory of group MC one without modification of (α, n) reaction rates.

namely ^{94}Sr(α, n). Table 5.1 indicates a strong relationship between the variation of the ^{94}Sr(α, n) reaction rate and the changes of the silver, palladium, ruthenium, and to a lesser extent of the cadmium and indium abundances. The abundances of these elements are influenced by the modification of the ^{94}Sr(α, n) reaction rate combined with (n, γ) reactions and beta decays. The ^{94}Sr(α, n) reaction competes with the ^{94}Sr(p, n) reaction. When the temperature falls below $T \approx 3.6$ GK, the ^{94}Sr(α, n) reaction does not appear. Note that according to the correlation factors (i.e., $|r_{\text{corr}}| \geq 0.40$) and the reaction flows, there is no important (α, n) reaction above Sr. The variations of the ^{84,85}Se(α, n), ^{90}Kr(α, n), and ^{94}Sr(α, n) reaction rates shift the position of the nucleosynthesis path, and thus to different decay paths resulting in the abundance uncertainties beyond Mo.

The reaction flows verify that the (α, n) reactions, which correlate with the elemental abundances according to Tab. 5.1, occur during the nucleosynthesis evolution. Nonetheless, the correlation factor is not a measure for the absolute abundance change (see Sect. 5.4.2). Figure 5.12 illustrates the four strongest correlations we have identified. In the upper left panel in Fig. 5.12, the scatter plot shows how the selenium abundance changes when the reaction ^{82}Ge(α, n) reaction rate is varied by the rate variation factor p. The different colors indicate the frequency of the same abundance for the same rate variation factor. The scatter plot shows that an increase of the ^{82}Ge(α, n) reaction rate leads to a decrease of the selenium abundance. Note that the spread along the y-axis is caused by combined uncertainties of all (α, n) reaction rates. The impact of the variation of the ^{82}Ge(α, n) reaction rate on the Se abundance is less than a factor of 4. The krypton abundance also decreases as the ^{82}Ge(α, n) reaction rate increases (see top right panel in Fig. 5.12). Here, the change in the Kr abundance is less than a factor of 20.

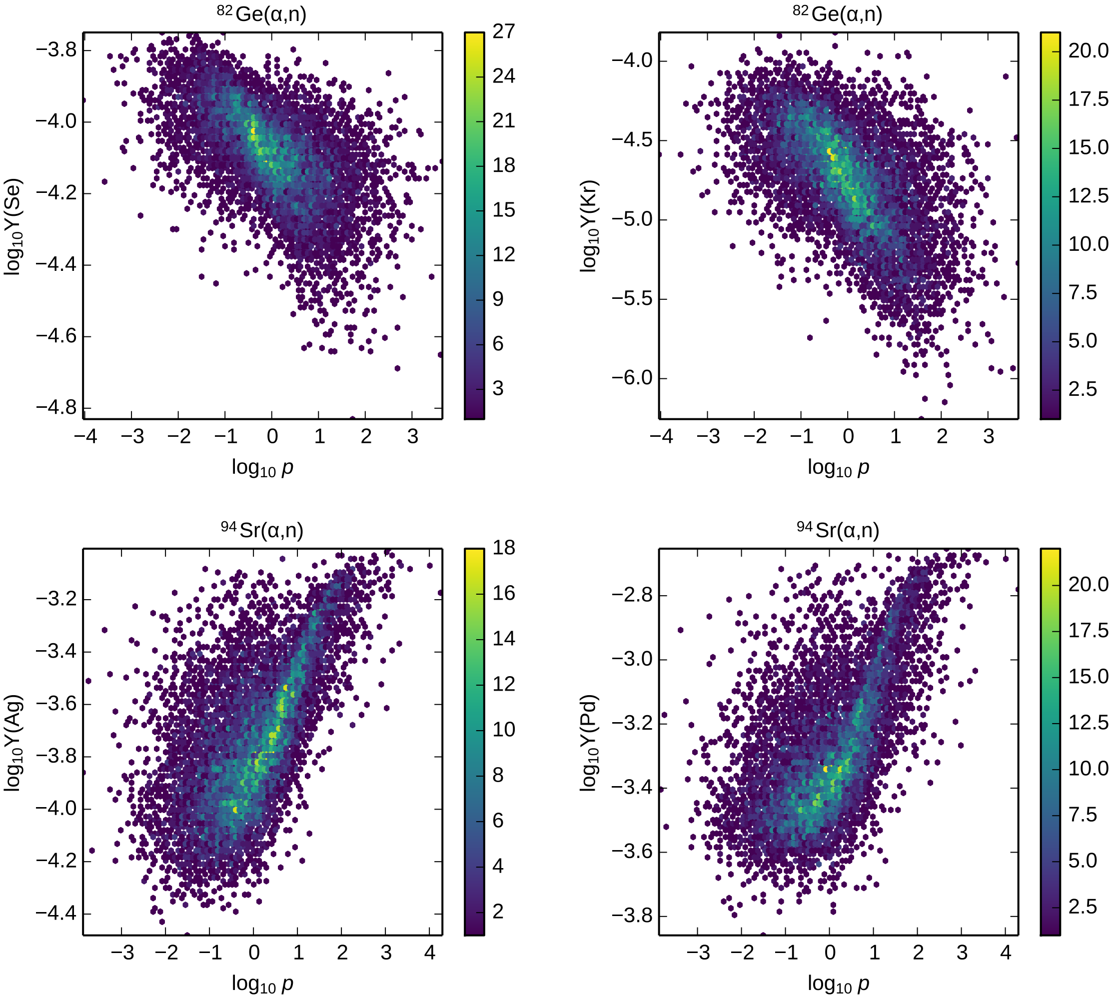

Figure 5.12: Overview of the four strongest correlations between reaction rate variations and abundance changes in the Monte Carlo study one. Final abundances of Se (top left panel), Kr (top right panel), Ag (bottom left panel), and Pd (bottom right panel) versus rate variation factor for modified ^{82}Ge(α, n) (first row) and ^{94}Sr(α, n) (second row) reaction rates. The different colors denote the frequency of the same abundance for the same rate variation factor.

The modification of the ^{82}Ge(α, n) reaction rate influences the selenium and krypton abundance in a similar way. An increase of the ^{82}Ge(α, n) reaction rate moves more matter towards heavier nuclei and thus less material decays to the stable selenium and krypton isotopes. The left panel at the bottom of Fig. 5.12 indicates that an increase of the ^{94}Sr(α, n) reaction rate results in a larger silver abundance. When the ^{94}Sr(α, n) reaction rate is raised, more material is shifted towards heavier elements, and thus the Ag abundance is larger. We find the same trend for the impact of ^{94}Sr(α, n) reaction rate on the abundance of Pd (bottom right panel in Fig. 5.12). However, the effect on the palladium abundance is slightly weaker than on the silver abundance. A reason for this is that palladium has a higher atomic number than silver, and so benefits less from the additional material moving towards heavier elements due to the increase of the ^{94}Sr(α, n) reaction rate. The impact of the ^{94}Sr(α, n) reaction rate uncertainty on the abundances of Ag and Pd is less than a factor of ~ 7 and ~ 11, respectively. Even if the ^{82}Ge(α, n) and ^{94}Sr(α, n) reaction rate uncertainties strongly correlate with the Se, Ag, and Pd abundances, they do not lead to large changes in the abundances. Thus, despite the clear correlation between the variation of the ^{94}Sr(α, n) reaction rate and the changes of the abundances, a reduction of the ^{84}Sr(α, n) reaction rate uncertainty will only slightly improve the uncertainties in the overall abundance pattern.

As mentioned before, the (α, n) reaction rate uncertainties have a significant impact on the abundances for $Z = 36-39$. We have already seen that the uncertainty in the Kr abundance is mainly governed by the modification of the ^{82}Ge(α, n) reaction rate. According to the computed correlation factors, the uncertainties in the abundances of Rb, Sr, and Y arise (in descending order) from the variation of the ^{84}Se(α, n) and ^{85}Se(α, n) reaction rates. Note that Ref. [48] has found that different alpha optical potentials lead to differences in the calculated ^{84,85}Se(α, n) reaction rates of up to two orders of magnitude at temperatures $T \lesssim 4$ GK. The calculated ^{84}Se(α, n) reaction rates using different alpha optical potentials are also shown in the top right panel of Fig. 5.3. Figure 5.13 illustrates the impact of the ^{84}Se(α, n) (left column) and ^{85}Se(α, n) (right column) reaction rates on the abundances of Rb (first row), Sr (second row), and Y (third row). The abundances of these elements decrease all when increasing the ^{84,85}Se(α, n) reaction rates. The variation of the ^{84}Se(α, n) reaction rate also correlates with the uncertainty of the Mo abundance. Here, the trend is that a higher ^{84}Se(α, n) reaction rate leads to an increase of the molybdenum abundance. Since the additional material reaching Mo has to come from nuclei with lower atomic number, i.e., $Z = 37-39$, the Rb, Sr, and Y abundances decrease as the Mo abundance increases.

To verify if the abundance uncertainties shown in Fig. 5.10 are mainly due the ^{82}Ge(α, n) and ^{84,85}Se(α, n) reaction rates uncertainties, we only vary these reaction rates and their reverse by a factor of 50 up and down (Fig. 5.14). The comparison between Figs. 5.10 and 5.14 indicates that the modification of only these three (α, n) reactions leads to the similar uncertainties in the abundance pattern as resulting from the Monte Carlo study. Note that only an increase of the ^{82}Ge(α, n) and ^{84,85}Se(α, n) reaction rates results in significant variations of the abundances for $Z = 36-39$.

To investigate if the variation of the ^{82}Ge(α, n) and ^{84,85}Se(α, n) reaction rates also leads to comparable changes in the overall abundance for other trajectories of the group MC one, or the uncertainties of other (α, n) reaction rates are relevant, we have performed a control Monte Carlo study with another trajectory of group MC one (purple dotted line in Fig. 5.9). The influence of the (α, n) reaction rate uncertainties for $Z = 26-45$ on the overall abundance pattern using the control trajectory is comparable to the abundance variations illustrated in Fig. 5.11. To probe if the same (α, n) reaction rate uncertainties lead to the variations of the abundance pattern, we compare the correlations in both Monte Carlo studies (see Tabs. 5.1 and 5.2). The correlation factors are larger in the control Monte Carlo study. However, we identify the same correlations for $|r_{\text{corr}}| \geq 0.40$ in both Monte Carlo studies, only in a different ranking. Consequently, for the astrophysical conditions investigated here, the reduction of the ^{82}Ge(α, n), ^{84,85}Se(α, n) reaction rate uncertainties will significantly contribute to decrease the abundance uncertainties of the lighter heavy elements between Kr and Y due to nuclear physics uncertainties. The measurement of these reactions combined with observations of lighter heavy elements in UMP stars will give evidence if the astrophysical conditions of group MC one are realistic conditions in neutrino-driven winds.

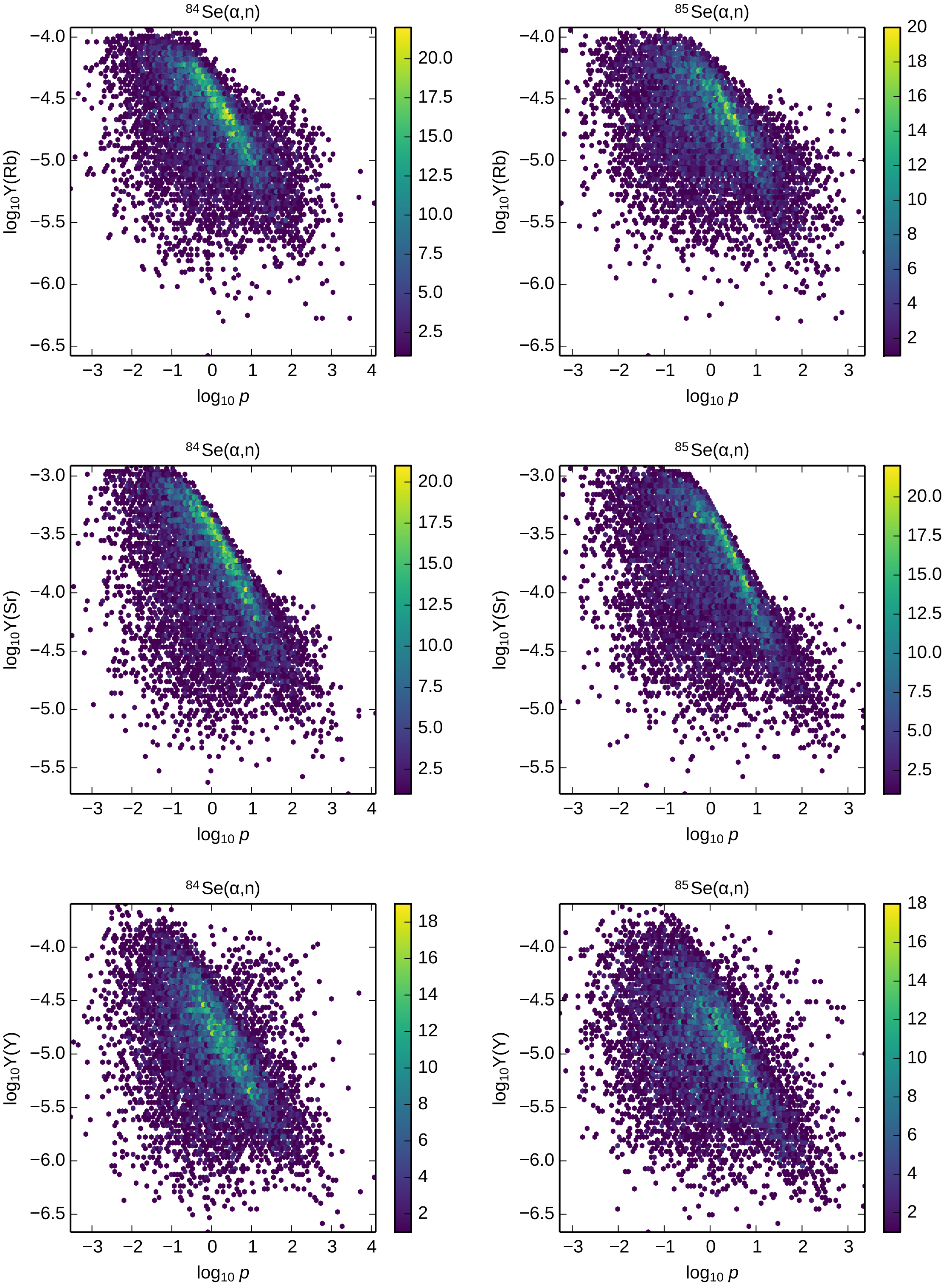

Figure 5.13: Final abundances of Rb (first row), Sr (second row), Y (third row) versus rate variation factor for the modified $^{84}\mathrm{Se}(\alpha,\mathrm{n})$ (left column) and $^{85}\mathrm{Se}(\alpha,\mathrm{n})$ (right column) reaction rates. The abundances of Rb, Sr, Y strongly vary in the Monte Carlo study one.

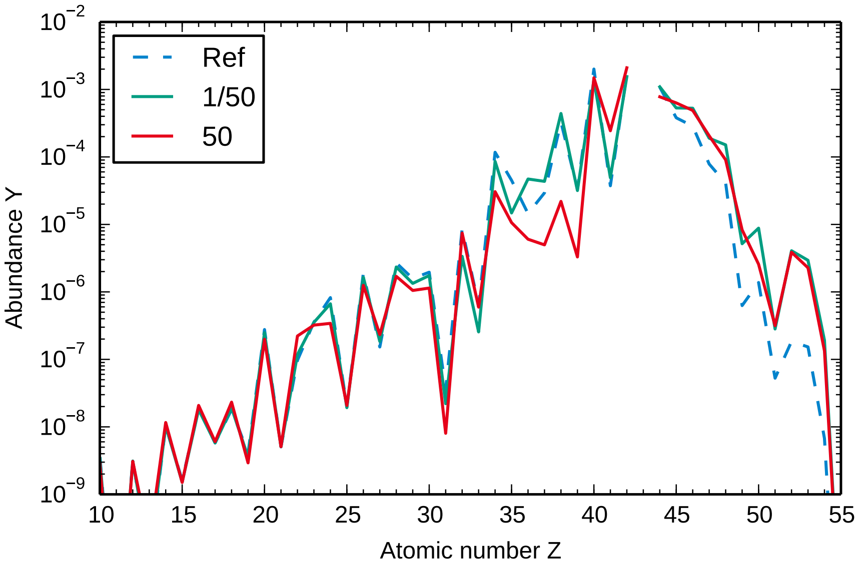

Figure 5.14: Elemental abundances for the representative trajectory of group MC one and variation of the $^{82}\mathrm{Ge}(\alpha,\mathrm{n})$, $^{84}\mathrm{Se}(\alpha,\mathrm{n})$, and $^{85}\mathrm{Se}(\alpha,\mathrm{n})$ reaction rates by a factor of 50 up (red) and down (green). The reference case corresponds to the original TALYS-calculated (α,n) reaction rates without variation of (α,n) reaction rates.

Element	Reaction	r_{corr}
Kr	$^{82}\mathrm{Ge}(\alpha,\mathrm{n})^{85}\mathrm{Se}$	−0.84
Ru	$^{94}\mathrm{Sr}(\alpha,\mathrm{n})^{97}\mathrm{Zr}$	−0.61
Ag	$^{94}\mathrm{Sr}(\alpha,\mathrm{n})^{97}\mathrm{Zr}$	+0.61
Cd	$^{94}\mathrm{Sr}(\alpha,\mathrm{n})^{97}\mathrm{Zr}$	+0.58
Zr	$^{90}\mathrm{Kr}(\alpha,\mathrm{n})^{93}\mathrm{Sr}$	−0.57
Sr	$^{84}\mathrm{Se}(\alpha,\mathrm{n})^{87}\mathrm{Kr}$	−0.56
Rb	$^{84}\mathrm{Se}(\alpha,\mathrm{n})^{87}\mathrm{Kr}$	−0.54
Y	$^{84}\mathrm{Se}(\alpha,\mathrm{n})^{87}\mathrm{Kr}$	−0.54
In	$^{94}\mathrm{Sr}(\alpha,\mathrm{n})^{97}\mathrm{Zr}$	+0.52
Mo	$^{84}\mathrm{Se}(\alpha,\mathrm{n})^{87}\mathrm{Kr}$	+0.51
Sr	$^{85}\mathrm{Se}(\alpha,\mathrm{n})^{88}\mathrm{Kr}$	−0.51
Pd	$^{94}\mathrm{Sr}(\alpha,\mathrm{n})^{97}\mathrm{Zr}$	+0.50
Rb	$^{85}\mathrm{Se}(\alpha,\mathrm{n})^{88}\mathrm{Kr}$	−0.49
Y	$^{85}\mathrm{Se}(\alpha,\mathrm{n})^{88}\mathrm{Kr}$	−0.49
Ga	$^{90}\mathrm{Kr}(\alpha,\mathrm{n})^{93}\mathrm{Sr}$	−0.48
Cu	$^{90}\mathrm{Kr}(\alpha,\mathrm{n})^{93}\mathrm{Sr}$	−0.47
Zn	$^{90}\mathrm{Kr}(\alpha,\mathrm{n})^{93}\mathrm{Sr}$	−0.47
Rh	$^{90}\mathrm{Kr}(\alpha,\mathrm{n})^{93}\mathrm{Sr}$	+0.46
Ni	$^{90}\mathrm{Kr}(\alpha,\mathrm{n})^{93}\mathrm{Sr}$	−0.46
Fe	$^{90}\mathrm{Kr}(\alpha,\mathrm{n})^{93}\mathrm{Sr}$	−0.45
Se	$^{82}\mathrm{Ge}(\alpha,\mathrm{n})^{85}\mathrm{Se}$	−0.45
Co	$^{90}\mathrm{Kr}(\alpha,\mathrm{n})^{93}\mathrm{Sr}$	+0.43

Table 5.2: Same as Tab. 5.1 for the control trajectory of group MC one.

The resulting abundance pattern variations from the Monte Carlo study using the selected trajectory of group MC two (green dashed line in Fig. 5.9) are shown in Fig. 5.15. The (α,n) reaction rate uncertainties have the largest impact (in descending order) on the elemental abundances of Kr, Rb, Ga, Zn, and Sr. In comparison to the Monte Carlo study one, the (α,n) reaction rate uncertainties have also a significant impact on the elements for $Z < 36$.

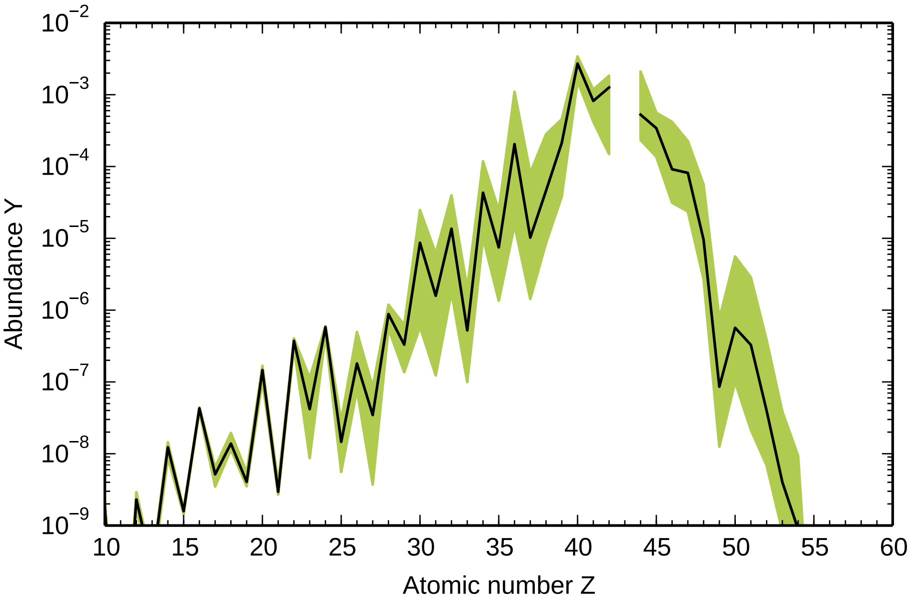

Figure 5.15: Resulting 2σ abundance pattern variations from 10000 Monte Carlo runs for the representative trajectory of group MC two (dashed green line in Fig. 5.9).

To understand which (α,n) reaction rates lead to changes in the abundance pattern, we consider again the nuclear reaction flows (Fig. 5.16) and the correlation factors (Tab. 5.3). The reaction flows display (α,n) reactions on Fe isotopes, especially on ^{68}Fe. According to Tab. 5.3, the variation of the ^{68}Fe(α,n) reaction rate strongly correlates with the final Zn abundance. In addition, the modification of the ^{68}Fe(α,n) reaction rate influences the Ga abundance, but in less extent. When the ^{68}Fe(α,n) reaction rate is raised, more material is shifted away from the iron isotopes to heavier elements. Since the matter moves from Fe to Zn and Ga during the decay, an increase of the ^{68}Fe(α,n) reaction rate leads to a decrease of the final Zn and Ga abundances. As we have mentioned before, there are a large uncertainties in the Zn and Ga abundances (see Fig. 5.15). The correlations between the variation of the ^{68}Fe(α,n) reaction rate and the change of the Zn (see right panel at the bottom of Fig. 5.17) and Ga (left panel at the bottom of Fig. 5.17) abundances mainly occur for rate variation factors larger than one. The large spread in the gallium abundance for similar rate variation factors indicates that several combined (α,n) reaction rate uncertainties contribute to its uncertainty. Therefore, the change of the ^{68}Fe(α,n) reaction rate cannot alone explain the uncertainty of the Ga abundance. The ^{68}Fe(α,n) reaction stops for temperatures below $T \approx 3.4$ GK. The nuclear reaction flows exhibit the ^{72}Ni(α,n) reaction which correlates with the final Ge abundance (see Tab. 5.3). When the ^{72}Ni(α,n) reaction rate is increased, more matter proceeds from the Ni isotope chain towards heavier nuclei, and thus less matter decays to germanium. The reaction ^{81}Ga(α,n) does not appear in the fluxes. A possible explanation is that this reaction is suppressed when the (α,n) reaction rates for $Z = 26-45$ are not varied. The simultaneous changes of the reaction rates lead to the appearance of the ^{81}Ga(α,n) reaction. The fluxes show that an (α,n) reaction occurs on ^{82}Ge. As in the previous Monte Carlo studies, the modification of the ^{82}Ge(α,n) reaction rate strongly correlates with the final abundance of Se. In contrast to the first Monte Carlo study, the variation of the ^{82}Ge(α,n) reaction rate only affects the Se abundance. Figure 5.16 displays that the ^{84,85}Se(α,n) reactions also contribute to the nucleosynthesis evolution. The change of the ^{84,85}Se(α,n) reaction rates correlates with the abundances of krypton (first row in Fig. 5.17), rubidium (second row in Fig. 5.17), zirconium (but is only related to ^{84}Ge(α,n)), and strontium, in descending order, and the correlation with the more abundant ^{84}Se(α,n) at $N = 50$ is always stronger. The correlation between the variation of the ^{84,85}Se(α,n) reaction rates and the change of the final Kr abundance has not been found in the Monte Carlo study one. An increase of the ^{84}Se(α,n) reaction rate moves matter away from ^{84}Se that would beta decay along the isobaric chain to ^{84}Kr. Since a $(\mathrm{n},\gamma)-(\gamma,\mathrm{n})$ equilibrium is established within the selenium isotopic chain, the modification of the ^{85}Se(α,n) reaction rate also affects the Kr abundance, because it influences if more or less material proceeds towards heavier nuclei, and thus less or more matter decays to Kr. The variations of the ^{84,85}Se(α,n) reaction rates influence the final abundance of Rb, Sr, and Y in the same way as in the Monte Carlo study one (see Sect. 5.5). As in the first Monte Carlo study, the uncertainties of the ^{84,85}Se(α,n) reaction rates are important for the uncertainties in the overall abundance pattern. Furthermore, we find that the variation of the yttrium abundance correlates with the^{85}Br(α,n) reaction rate uncertainty. If the ^{85}Br(α,n) reaction rate is raised, more matter is shifted from Br to Rb where matter proceeds further away from stability by (n,γ) reactions. Thus, less matter indirectly decays from rubidium to yttrium. The correlation between the final yttrium abundance and the ^{85}Br(α,n) reaction rate uncertainty has not been found in the Monte Carlo study one. An explanation for this is that for the astrophysical conditions investigated here, the nucleosynthesis path evolves closer to the valley of stability, and the path overcomes $N = 50$ at a higher atomic number resulting in a larger accumulation of matter at ^{85}Br. Nonetheless, the overall changes of the yttrium abundance due to (α,n) reaction rate uncertainties are small (see Fig. 5.15). The reaction flows also present (α,n) reactions on ^{88,89,90}Kr. As we have seen in the Monte Carlo study one, the modification of the ^{90}Kr(α,n) reaction rate influences the final abundances of several elements (here Co, Fe, Cu, and Ni in descending order), and these elements are mainly affected by changes in the neutron abundance due to the varied ^{90}Kr(α,n) reaction rate. The ^{88,89}Kr(α,n) reactions also contribute to the nucleosynthesis evolution, but the (α,n) reaction rate uncertainties have no significant impact on the abundances (see Sect. 5.5). As in the Monte Carlo study one, the reaction flows and correlations factors do not indicate important (α,n) reactions beyond Sr. The uncertainties in the final abundances of Pd, Ru, Mo, Ag, and Rh are mainly due to the variation of the ^{94}Sr(α,n) reaction rate. The modification of the ^{94}Sr(α,n) reaction rate alters the position of the nucleosynthesis path, and thus to different decay paths which result in the uncertainties in the abundances beyond Zr. Note that the relation between the ^{94}Sr(α,n) reaction rate uncertainty and the molybdenum abundance has not been found in the Monte Carlo study one.

To investigate if the modification of the ^{68}Fe(α,n), ^{72}Ni(α,n), ^{81}Ga(α,n), ^{82}Ge(α,n), ^{84,85}Se(α,n), ^{85}Br(α,n), ^{90}Kr(α,n), and ^{94}Sr(α,n) reaction rates causes the uncertainties in the overall abundance pattern (Fig. 5.15), we only vary these (α,n) reaction rates by a factor of 50 up and down (see Fig. 5.18). The comparison between Figs. 5.15 and 5.18 indicates that the variation of only these (α,n) reaction rates cannot fully explain the overall uncertainties of the abundances. The variation of the abundance pattern is not as strongly pronounced as in the Monte Carlo study. This also indicates that Monte Carlo sensitivity studies are necessary to study the impact of

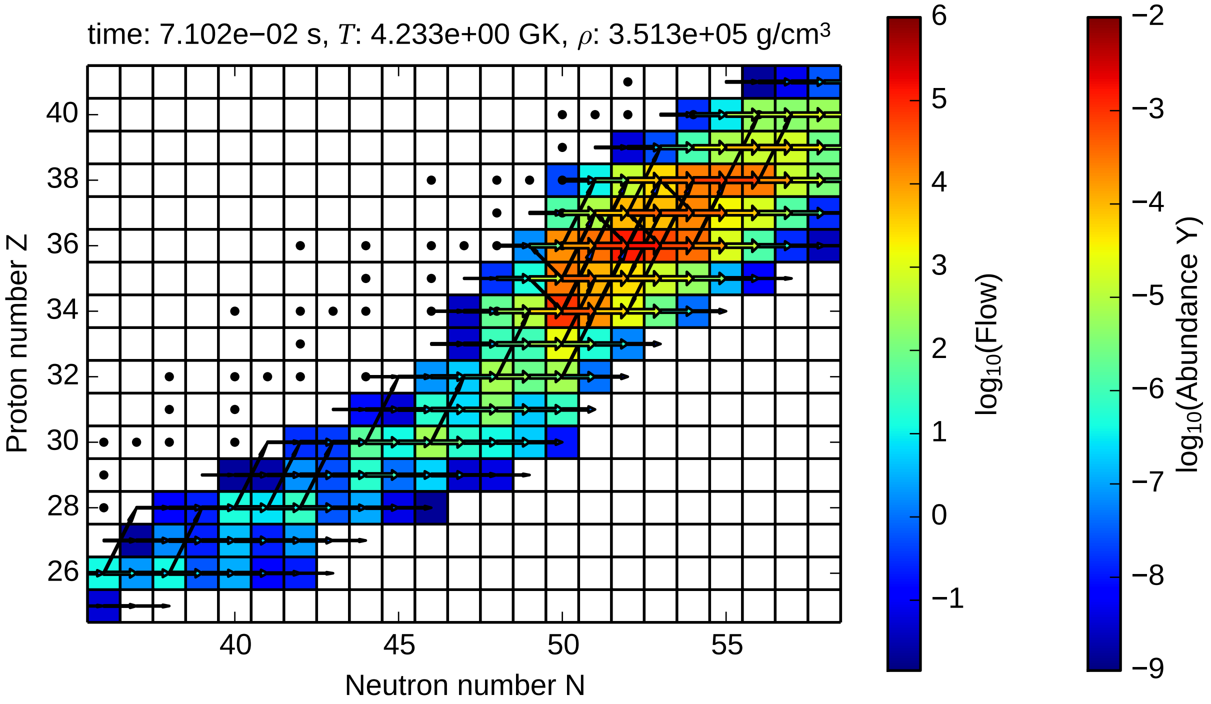

Figure 5.16: Nucleosynthesis evolution at $T \approx 4.2$ GK for the representative trajectory of group MC two without modification of (α,n) reaction rates.

Element	Reaction	r_{corr}
Zn	^{68}Fe$(\alpha,\mathrm{n})^{71}$Ni	-0.74
Se	^{82}Ge$(\alpha,\mathrm{n})^{85}$Se	-0.70
Kr	^{84}Se$(\alpha,\mathrm{n})^{87}$Kr	-0.64
Pd	^{94}Sr$(\alpha,\mathrm{n})^{97}$Zr	$+0.60$
Y	^{85}Br$(\alpha,\mathrm{n})^{88}$Rb	-0.58
Rb	^{84}Se$(\alpha,\mathrm{n})^{87}$Kr	-0.57
Ru	^{94}Sr$(\alpha,\mathrm{n})^{97}$Zr	$+0.57$
Mo	^{94}Sr$(\alpha,\mathrm{n})^{97}$Zr	-0.57
Ga	^{68}Fe$(\alpha,\mathrm{n})^{71}$Ni	-0.56
Ag	^{94}Sr$(\alpha,\mathrm{n})^{97}$Zr	$+0.54$
Zr	^{84}Se$(\alpha,\mathrm{n})^{87}$Kr	$+0.52$
Kr	^{85}Se$(\alpha,\mathrm{n})^{88}$Kr	-0.51
Rb	^{85}Se$(\alpha,\mathrm{n})^{88}$Kr	-0.48
Sr	^{84}Se$(\alpha,\mathrm{n})^{87}$Kr	-0.48
Br	^{81}Ga$(\alpha,\mathrm{n})^{83}$As	-0.47
Co	^{90}Kr$(\alpha,\mathrm{n})^{93}$Sr	-0.45
Fe	^{90}Kr$(\alpha,\mathrm{n})^{93}$Sr	-0.45
Cu	^{90}Kr$(\alpha,\mathrm{n})^{93}$Sr	-0.45
Ni	^{90}Kr$(\alpha,\mathrm{n})^{93}$Sr	-0.44
Sr	^{85}Se$(\alpha,\mathrm{n})^{88}$Kr	-0.43
Ge	^{72}Ni$(\alpha,\mathrm{n})^{75}$Zn	-0.41
Rh	^{94}Sr$(\alpha,\mathrm{n})^{97}$Zr	$+0.38$

Table 5.3: Correlation factors of the Monte Carlo study two.

nuclear physics uncertainties on the nucleosynthesis because the modification of all reaction rates by the same factor can (partially) suppress important reactions. Note that again only an increase of the (α,n) reaction rates leads to significant changes in the abundance pattern. Besides, the scaling factors of 50 and 100 have a similar impact on the abundances.

We have performed another Monte Carlo study with the control trajectory of the group MC two (green dotted line in Fig. 5.9) to verify if the variations in the overall abundance pattern are in general mainly due to the ^{68}Fe(α,n), ^{72}Ni(α,n), ^{81}Ga(α,n), ^{82}Ge(α,n), ^{84,85}Se(α,n), ^{85}Br(α,n), ^{90}Kr(α,n), and ^{94}Sr(α,n) reaction rate uncertainties. The resulting abundance pattern variations from the control Monte Carlo study two are similar to the abundance variations of the reference Monte Carlo study two (Fig. 5.15). The calculated correlation factors for the control Monte Carlo study are given in Tab. 5.4. Comparing the correlation factors of both Monte Carlo studies (see Tabs. 5.3– 5.4), we find that the correlations for $|r_{\mathrm{corr}}| \geq 0.40$ in the reference Monte Carlo study also appear in the control Monte Carlo study. In addition, we find a correlation between the Rh abundance and the change of the ^{94}Sr$(\alpha,\mathrm{n})^{97}$Zr reaction rate in the control Monte Carlo study which is described by $|r_{\mathrm{corr}}| = 0.38$ in the reference Monte Carlo study. However, the most varying elemental abundances are correlated to the same (α,n) reaction rate uncertainties in the reference and in the control Monte Carlo study two.

Despite the larger uncertainties in the Zn and Ga abundances, the reduction of their abundance uncertainties will not contribute much to better understand the formation of lighter heavy elements in neutrino-driven winds, because Zn and Ga can be also produced during the explosive phase of supernovae. Nonetheless, since the conditions of the neutrino-driven wind are similar to those of supernova ejecta exposed to neutrinos, the measurement of the ^{68}Fe(α,n) reaction will improve the understanding of the synthesis of Zn and Ga in supernova in general. As in the Monte Carlo study one, the large variation in the abundances for $Z = 36-38$ are mainly due to the ^{84,85}Se(α,n) reaction rate uncertainties. Therefore, also for the astrophysical conditions investigated here, the measurement of the ^{84,85}Se(α,n) reactions will significantly contribute to better understand the formation of lighter heavy elements in neutron-rich winds.

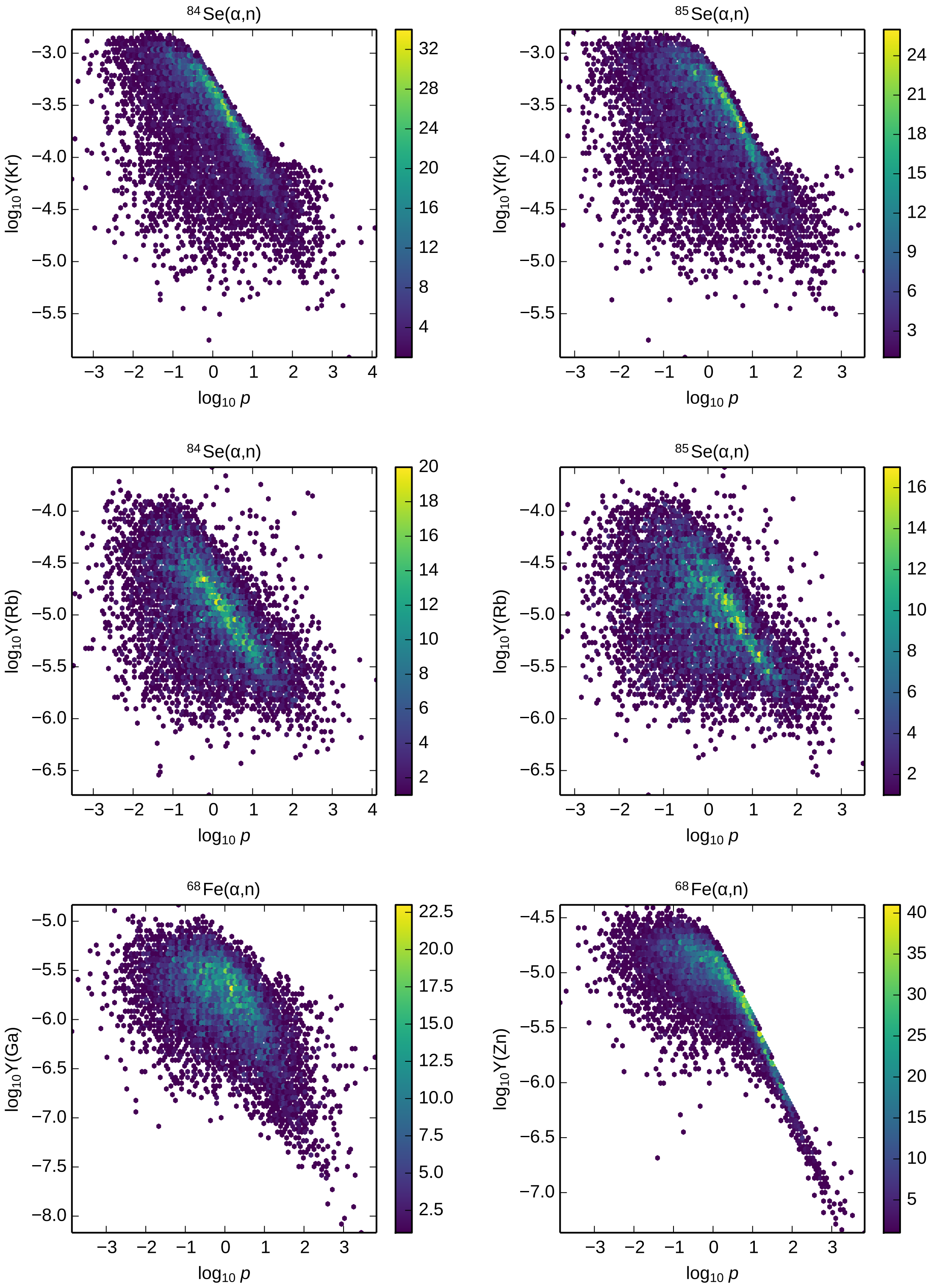

Figure 5.17: First row: Impact of the variation of the $^{84}\mathrm{Se}(\alpha,\mathrm{n})$ (left panel) and $^{85}\mathrm{Se}(\alpha,\mathrm{n})$ (right panel) rates on the Kr abundance. Second row: Change in the Rb abundance due to the modified $^{84}\mathrm{Se}(\alpha,\mathrm{n})$ (left panel) and $^{85}\mathrm{Se}(\alpha,\mathrm{n})$ (right panel) reaction rates. Third row: Influence on the varied $^{68}\mathrm{Fe}(\alpha,\mathrm{n})$ rate on the Ga (left panel) and Zn (right panel) abundances. The Kr, Rb, Ga, and Zn abundances vary the most in the Monte Carlo study two.

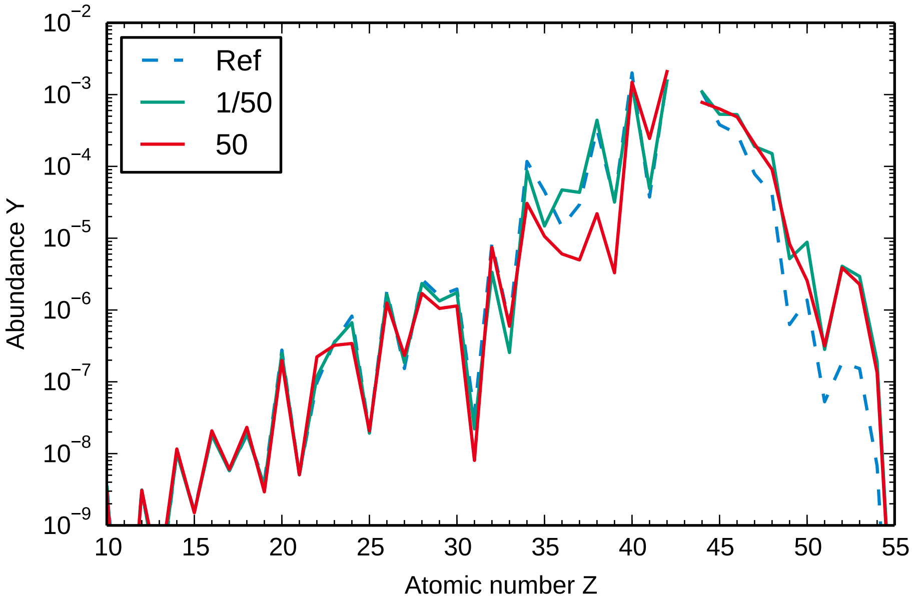

Figure 5.18: Elemental abundances when the $^{68}\mathrm{Fe}(\alpha,\mathrm{n})$, $^{72}\mathrm{Ni}(\alpha,\mathrm{n})$, $^{81}\mathrm{Ga}(\alpha,\mathrm{n})$, $^{82}\mathrm{Ge}(\alpha,\mathrm{n})$, $^{84,85}\mathrm{Se}(\alpha,\mathrm{n})$, $^{85}\mathrm{Br}(\alpha,\mathrm{n})$, $^{90}\mathrm{Kr}(\alpha,\mathrm{n})$, and $^{94}\mathrm{Sr}(\alpha,\mathrm{n})$ are increased and decreased by a factor of 50 up (red) and down (green) using the reference trajectory of group MC two.

Element	Reaction	r_{corr}
Zn	$^{68}\mathrm{Fe}(\alpha,\mathrm{n})^{71}\mathrm{Ni}$	−0.76
Se	$^{82}\mathrm{Ge}(\alpha,\mathrm{n})^{85}\mathrm{Se}$	−0.72
Ga	$^{68}\mathrm{Fe}(\alpha,\mathrm{n})^{71}\mathrm{Ni}$	−0.65
Mo	$^{94}\mathrm{Sr}(\alpha,\mathrm{n})^{97}\mathrm{Zr}$	−0.62
Kr	$^{84}\mathrm{Se}(\alpha,\mathrm{n})^{87}\mathrm{Kr}$	−0.61
Pd	$^{94}\mathrm{Sr}(\alpha,\mathrm{n})^{97}\mathrm{Zr}$	+0.59
Ru	$^{94}\mathrm{Sr}(\alpha,\mathrm{n})^{97}\mathrm{Zr}$	+0.59
Zr	$^{84}\mathrm{Se}(\alpha,\mathrm{n})^{87}\mathrm{Kr}$	+0.55
Kr	$^{85}\mathrm{Se}(\alpha,\mathrm{n})^{88}\mathrm{Kr}$	−0.53
Rh	$^{94}\mathrm{Sr}(\alpha,\mathrm{n})^{97}\mathrm{Zr}$	−0.53
Rb	$^{84}\mathrm{Se}(\alpha,\mathrm{n})^{87}\mathrm{Kr}$	−0.51
Y	$^{85}\mathrm{Br}(\alpha,\mathrm{n})^{88}\mathrm{Rb}$	−0.50
Rb	$^{85}\mathrm{Se}(\alpha,\mathrm{n})^{88}\mathrm{Kr}$	−0.47
Cu	$^{90}\mathrm{Kr}(\alpha,\mathrm{n})^{93}\mathrm{Sr}$	−0.45
Ni	$^{90}\mathrm{Kr}(\alpha,\mathrm{n})^{93}\mathrm{Sr}$	−0.45
Co	$^{90}\mathrm{Kr}(\alpha,\mathrm{n})^{93}\mathrm{Sr}$	−0.45
Ge	$^{72}\mathrm{Ni}(\alpha,\mathrm{n})^{75}\mathrm{Zn}$	−0.45
Fe	$^{90}\mathrm{Kr}(\alpha,\mathrm{n})^{93}\mathrm{Sr}$	−0.44
Ag	$^{94}\mathrm{Sr}(\alpha,\mathrm{n})^{97}\mathrm{Zr}$	+0.44
Sr	$^{85}\mathrm{Se}(\alpha,\mathrm{n})^{88}\mathrm{Kr}$	−0.41
Br	$^{81}\mathrm{Ga}(\alpha,\mathrm{n})^{84}\mathrm{As}$	−0.41
Sr	$^{84}\mathrm{Se}(\alpha,\mathrm{n})^{87}\mathrm{Kr}$	−0.40

Table 5.4: Correlation factors of the control Monte Carlo study two.

5.7 Results of Monte Carlo study three

Figure 5.19 illustrates the resulting abundance pattern variations from the Monte Carlo study using the selected trajectory of group MC three (blue dashed in Fig. 5.9). The (α, n) reaction rate uncertainties strongly affect the abundances for $Z = 28$—35 and for $Z = 47$—48. However, for $36 \leq Z \leq 42$, the variation of the (α, n) reaction rates has only a small effect on the abundances (up to a factor of 10). Our goal is to reduce the nuclear physics uncertainties having an impact on the formation of the lighter heavy elements in the wind nucleosynthesis, and then to put constraints on the astrophysical conditions by combining nucleosynthesis studies with observations of lighter heavy elements in UMP stars (see Sect. 5.3). Therefore, the decrease of the abundance uncertainties for $28 \leq Z \leq 35$ will not help to improve the understanding of neutrino-driven winds. Nonetheless, the elements between Ni and Br can be also synthesized by (α, n) reactions during the explosive phase of core-collapse supernovae.

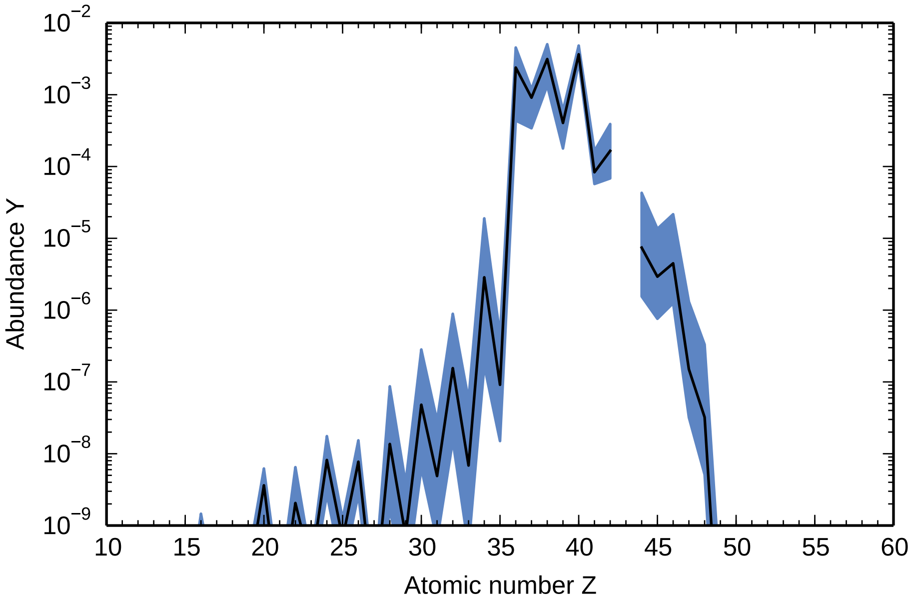

Figure 5.19: Abundance pattern variations from the Monte Carlo study using the representative trajectory of group MC three (dashed blue line in Fig. 5.9).

The nuclear reaction flows at $T \approx 3.7$ GK are illustrated in Fig. 5.20. Note that some of the important (α, n) reactions occur at lower temperatures (i.e., $T \lesssim 2.5$ GK). The computed correlation factors are given in Tab. 5.5. According to the correlation factors, the modification of the $^{64}\mathrm{Fe}(\alpha, \mathrm{n})$ reaction rate leads to changes of the Ni and Cu abundances. An increase of this reaction rate moves matter away from the Fe isotopes which cannot populate Ni and Cu during the decay. The final Zn abundance is influenced in the same way by the variation of the $^{70}\mathrm{Ni}(\alpha, \mathrm{n})$ reaction rate. When the $^{70}\mathrm{Ni}(\alpha, \mathrm{n})$ reaction rate is raised, more material proceeds from the Ni isotopes towards heavier elements, and thus less material decays from the Ni to the Zn isotopes. Although the Ga abundance varies up to a factor of 47, it does not strongly correlate with the variation of any (α, n) reaction rate ($|r_{\mathrm{corr}}| \leq 0.40$). Hence, the variation of the Ga abundance arises from several combined (α, n) reaction rate uncertainties. According to the correlation factor, the change of the Ge abundance is related to the variation of the $^{76}\mathrm{Zn}(\alpha, \mathrm{n})$ reaction rate. As the $^{76}\mathrm{Zn}(\alpha, \mathrm{n})$ reaction rate increases, the Ge abundance decreases (see bottom right panel in Fig. 5.21) since less matter beta decays along the isobaric chain from $^{76}\mathrm{Zn}$ to $^{76}\mathrm{Ge}$. The variation of the As abundance correlates with the change of the $^{73}\mathrm{Cu}(\alpha, \mathrm{n})$ reaction rate (top left panel in Fig. 5.21). However, the As abundance is very low. Note that the reaction $^{73}\mathrm{Cu}(\alpha, \mathrm{n})$ occurs around $T \approx 2.3$ GK. There is a competition between the reactions $^{73}\mathrm{Cu}(\alpha, \mathrm{n})$ and $^{73}\mathrm{Cu}(\mathrm{p}, \mathrm{n})$. The latter reaction shifts material to the zinc isotopes from where it can decay to As. When the $^{73}\mathrm{Cu}(\alpha, \mathrm{n})$ reaction rate is raised, more matter proceeds towards heavier nuclei and does not decay to arsenic. As in the Monte Carlo studies one and two, the modification of the $^{82}\mathrm{Ge}(\alpha, \mathrm{n})$ reaction rate correlates with the change of the Se abundance (top right panel in Fig. 5.21). For the astrophysical conditions investigated here, $^{80}\mathrm{Ge}$ becomes more abundant, and thus the reaction $^{80}\mathrm{Ge}(\alpha, \mathrm{n})$ appears. Since $^{80}\mathrm{Ge}$ and $^{80}\mathrm{Se}$ are linked by beta decays, the variation of the $^{80}\mathrm{Ge}(\alpha, \mathrm{n})$ directly affects the Se abundance (bottom left panel in Fig. 5.21). The Br abundance directly correlates with the modification of the $^{79}\mathrm{Ga}(\alpha, \mathrm{n})$ reaction rate. This reaction

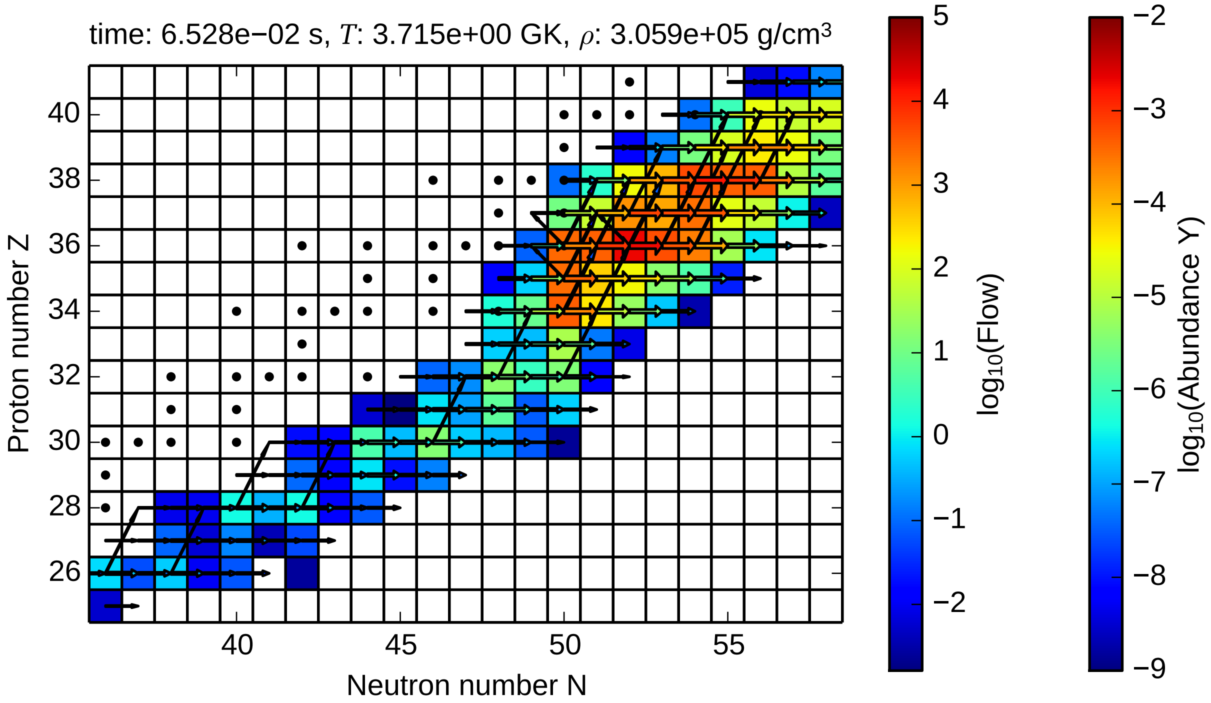

Figure 5.20: Nucleosynthesis evolution at $T \approx 3.7$ GK for the representative trajectory of group MC three without modification of (α, n) reaction rates.

Element	Reaction	r_{corr}
Kr	$^{84}\mathrm{Se}(\alpha,\mathrm{n})^{87}\mathrm{Kr}$	−0.74
Rb	$^{85}\mathrm{Br}(\alpha,\mathrm{n})^{88}\mathrm{Rb}$	−0.73
Sr	$^{84}\mathrm{Se}(\alpha,\mathrm{n})^{87}\mathrm{Kr}$	+0.71
Ge	$^{76}\mathrm{Zn}(\alpha,\mathrm{n})^{79}\mathrm{Ge}$	−0.66
Se	$^{82}\mathrm{Ge}(\alpha,\mathrm{n})^{85}\mathrm{Se}$	−0.65
As	$^{73}\mathrm{Cu}(\alpha,\mathrm{n})^{77}\mathrm{Ga}$	−0.59
Fe	$^{84}\mathrm{Se}(\alpha,\mathrm{n})^{87}\mathrm{Kr}$	−0.59
Ni	$^{64}\mathrm{Fe}(\alpha,\mathrm{n})^{67}\mathrm{Ni}$	−0.59
Br	$^{79}\mathrm{Ga}(\alpha,\mathrm{n})^{82}\mathrm{As}$	−0.49
Zn	$^{70}\mathrm{Ni}(\alpha,\mathrm{n})^{73}\mathrm{Zn}$	−0.47
Kr	$^{85}\mathrm{Se}(\alpha,\mathrm{n})^{88}\mathrm{Kr}$	−0.46
Y	$^{84}\mathrm{Se}(\alpha,\mathrm{n})^{87}\mathrm{Kr}$	+0.45
Ru	$^{94}\mathrm{Sr}(\alpha,\mathrm{n})^{97}\mathrm{Zr}$	+0.42
Sr	$^{85}\mathrm{Se}(\alpha,\mathrm{n})^{88}\mathrm{Kr}$	+0.41
Se	$^{80}\mathrm{Ge}(\alpha,\mathrm{n})^{83}\mathrm{Se}$	−0.41
Cu	$^{64}\mathrm{Fe}(\alpha,\mathrm{n})^{67}\mathrm{Ni}$	−0.41

Table 5.5: Correlation factors of the Monte Carlo study three.

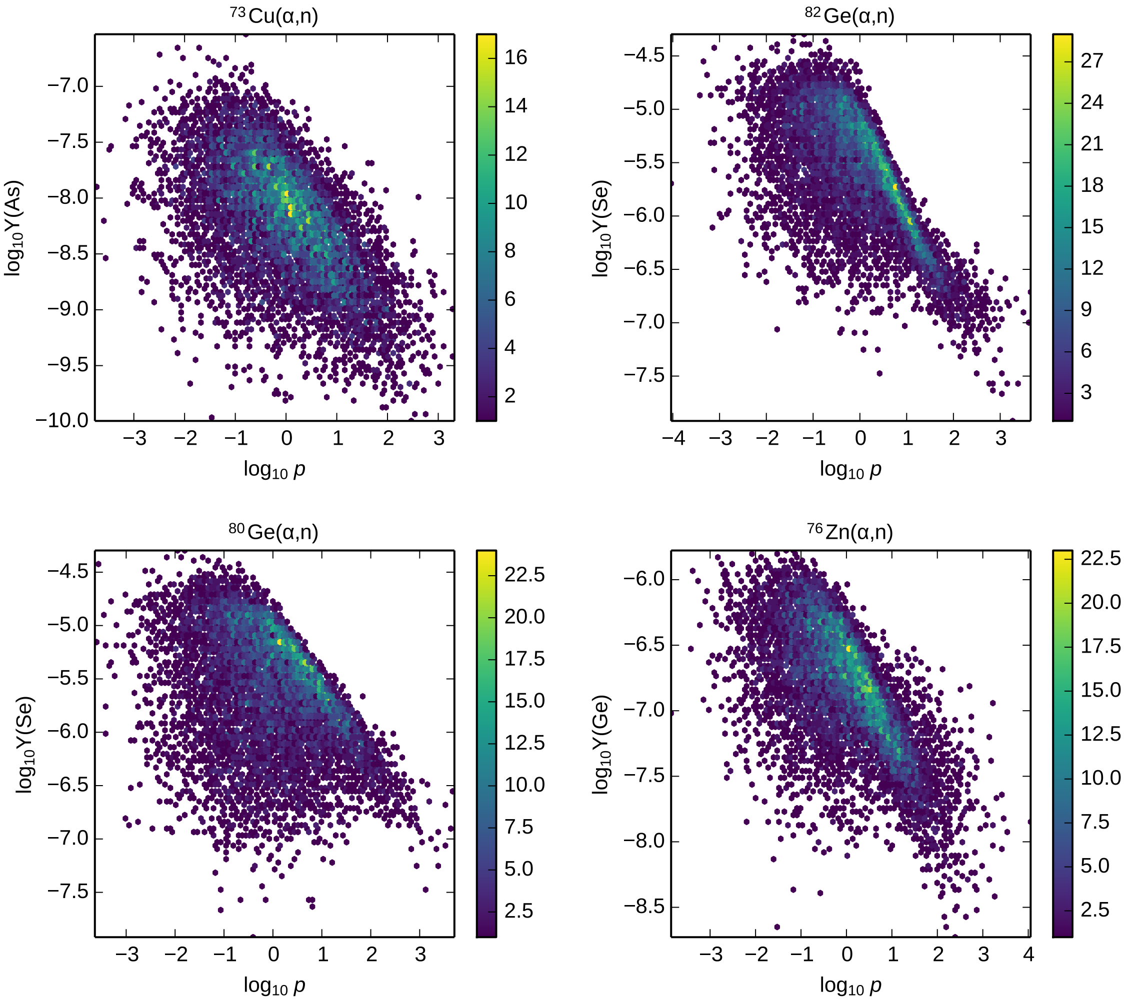

Figure 5.21: Impact of the $^{73}\mathrm{Cu}(\alpha,\mathrm{n})$, $^{82,80}\mathrm{Ge}(\alpha,\mathrm{n})$, $^{76}\mathrm{Zn}(\alpha,\mathrm{n})$ reaction rate variations on the final abundances of As, Se, Ge, respectively. The abundances of these elements vary most (in descending order) in the Monte Carlo study three. The Se abundance correlates stronger with the variation of the $^{82}\mathrm{Ge}(\alpha,\mathrm{n})$ reaction rate.

only appears below $T \approx 2.2$ GK. Note that we have not found a correlation between the $^{79}\mathrm{Ga}(\alpha,\mathrm{n})$ reaction rate uncertainty and changes of the elemental abundances in the Monte Carlo studies one and two.

As we have mentioned before, the (α,n) reaction rate uncertainties do no lead to large variations in the abundances for $Z = 36-42$. The abundance uncertainties of these elements are mainly governed by the variation of the $^{84,85}\mathrm{Se}(\alpha,\mathrm{n})$ and $^{85}\mathrm{Br}(\alpha,\mathrm{n})$ reaction rates (see Tab. 5.5). However, the krypton and strontium abundances strongly correlate with the change of the $^{84}\mathrm{Se}(\alpha,\mathrm{n})$ reaction rate, and the variation of the rubidium abundance is related to the modification of the $^{85}\mathrm{Br}(\alpha,\mathrm{n})$ reaction rate. In the Monte Carlo studies one and two, the uncertainty of the Sr abundance has been also related to the variation of the $^{84}\mathrm{Se}(\alpha,\mathrm{n})$ reaction rate. Besides, in the Monte Carlo study two, the uncertainty in the krypton abundance has been also correlated to the modification of the $^{84}\mathrm{Se}(\alpha,\mathrm{n})$ reaction rate. Nonetheless, the variations of these (α,n) reaction rates have had a larger impact on the abundances for $Z = 36-40$ in the Monte Carlo studies one and two. For the astrophysical conditions investigated here, more matter accumulates at $N = 50$ and the nucleosynthesis path evolve closer to the valley of stability beyond the neutron shell closure. Moreover, for the matter accumulated at $N = 50$, the final abundances are rather given by the Q-values of (α,n) reactions (see Sect. 4.4.3). Since less material exceeds beyond the neutron shell closure, there are less variations of the nucleosynthesis path due to the varied (α,n) reactions, and consequently smaller abundance uncertainties for $Z = 36-42$. According to Tab. 5.5, the change of the $^{94}\mathrm{Sr}(\alpha,\mathrm{n})$ reaction rate correlates with the variation of the ruthenium abundance. As the $^{94}\mathrm{Sr}(\alpha,\mathrm{n})$ reaction rate increases, more material reaches heavier nuclei and thus more matter decays to Ru. The uncertainties in the abundances beyond $Z = 45$ are caused by the alteration of the $^{96}\mathrm{Zr}(\alpha,\mathrm{n})$ reaction rate ($|r_{\mathrm{corr}}| = 0.39$). Note that ^{96}Zr is stable and the $^{96}\mathrm{Zr}(\alpha,\mathrm{n})$ reaction appears for $T \gtrsim 2.5$ GK. The modification of the ^{96}Zr(α, n) reaction rate indirectly changes the abundances for $Z > 43$ in combination with neutron capture reactions and beta decays.

Figure 5.22 displays the elemental abundances when the ^{64}Fe(α, n), ^{70}Ni(α, n), ^{73}Cu(α, n), ^{76}Zn(α, n), ^{79}Ga(α, n), ^{80,82}Ge(α, n), ^{84,85}Se(α, n), ^{85}Br(α, n), ^{88}Kr(α, n), ^{94}Sr(α, n), ^{96}Zr(α, n) reaction rates are varied by a factor of 50 up and down. The comparison between Figs. 5.19 and 5.22 shows that the variation of ^{64}Fe(α, n), ^{70}Ni(α, n), ^{73}Cu(α, n), ^{76}Zn(α, n), ^{79}Ga(α, n), and ^{80,82}Ge(α, n) reaction rates reproduce the abundance uncertainties for $Z < 35$ obtained in the Monte Carlo study. Furthermore, the abundance uncertainties for $Z = 36 - 48$ can be partially explained by the change of the ^{84,85}Se(α, n), ^{85}Br(α, n), ^{88}Kr(α, n), ^{94}Sr(α, n), ^{96}Zr(α, n) reaction rates by a scaling factor of 50. Although the correlation factor indicates a relation between the ^{84}Se(α, n) reaction rate uncertainty and the change of the yttrium abundance, the variation of this rate is not sufficient to explain the Y abundance uncertainty. Note that only the variation of the ^{88}Kr(α, n) reaction rate leads to changes of the Mo abundance ($|r_{\mathrm{corr}}| = 0.37$). However, the Mo abundance only varies by a factor of ~ 6. The uncertainties in the abundances for $Z > 43$ obtained in the Monte Carlo study are a result of several combined reaction rates changes. Nonetheless, the comparison between Figs. 5.19 and 5.22 indicates that the modification of the ^{94}Sr(α, n) and ^{96}Zr(α, n) reaction rates contributes to a large fraction of the abundance uncertainties beyond $Z > 43$.

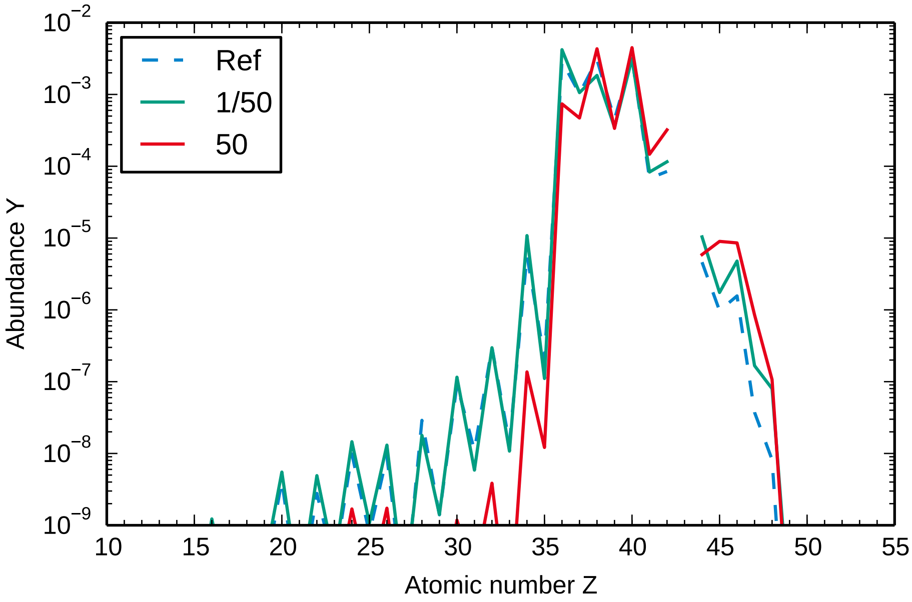

Figure 5.22: Elemental abundances when changing the ^{64}Fe(α, n), ^{70}Ni(α, n), ^{73}Cu(α, n), ^{76}Zn(α, n), ^{79}Ga(α, n), ^{80,82}Ge(α, n), ^{84,85}Se(α, n), ^{85}Br(α, n), ^{88}Kr(α, n), ^{94}Sr(α, n), and ^{96}Zr(α, n) rates by a scaling factor of 50 up (red) and down (green) using the reference trajectory of group MC three.

To verify if the variation of the ^{64}Fe(α, n), ^{70}Ni(α, n), ^{73}Cu(α, n), ^{76}Zn(α, n), ^{79}Ga(α, n), ^{80,82}Ge(α, n), ^{84,85}Se(α, n), ^{85}Br(α, n), ^{88}Kr(α, n), ^{94}Sr(α, n), and ^{96}Zr(α, n) reaction rates in general leads to uncertainties in the abundance pattern for trajectories of group MC three, we have performed a control Monte Carlo study with another trajectory (blue dotted line in Fig. 5.9). The resulting abundance pattern variations from the control Monte Carlo study three are shown in Fig. 5.23. The comparison between Figs. 5.19 and 5.23 shows that the variations in the abundance pattern differ except for the Sr, Y, and Zr abundances. However, the change of the (α, n) reaction rates also has the largest impact on the abundance for $Z = 28 - 35$, only slightly different pronounced than in the reference Monte Carlo study three. Moreover, the influence on the abundances for $Z = 36 - 42$ is also small. The calculated correlation factors are given in Tab. 5.6. Note that the (α, n) reactions having an impact on the abundances for $Z = 28 - 35$ in the reference Monte Carlo study also affect these elemental abundances in the control study. The variations of the krypton and rubidium abundances are also correlated with the ^{84}Se(α, n) and ^{85}Br(α, n) reaction rate uncertainties. In the control study Monte Carlo study three, the Sr and Zr abundance uncertainties are governed by the modification of the ^{88}Kr(α, n) reaction rate, and the Y abundance uncertainty is caused by the change of the ^{85}Br(α, n) reaction rate. Furthermore, we find that the change of the ^{62}Fe(α, n), ^{68}Ni(α, n), ^{74}Zn(α, n), and ^{88}Kr(α, n) reaction rates has an impact on the abundance uncertainties in the control Monte Carlo study three. In addition, the modification of the ^{85}Se(α, n) and the ^{94}Sr(α, n) reaction rates has no influence on the abundance uncertainties in the control Monte Carlo study. The different $Y_{\mathrm{n}}/Y_{\mathrm{seed}}$ and $Y_{\alpha}/Y_{\mathrm{seed}}$ of the selected

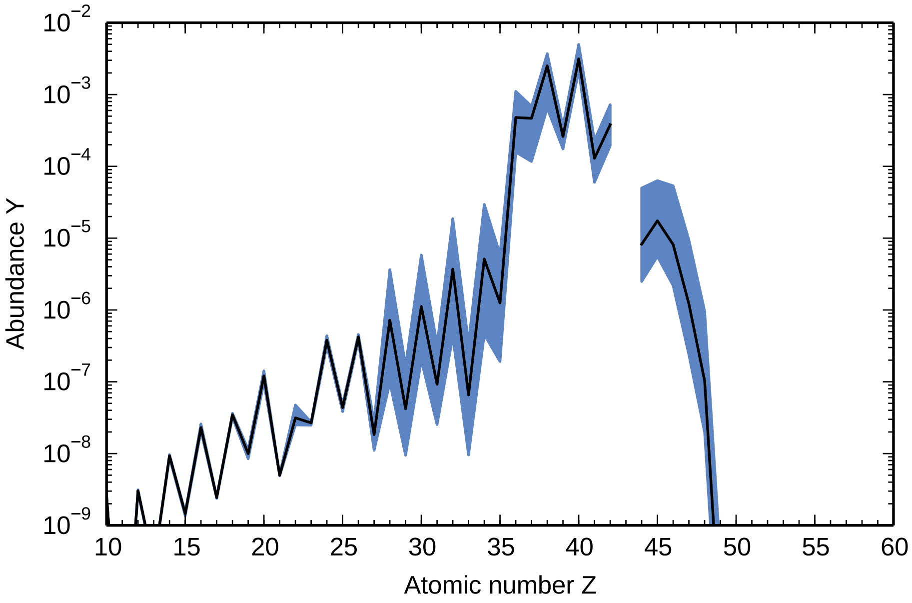

Figure 5.23: Same as Fig. 5.19 for the control trajectory of group MC three (dotted blue line in Fig. 5.9).

Element	Reaction	r_{corr}
Rb	^{85}Br(α, n)^{88}Rb	−0.88
Kr	^{84}Se(α, n)^{87}Kr	−0.79
Ge	^{76}Zn(α, n)^{79}Ge	−0.68
Y	^{85}Br(α, n)^{88}Rb	+0.62
As	^{73}Cu(α, n)^{76}Ga	−0.60
Se	^{82}Ge(α, n)^{85}Se	−0.57
Ni	^{62}Fe(α, n)^{65}Ni	−0.57
Ni	^{64}Fe(α, n)^{67}Ni	−0.57
Br	^{79}Ga(α, n)^{82}As	−0.55
Zn	^{70}Ni(α, n)^{73}Zn	−0.55
Se	^{80}Ge(α, n)^{83}Se	−0.52
Ag	^{96}Zr(α, n)^{99}Mo	+0.52
Nb	^{88}Kr(α, n)^{91}Sr	+0.51
Sr	^{88}Kr(α, n)^{91}Sr	−0.51
Zr	^{88}Kr(α, n)^{91}Sr	+0.50
Zn	^{68}Ni(α, n)^{71}Zn	−0.48
Pd	^{96}Zr(α, n)^{99}Mo	+0.48
Co	^{88}Kr(α, n)^{91}Sr	+0.47
Cd	^{96}Zr(α, n)^{99}Mo	+0.44
Fe	^{88}Kr(α, n)^{91}Sr	−0.44
Ge	^{74}Zn(α, n)^{77}Ge	−0.41

Table 5.6: Correlation factors of the control Monte Carlo study three.

trajectories of the group MC three lead to slightly different nucleosynthesis paths, and thus different or additional (α,n) reactions can occur. Since the (α,n) reactions leading to the largest abundance changes are the same in the reference and control Monte Carlo study three, their reduction will already help to decrease the variations of the abundances due to nuclear physics uncertainties for trajectories of the group MC three. However, the reduction of the $^{64}\mathrm{Fe}(\alpha,\mathrm{n})$, $^{70}\mathrm{Ni}(\alpha,\mathrm{n})$, $^{73}\mathrm{Cu}(\alpha,\mathrm{n})$, $^{76}\mathrm{Zn}(\alpha,\mathrm{n})$, and $^{79}\mathrm{Ga}(\alpha,\mathrm{n})$ rate uncertainties will not put constraints on the astrophysical conditions in neutrino-driven winds. The (α,n) reaction rates which influence the abundances for $Z = 36-42$ are different in the reference and control study, but these reaction rates have been already identified as key rates in the previous Monte Carlo studies (Sects. 5.5–5.6) where they have led to significant changes in the abundance for $Z = 36-39$.

5.8 Comparison of astrophysical and nuclear physics uncertainties with observations of very old stars

After we have performed a Monte Carlo sensitivity study to investigate the impact of the (α,n) reaction rate uncertainties on the abundances in neutron-rich winds using different representative astrophysical conditions (i.e., representative trajectories of the groups MC one, two, three), we compare the resulting abundance uncertainties with observations of very old stars (see Fig. 5.24). We consider the same abundance ratios between pairs of lighter heavy elements as in Sect. 5.3. In Fig. 5.24, the thick lines display the value of the abundance ratio between a given pair of elements A and B using the reference TALYS rates discussed in Sect. 5.2. The thin lines show the ratios of the 2σ abundances of the pairs of elements A and B (i.e., $Y_{+2\sigma}(\mathrm{A})/Y_{+2\sigma}(\mathrm{B})$ and $Y_{-2\sigma}(\mathrm{A})/Y_{-2\sigma}(\mathrm{B})$) obtained in the Monte Carlo studies. Besides, we again compare our results with observations of metal-poor stars with typical r-process robust pattern (CS22892-052 [193]) and with low-enrichment of heavy elements (HD122563 and HD88609 [194]) which are represented by pink and blue stars, respectively. The different colors indicate the different astrophysical conditions and we apply the same color code as in Sects. 5.5–5.7.

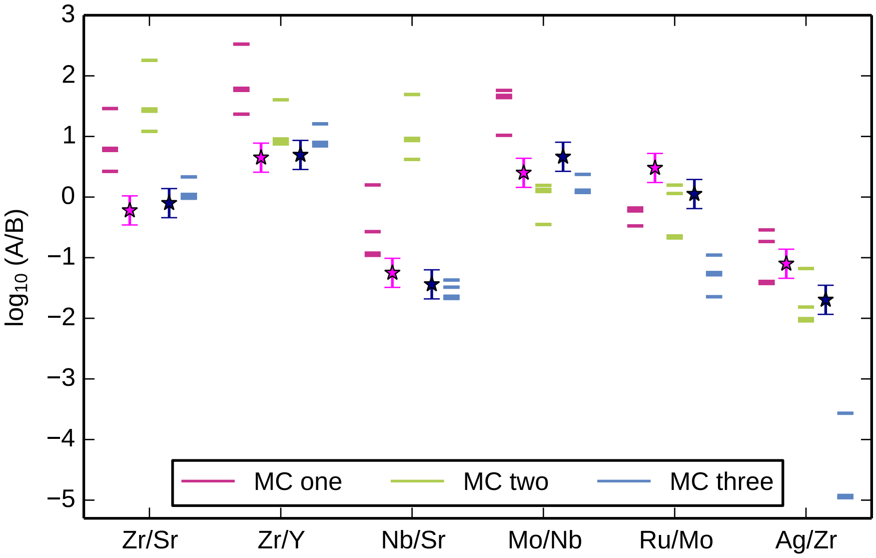

Figure 5.24: Elemental abundance ratios compared to observations from averaged HD122563 and HD88609 (blue stars) and CS22892-052 (pink stars) for the astrophysical conditions MC one, two, three. We apply the same color code for the different astrophysical conditions as in Sects. 5.5–5.7. The horizontal lines indicate the abundance ratio of the given pair of elements A and B: the thicker lines correspond to the reference TALYS rates, whereas the thin lines correspond to the $Y_{+2\sigma}(\mathrm{A})/Y_{+2\sigma}(\mathrm{B})$ and $Y_{-2\sigma}(\mathrm{A})/Y_{-2\sigma}(\mathrm{B})$ ratios obtained in the Monte Carlo studies.

For the astrophysical conditions of group MC one, the large variation of the Zr/Sr, Zr/Y, and Nb/Sr abundance ratios is due to the strongly varying strontium and yttrium abundances. The modification of the (α,n) reaction rates has also a significant impact on the strontium abundance for the astrophysical conditions of group MC two which results in a large spread of the Zr/Sr and Nb/Sr abundance ratios. The variation of the Sr abundance in the Monte Carlo study two is not as strongly pronounced as in the Monte Carlo study one, but since we are comparing abundance ratios this is not visible in Fig. 5.24. For the astrophysical conditions of group MC three, the (α,n) reaction rate uncertainties only slightly influence the abundances for $Z = 36-42$, and thus the abundance ratios selected here do not vary much. The relatively large variation of the Ag/Zr abundance ratio is due to the small and strongly varying Ag abundance. Note that the reference Ag/Zr abundance ratio overlaps with the $Y_{+2\sigma}(\mathrm{Ag})/Y_{+2\sigma}(\mathrm{Zr})$ ratio. Compared to Fig. 5.7, where various astrophysical conditions have been given by different Y_e and all (α, n) reaction rates have been varied by the same factor, the variation of the abundance ratios resulting from the Monte Carlo studies is larger. However, none of the considered astrophysical conditions can reproduce the trend from Zr/Sr through Ag/Zr taking into account the nuclear physics uncertainties.

Figure 5.24 clearly indicates that for the astrophysical conditions investigated here, the influence of the (α, n) reaction rate uncertainties on the abundances can become critical when comparing to the observations of very old stars. Therefore, it is critical to reduce the uncertainties of the identified key (α, n) reactions before we can make full use of the observations and combine them with nucleosynthesis studies to put constraints on the astrophysical conditions in neutrino-driven winds and core-collapse supernovae.

6 Summary and outlook

Neutrino-driven winds from nascent neutron stars are an exciting astrophysical site for the formation of the lighter heavy elements between Sr up to (possibly) Ag. Observations of very old stars (i.e., ultra metal-poor stars) indicate that the formation of the lighter heavy elements in the early universe is related to the r-process and at least one additional process [23, 88]. Although it is not clear if neutrino-driven winds are neutron- [126–128] or proton-rich [38, 39], or a combination of both [123], the required astrophysical conditions to synthesize lighter heavy elements are found in current supernova simulations [40, 41]. In this thesis, we assumed that these elements are produced in slightly neutron-rich winds by the weak r-process. Despite the fast progress in the last years, the astrophysics and nuclear physics uncertainties are still large [208]. Therefore, the goal of this thesis was to study the impact of astrophysical and nuclear physics uncertainties on the wind nucleosynthesis.

In the first part of this thesis, we performed a systematic study to quantify the astrophysical uncertainties in neutron-rich winds. Since a systematic study with trajectories from hydrodynamic simulations is computationally very expensive, we used steady-state wind trajectories. The neutrino-driven wind can be assumed to be a steady-state outflow [34] because the neutrino luminosities and energies as well as the neutron star mass and radius change only slowly during the Kelvin-Helmholtz cooling time scale. The structure and characteristics of the neutrino-driven wind depend on the mass and radius of the neutron star and the energies and luminosties of the neutrinos. Therefore, to cover all possible wind conditions, we varied these quantities within the entire relevant parameter space and calculated the corresponding steady-state wind trajectories.

We performed nucleosynthesis calculations for all steady-state trajectories. In the final abundances, we distinguished between four nucleosynthesis groups (NSE1, NSE2, CPR1, CPR2) which were identified by the $Y_\mathrm{n}/Y_\mathrm{seed}$ and the Y_α/Y_seed at $T = 3$ GK. These groups differ in the evolution of the nucleosynthesis path relative to the valley of stability. Each nucleosynthesis group shows characteristic abundance peaks. We showed that within the groups NSE1, NSE2, CPR1 the nucleosynthesis evolution is similar and therefore results in similar final abundances. For none of these three groups, the nucleosynthesis path overcomes the neutron shell closure $N = 50$ and thus matter accumulates there. Hence, heavier elements than Zr are not synthesized. The final abundances of the groups NSE1 and NSE2 are mainly synthesized during NSE. Therefore, the abundances are rather determined by binding energies and partition functions and do not depend on specific reactions. For stable nuclei and particularly for unstable nuclei, binding energies and partition functions are better known than reaction rates [150]. The conditions of group CPR1 are slightly more neutron- and alpha-rich compared to the groups NSE1 and NSE2. Nonetheless, the $Y_\mathrm{n}/Y_\mathrm{seed}$ and the Y_α/Y_seed are not large enough to exceed the production of nuclei with $N = 50$. Thus, the final abundances are rather given by Q-values of (α,n) reactions (see also Refs. [33, 40, 186]). For nuclei close to stability, where most of the masses have been measured by experiments, the Q-values are relatively well known. Consequently, as for the groups NSE1 and NSE2, nuclear physics uncertainties will not have a large impact on the abundance patterns.

Only for the conditions of group CPR2, the nucleosynthesis path proceeds beyond $N = 50$. The larger $Y_\mathrm{n}/Y_\mathrm{seed}$ and Y_α/Y_seed result in a nucleosynthesis evolution further away from the valley of stability. The nucleosynthesis path reaches $N = 50$ at lower atomic numbers where the Q-values of (α,n) reactions are close to zero. Therefore, the path exceeds the neutron shell closure by (α,n) reactions. For the nucleosynthesis group CPR2, the final abundances are very sensitive to the $Y_\mathrm{n}/Y_\mathrm{seed}$ and the Y_α/Y_seed. Small variations of these quantities lead to different abundance patterns and also the heaviest synthesized elements change. The final abundances are very sensitive to individual critical reactions, especially charged particle reactions.

Based on the relation between the electron fraction, the entropy, and the expansion time scale derived from Ref. [111], we gave an overview of which combinations of these wind parameters lead to the nucleosynthesis patterns NSE1, NSE2, CPR1, or CPR2. This overview will be very useful for hydrodynamic simulations (where the electron fraction, the entropy, and the expansion time scale are known) because it qualitatively predicts the nucleosynthesis evolution and final abundance pattern without running post-processing nucleosynthesis calculations. We identified that the nucleosynthesis groups NSE1 and NSE2 only occur for $Y_\mathrm{e} < 0.45$ and $Y_\mathrm{e} > 0.45$, respectively. Both groups occur for low entropies and/or long expansion time scales. For increasing entropies and/or decreasing expansion time scales, we found the nucleosynthesis group CPR1. This group is the transition from the patterns NSE1 and NSE2 to the pattern CPR2. For larger electron fractions, the group CPR2 occurs at higher entropies and/or shorter expansion time scales.

We also illustrated which combinations of Y_e, $Y_\mathrm{n}/Y_\mathrm{seed}$, and Y_α/Y_seed result in the nucleosynthesis groups NSE1, NSE2, CPR1, or CPR2. Furthermore, we indicated which combinations of Y_e, $Y_\mathrm{n}/Y_\mathrm{seed}$, and Y_α/Y_seed are required to synthesize elements beyond the second or third r-process peak. We found that for a sufficient amount of Y_α/Y_seed the nucleosynthesis only depends on the $Y_\mathrm{n}/Y_\mathrm{seed}$. Moreover, we showed which Y_e, $Y_\mathrm{n}/Y_\mathrm{seed}$, and Y_α/Y_seed lead to the abundance patterns from neutrino-driven winds of neutron star mergers with $Y_\mathrm{e} = 0.25 - 0.40$ and $S = 14 - 27$ $\mathrm{k_B/nuc}$ [187].

In the first part of the thesis, we obtained a comprehensive picture of the possible nucleosynthesis in neutron-rich winds. Since the conditions of the neutrino-driven wind are similar to those of supernova ejecta exposed to neutrinos, our conclusions can be extended to supernova ejecta in general and they are complementary to post-processing studies based on simulations.

In the second part of the thesis, we investigated the impact of nuclear physics uncertainties due to (α,n) reactions on the nucleosynthesis in neutron-rich winds. We described in detail the nucleosynthesis evolution in the weak r-process based on the nuclear reaction flows and the averaged expansion time scales of the contributing reactions. For slightly neutron-rich winds, the nucleosynthesis path evolves close to the valley of stability where (α,n) reactions are faster than beta decays. Therefore, (α,n) reactions are crucial to redistribute matter and reach heavier nuclei in slightly neutron-rich winds. However, none of the relevant (α,n) reactions has been measured in the energy (temperature) range relevant for the weak r-process. All (α,n) reaction rates entering in our nucleosynthesis calculations are calculated with the statistical Hauser-Feshbach model. We estimated the uncertainty of the theoretical (α,n) reaction rates based on previous studies of Refs. [48, 162]. According to these studies, the main uncertainty in the theoretical (α,n) reaction rates arises from the different alpha optical potentials for the temperatures relevant for the weak r-process. Besides, we compared theoretical (α,n) calculations with few available measurements of stable nuclei at temperatures above the weak r-process regime. We concluded that the reliability of the theoretical (α,n) reaction rates is not better than a factor of 10.

In a first sensitivity study, we investigated the impact of the (α,n) reactions on the abundances by varying all (α,n) reaction rates between Fe and Rh by factors of 5, 10, and 50 up and down using a trajectory ejected 9 s after bounce from a hydrodynamic simulation of Ref. [36]. To study the influence of (α,n) reaction rates for different astrophysical conditions, we varied the electron fraction. This does not cover all possible astrophysical conditions but allows to consider the impact of (α,n) reactions for different nucleosynthesis evolutions. Our results clearly showed that (α,n) reaction rates have an impact on the nucleosynthesis. When the (α,n) reaction rates are increased, the abundances are larger for $Z > 38$ compared to the case where no (α,n) rates are varied. On the other hand, when the (α,n) rates are reduced, less matter moves towards heavier nuclei and the abundances below Sr are larger. We found similar results for different Y_e (i.e., nucleosynthesis paths), only for $Y_\mathrm{e} = 0.49$ the (α,n) reactions have no significant impact on the abundances. Moreover, we emphasized the importance of reducing astrophysical and nuclear physics uncertainties by comparing abundance ratios from observations and nucleosynthesis calculations including astrophysical uncertainties due to different Y_e and nuclear physics uncertainties due to varied (α,n) reaction rates.

The variation of a set of reaction rates gives an overview if the rate uncertainties have an impact on the nucleosynthesis. Since the change of the reaction rates by the same factors can (partially) suppress important reactions or point out to not so relevant reactions, this method is not recommended to identify key reactions. Therefore, we performed a Monte Carlo sensitivity study by independently varying each (α,n) reaction rate between Fe and Rh by a random factor. The rate variation factors followed a lognormal distribution to avoid unphysical, negative reaction rates. The parameters of the lognormal distribution were chosen in such a way that the rate factors describe the (α,n) reaction rate uncertainties. To select representative wind conditions for the Monte Carlo sensitivity study, we referred to the comprehensive study of the possible astrophysical conditions in neutron-rich winds. This study showed that nuclear physics uncertainties only affect the nucleosynthesis for the conditions of group CPR2. We identified three typical Kr-Rb-Sr-Y-Zr patterns in the final CPR2 abundances and performed a Monte Carlo study (Monte Carlo one, Monte Carlo two, Monte Carlo three) for a representative trajectory of each of the three abundance patterns. Since the abundance patterns of the same group can vary for $Z < 36$ and $Z > 40$, we performed a control Monte Carlo study with another trajectory for each group. In the Monte Carlo studies one and two, the variation of the (α,n) reaction rates had a significant impact on the abundances between $Z = 36 - 39$. This can be very important when comparing calculated abundances to observations. In the Monte Carlo study three, the modification of the (α,n) reaction rates rather influenced the abundances for $Z = 28 - 35$ which can be relevant for explosive nucleosynthesis calculations. The key (α,n) reactions, having a strong impact on the nucleosynthesis, were identified by inspecting large abundance changes and analyzing the correlations between reaction rate variations and resulting abundance changes in the 10000 Monte Carlo runs. Since the relations between the reaction rate variations and the abundance changes are frequently non-linear [204], we used the Spearman rank-order coefficient which quantifies how well the relation is described by a monotonic function. We found that in the Monte Carlo studies (one, two, and three) the (α, n) reactions contributing to the largest abundance changes are the same for both selected trajectories. Moreover, we showed that the ^{82}Ge(α, n), ^{84}Se(α, n), and ^{85}Se(α, n) reaction rate uncertainties have a significant impact on the elemental abundances for $Z = 36-39$ for some astrophysical conditions. The reduction of the reaction rate uncertainties would significantly decrease the influence of nuclear physics uncertainties on the nucleosynthesis of lighter heavy elements in neutron-rich winds.

Once the uncertainties in the (α, n) reaction rates are reduced by experiments, nucleosynthesis studies within the astrophysical uncertainties combined with observations of ultra metal-poor stars will put constraints on the wind conditions. Therefore, the results presented in this thesis will contribute to better understand the nucleosynthesis in neutrino-driven winds and core-collapse supernovae. We are close to understand the formation of lighter heavy elements in neutrino-driven winds. The necessary wind conditions to synthesize them are found in current supernova simulations. Since the nuclei involved in the wind nucleosynthesis are close to stability, the relevant unmeasured experimental data will be accessible with new radioactive beam facilities like FRIB and FAIR in the near future. At the present time, observations of UMP stars are very rare but there will be more high resolution detections with large-scale surveys and new telescopes in the future [49, 50]. All this progress combined with nucleosynthesis studies will explain the formation of lighter heavy elements in core-collapse supernovae.

Bibliography

[1] E. M. Burbidge, G. R. Burbidge, W. A. Fowler, and F. Hoyle, Rev. Mod. Phys. **29**, 547 (1957).

[2] A. G. W. Cameron, Publ. Astron. Soc. Pac. **69**, 201 (1957).

[3] S. Goriely, A. Bauswein, and H.-T. Janka, Astrophys. J. Lett. **738**, L32 (2011).

[4] O. Korobkin, S. Rosswog, A. Arcones, and C. Winteler, Mon. Not. R. Astron. Soc. **426**, 1940 (2012).

[5] S. Wanajo, Y. Sekiguchi, N. Nishimura, K. Kiuchi, K. Kyutoku, and M. Shibata, Astrophys. J. Lett. **789**, L39 (2014).

[6] A. P. Ji, A. Frebel, A. Chiti, and J. D. Simon, Nature **531**, 610 (2016).

[7] N. Nishimura, T. Takiwaki, and F.-K. Thielemann, Astrophys. J. **810**, 109 (2015).

[8] C. Arlandini, F. Käppeler, K. Wisshak, R. Gallino, M. Lugaro, M. Busso, and O. Straniero, Astrophys. J. **525**, 886 (1999).

[9] R. Gallino, C. Arlandini, M. Busso, M. Lugaro, C. Travaglio, O. Straniero, A. Chieffi, and M. Limongi, Astrophys. J. **497**, 388 (1998).

[10] O. Straniero, R. Gallino, M. Busso, A. Chiefei, C. M. Raiteri, M. Limongi, and M. Salaris, Astrophys. J. Lett. **440**, L85 (1995).

[11] M. Limongi, O. Straniero, and A. Chieffi, Astrophys. J. Suppl. Ser. **129**, 625 (2000).

[12] C. M. Raiteri, M. Busso, G. Picchio, and R. Gallino, Astrophys. J. **371**, 665 (1991).

[13] C. M. Raiteri, R. Gallino, M. Busso, D. Neuberger, and F. Käppeler, Astrophys. J. **419**, 207 (1993).

[14] M. Pignatari, K. Göbel, R. Reifarth, and C. Travaglio, Int. J. Mod. Phys. E **25**, 1630003-232 (2016).

[15] C. Sneden, J. J. Cowan, and R. Gallino, Annu. Rev. Astron. & Astrophys. **46**, 241 (2008).

[16] G. J. Wasserburg, and Y.-Z. Qian, Astrophys. J. Lett. **529**, L21 (2000).

[17] Y.-Z. Qian, and G. J. Wasserburg, Phys. Rep. **333**, 77 (2000).

[18] Y.-Z. Qian, and G. J. Wasserburg, Astrophys. J. **559**, 925 (2001).

[19] E. Depagne *et al.*, Astron. Astrophys. **390**, 187 (2002).

[20] Y.-Z. Qian, and G. J. Wasserburg, Astrophys. J. **567**, 515 (2002).

[21] Y.-Z. Qian, W. L. W. Sargent, and G. J. Wasserburg, Astrophys. J. Lett. **569**, L61 (2002).

[22] J. A. Johnson, and M. Bolte, Astrophys. J. **579**, 616 (2002).

[23] Y. Qian, and G. J. Wasserburg, Phys. Rep. **442**, 237 (2007).

[24] C. J. Hansen, F. Montes, and A. Arcones, Astrophys. J. **797**, 123 (2014).

[25] C. Travaglio, R. Gallino, E. Arnone, J. J. Cowan, F. Jordan, and C. Sneden, Astrophys. J. **601**, 864 (2004).

[26] F. Montes *et al.*, Astrophys. J. **671**, 1685 (2007).

[27] U. Frischknecht, R. Hirschi, and F.-K. Thielemann, Astron. Astrophys. **538**, L2 (2012).

[28] S. E. Woosley, and R. D. Hoffman, Astrophys. J. **395**, 202 (1992).

[29] C. Freiburghaus, J.-F. Rembges, T. Rauscher, E. Kolbe, F.-K. Thielemann, K.-L. Kratz, B. Pfeiffer, and J. J. Cowan, Astrophys. J. **516**, 381 (1999).

[30] J. W. Truran, and J. J. Cowan, in *Nuclear Astrophysics, 2000*, edited by W. Hillebrandt & E. Müller (2000).

[31] C. Fröhlich, G. Martínez-Pinedo, M. Liebendörfer, F.-K. Thielemann, E. Bravo, W. R. Hix, K. Langanke, and N. T. Zinner, Phys. Rev. Lett. **96**, 142502 (2006).

[32] J. Pruet, R. D. Hoffman, S. E. Woosley, H.-T. Janka, and R. Buras, Astrophys. J. **644**, 1028 (2006).

[33] S. Wanajo, Astrophys. J. **647**, 1323 (2006).

[34] R. C. Duncan, S. L. Shapiro, and I. Wasserman, Astrophys. J. **309**, 141 (1986).

[35] S. E. Woosley, J. R. Wilson, G. J. Mathews, R. D. Hoffman, and B. S. Meyer, Astrophys. J. **433**, 229 (1994).

[36] A. Arcones, H.-T. Janka, and L. Scheck, Astron. Astrophys. **467**, 1227 (2007).

[37] A. Arcones, and H.-T. Janka, Astron. Astrophys. **526**, A160 (2011).

[38] L. Hüdepohl, B. Müller, H. Janka, A. Marek, and G. G. Raffelt, Phys. Rev. Lett. **104**, 251101 (2010).

[39] T. Fischer, S. C. Whitehouse, A. Mezzacappa, F.-K. Thielemann, and M. Liebendörfer, Astron. Astrophys. **517**, A80 (2010), 0908.1871.

[40] S. Wanajo, B. Müller, H.-T. Janka, and A. Heger, Astrophys. J. **852**, 40 (2018).

[41] J. A. Harris, W. R. Hix, M. A. Chertkow, C. T. Lee, E. J. Lentz, and O. E. B. Messer, Astrophys. J. **843**, 2 (2017).

[42] H.-T. Janka, Annu. Rev. Nucl. Part. Sc. **62**, 407 (2012).

[43] A. Burrows, Rev. Mod. Phys. **85**, 245 (2013).

[44] C. D. Ott, Computing in Science & Engineering **18**, 78 (2016).

[45] A. Arcones, and F.-K. Thielemann, J. Phys. G: Nucl. Phys. **40**, 013201 (2013).

[46] W. Hauser, and H. Feshbach, Phys. Rev. **87**, 366 (1952).

[47] M. Beard, E. Uberseder, R. Crowter, and M. Wiescher, Phys. Rev. C **90**, 034619 (2014).

[48] J. Pereira, and F. Montes, Phys. Rev. C **93**, 034611 (2016).

[49] P. S. Barklem, N. Christlieb, T. C. Beers, V. Hill, M. S. Bessell, J. Holmberg, B. Marsteller, S. Rossi, F.-J. Zickgraf, and D. Reimers, Astron. Astrophys. **439**, 129 (2005).

[50] H. Aihara *et al.*, Astrophys. J. Suppl. Ser. **193**, 29 (2011).

[51] C. Iliadis, *Nuclear Physics of Stars* (Wiley-VCH, 2007).

[52] A. Frebel, and J. E. Norris, “Metal-Poor Stars and the Chemical Enrichment of the Universe,” in *Planets, Stars and Stellar Systems. Volume 5: Galactic Structure and Stellar Populations*, edited by T. D. Oswalt, and G. Gilmore (2013) p. 55.

[53] H.-T. Janka, K. Langanke, A. Marek, G. Martínez-Pinedo, and B. Müller, Phys. Rep. **442**, 38 (2007).

[54] H.-T. Janka, *Supernovae und kosmische Gammablitze: Ursachen und Folgen von Sternexplosionen* (Spektrum Akademischer Verlag, 2011).

[55] Y.-Z. Qian, and S. E. Woosley, Astrophys. J. **471**, 331 (1996).

[56] R. H. Cyburt, B. D. Fields, K. A. Olive, and T.-H. Yeh, Rev. Mod. Phys. **88**, 015004 (2016).

[57] R. Kippenhahn, A. Weigert, and A. Weiss, *Stellar Structure and Evolution* (Springer Berlin Heidelberg, 2012).

[58] S. E. Woosley, A. Heger, and T. A. Weaver, Rev. Mod. Phys. **74**, 1015 (2002).

[59] D. Arnett, *Supernovae and Nucleosynthesis* (Princeton University Press, 1996).

[60] N. Grevesse, and A. J. Sauval, Space Sci. Rev. **85**, 161 (1998).

[61] C. Mihos, *Late Stage Nuclear Burning in High Mass Stars*, `http://burro.astr.cwru.edu/Academics/Astr221/LifeCycle/highmassburn.html`.

[62] K. Lodders, Astrophys. J. **591**, 1220 (2003).

[63] H. Schatz, J. Phys. G: Nucl. Phys. **43**, 064001 (2016).

[64] M. Busso, R. Gallino, and G. J. Wasserburg, Annu. Rev. Astron. & Astrophys. **37**, 239 (1999).

[65] F. Käppeler, R. Gallino, S. Bisterzo, and W. Aoki, Rev. Mod. Phys. **83**, 157 (2011).

[66] K.-L. Kratz, K. Farouqi, B. Pfeiffer, J. W. Truran, C. Sneden, and J. J. Cowan, Astrophys. J. **662**, 39 (2007).

[67] I. V. Panov, E. Kolbe, B. Pfeiffer, T. Rauscher, K.-L. Kratz, and F.-K. Thielemann, Nucl. Phys. A **747**, 633 (2005).

[68] S. Goriely, J.-L. Sida, J.-F. Lemaître, S. Panebianco, N. Dubray, S. Hilaire, A. Bauswein, and H.-T. Janka, Phys. Rev. Lett. **111**, 242502 (2013).

[69] J. J. Cowan, F.-K. Thielemann, and J. W. Truran, Phys. Rep. **208**, 267 (1991).

[70] M. Arnould, S. Goriely, and K. Takahashi, Phys. Rep. **450**, 97 (2007).

[71] K. Farouqi, K.-L. Kratz, B. Pfeiffer, T. Rauscher, F.-K. Thielemann, and J. W. Truran, Astrophys. J. **712**, 1359 (2010).

[72] M. Arnould, and S. Goriely, Phys. Rep. **384**, 1 (2003).

[73] T. Rauscher, N. Dauphas, I. Dillmann, C. Fröhlich, Z. Fülöp, and G. Gyürky, Rep. Prog. Phys. **76**, 066201 (2013).

[74] B. S. Meyer, G. J. Mathews, W. M. Howard, S. E. Woosley, and R. D. Hoffman, Astrophys. J. **399**, 656 (1992).

[75] A. Parikh, J. José, G. Sala, and C. Iliadis, Prog. Part. Nucl. Phys. **69**, 225 (2013).

[76] H. Schatz *et al.*, Phys. Rep. **294**, 167–263 (1998).

[77] H. Schatz, A. Aprahamian, V. Barnard, L. Bildsten, A. Cumming, M. Ouellette, T. Rauscher, F.-K. Thielemann, and M. Wiescher, Phys. Rev. Lett. **86**, 3471 (2001).

[78] J. J. Cowan, and W. K. Rose, Astrophys. J. **212**, 149 (1977).

[79] M. Hampel, R. J. Stancliffe, M. Lugaro, and B. S. Meyer, Astrophys. J. **831**, 171 (2016).

[80] S. Jones, C. Ritter, F. Herwig, C. Fryer, M. Pignatari, M. G. Bertolli, and B. Paxton, Mon. Not. R. Astron. Soc. **455**, 3848 (2016).

[81] C. Sneden *et al.*, Astrophys. J. **591**, 936 (2003).

[82] J. Westin, C. Sneden, B. Gustafsson, and J. J. Cowan, Astrophys. J. **530**, 783 (2000).

[83] J. J. Cowan *et al.*, Astrophys. J. **572**, 861 (2002).

[84] V. Hill *et al.*, Astron. Astrophys. **387**, 560 (2002).

[85] I. I. Ivans, J. Simmerer, C. Sneden, J. E. Lawler, J. J. Cowan, R. Gallino, and S. Bisterzo, Astrophys. J. **645**, 613 (2006).

[86] A. Frebel, N. Christlieb, J. E. Norris, C. Thom, T. C. Beers, and J. Rhee, Astrophys. J. Lett. **660**, L117 (2007).

[87] J. Simmerer, C. Sneden, J. J. Cowan, J. Collier, V. M. Woolf, and J. E. Lawler, Astrophys. J. **617**, 1091 (2004).

[88] Y.-Z. Qian, and G. J. Wasserburg, Astrophys. J. **687**, 272 (2008).

[89] S. Cristallo, C. Abia, O. Straniero, and L. Piersanti, Astrophys. J. **801**, 53 (2015).

[90] M. Reichert, *Reduced nuclear reaction network for hydrodynamical simulations*, Master's thesis, TU Darmstadt (2016).

[91] M. Ugliano, H.-T. Janka, A. Marek, and A. Arcones, Astrophys. J. **757**, 69 (2012).

[92] T. Ertl, M. Ugliano, H.-T. Janka, A. Marek, and A. Arcones, Astrophys. J. **821**, 69 (2016).

[93] T. Ertl, H.-T. Janka, S. E. Woosley, T. Sukhbold, and M. Ugliano, Astrophys. J. **818**, 124 (2016).

[94] S. W. Bruenn, and W. C. Haxton, Astrophys. J. **376**, 678 (1991).

[95] H. A. Bethe, Rev. Mod. Phys. **62**, 801 (1990).

[96] W. Hillebrandt, T. Kodama, and K. Takahashi, Astron. Astrophys. **52**, 63 (1976).

[97] J. R. Wilson, and R. W. Mayle, Phys. Rep. **227**, 97 (1993).

[98] A. Burrows, Annu. Rev. Nucl. Part. Sc. **40**, 181 (1990).

[99] H. A. Bethe, and J. R. Wilson, Astrophys. J. **295**, 14 (1985).

[100] S. Yamada, H.-T. Janka, and H. Suzuki, Astron. Astrophys. **344**, 533 (1999).

[101] C. Y. Cardall, and G. M. Fuller, Astrophys. J. Lett. **486**, L111 (1997).

[102] K. Otsuki, H. Tagoshi, T. Kajino, and S. Wanajo, Astrophys. J. **533**, 424 (2000).

[103] T. A. Thompson, A. Burrows, and B. S. Meyer, Astrophys. J. **562**, 887 (2001).

[104] S. Wanajo, T. Kajino, G. J. Mathews, and K. Otsuki, Astrophys. J. **554**, 578 (2001).

[105] S. L. Shapiro, and S. A. Teukolsky, *Black Holes, White Dwarfs, and Neutron Stars* (New York: Wiley, 1983).

[106] H. A. Bethe, Astrophys. J. **412**, 192 (1993).

[107] H. A. Bethe, J. H. Applegate, and G. E. Brown, Astrophys. J. **241**, 343 (1980).

[108] A. Arcones, G. Martínez-Pinedo, E. O'Connor, A. Schwenk, H.-T. Janka, C. J. Horowitz, and K. Langanke, Phys. Rev. C **78**, 015806 (2008).

[109] J. Witti, H.-T. Janka, and K. Takahashi, Astron. Astrophys. **286**, 841 (1994).

[110] B. S. Meyer, Phys. Rep. **227**, 257 (1993).

[111] R. D. Hoffman, S. E. Woosley, and Y.-Z. Qian, Astrophys. J. **482**, 951 (1997).

[112] G. M. Fuller, and B. S. Meyer, Astrophys. J. **453**, 792 (1995).

[113] G. C. McLaughlin, G. M. Fuller, and J. R. Wilson, Astrophys. J. **472**, 440 (1996).

[114] A. B. Balantekin, and H. Yüksel, New J. Phys. **7**, 51 (2005).

[115] H. Duan, A. Friedland, G. C. McLaughlin, and R. Surman, J. Phys. G: Nucl. Phys. **38**, 035201 (2011).

[116] B. S. Meyer, Astrophys. J. Lett. **449**, L55 (1995).

[117] B. S. Meyer, G. C. McLaughlin, and G. M. Fuller, Phys. Rev. C **58**, 3696 (1998).

[118] K. Takahashi, J. Witti, and H.-T. Janka, Astron. Astrophys. **286**, 857 (1994).

[119] A. Arcones, and J. Bliss, J. Phys. G: Nucl. Phys. **41**, 044005 (2014).

[120] L. F. Roberts, S. E. Woosley, and R. D. Hoffman, Astrophys. J. **722**, 954 (2010).

[121] A. Arcones, and F. Montes, Astrophys. J. **731**, 5 (2011).

[122] R. D. Hoffman, B. Müller, and H.-T. Janka, Astrophys. J. Lett. **676**, L127 (2008).

[123] R. Buras, M. Rampp, H.-T. Janka, and K. Kifonidis, Astron. Astrophys. **447**, 1049 (2006).

[124] G. C. McLaughlin, J. M. Fetter, A. B. Balantekin, and G. M. Fuller, Phys. Rev. C **59**, 2873 (1999).

[125] I. Tamborra, G. G. Raffelt, L. Hüdepohl, and H.-T. Janka, JCAP **1**, 013 (2012).

[126] G. Martínez-Pinedo, T. Fischer, A. Lohs, and L. Huther, Phys. Rev. Lett. **109**, 251104 (2012).

[127] L. F. Roberts, Astrophys. J. **755**, 126 (2012).

[128] L. F. Roberts, S. Reddy, and G. Shen, Phys. Rev. C **86**, 065803 (2012).

[129] S. Wanajo, H.-T. Janka, and B. Müller, Astrophys. J. Lett. **726**, L15 (2011).

[130] M. Liebendörfer, A. Mezzacappa, O. E. B. Messer, G. Martínez-Pinedo, W. R. Hix, and F.-K. Thielemann, Nucl. Phys. A **719**, C144 (2003).

[131] J. Pruet, S. E. Woosley, R. Buras, H.-T. Janka, and R. D. Hoffman, Astrophys. J. **623**, 325 (2005).

[132] C. Fröhlich *et al.*, Astrophys. J. **637**, 415 (2006).

[133] S. Wanajo, H.-T. Janka, and S. Kubono, Astrophys. J. **729**, 46 (2011).

[134] A. Arcones, C. Fröhlich, and G. Martínez-Pinedo, Astrophys. J. **750**, 18 (2012).

[135] H.-T. Janka, and E. Müller, Astrophys. J. Lett. **448**, L109 (1995).

[136] H.-T. Janka, and E. Müller, Astron. Astrophys. **306**, 167 (1996).

[137] A. Burrows, J. Hayes, and B. A. Fryxell, Astrophys. J. **450**, 830 (1995).

[138] W. R. Hix, and F.-K. Thielemann, J. Comput. Appl. Math. **109**, 321 (1999).

[139] J. J. Cowan, F.-K. Thielemann, and J. W. Truran, (in preparation).

[140] A. Messiah, *Quantum Mechanics* (Dover Publications: New York, 1999).

[141] J. M. Blatt, and V. Weisskopf, *Theoretical Nuclear Physics* (Wiley: New York, 1952).

[142] W. A. Fowler, G. R. Caughlan, and B. A. Zimmerman, Annu. Rev. Astron. & Astrophys. **5**, 525 (1967).

[143] W. D. Arnett, and J. W. Truran, Astrophys. J. **157**, 339 (1969).

[144] R. V. Wagoner, Astrophys. J. **179**, 343 (1973).

[145] Intel, *Intel LAPACK*, `https://software.intel.com/en-us/node/520866` (2017).

[146] E. Müller, Astron. Astrophys. **162**, 103 (1986).

[147] E. Müller, *Computational Methods for Astrophysical Fluid Flow*, edited by A. G. O. Steiner (Springer-Verlag:Berlin, 1998) p. 343.

[148] Intel, *Intel MKL PARDISO*, `https://software.intel.com/en-us/node/470282` (2017).

[149] B. S. Meyer, T. D. Krishnan, and D. D. Clayton, Astrophys. J. **498**, 808 (1998).

[150] W. R. Hix, and B. S. Meyer, Nucl. Phys. A **777**, 188 (2006).

[151] D. D. Clayton, *Principles of stellar evolution and nucleosynthesis* (University of Chicago Press, 1983).

[152] F. E. Clifford, and R. J. Tayler, MmRAS **69**, 21 (1965).

[153] A. G. W. Cameron, Astrophys. J. Lett. **230**, L53 (1979).

[154] D. Hartmann, S. E. Woosley, and M. F. El Eid, Astrophys. J. **297**, 837 (1985).

[155] C. Winteler, *Light Element Production in the Big Bang and the Synthesis of Heavy Elements in 3D MHD Jets from Core-Collapse Supernovae*, Ph.D. thesis, Univ. Basel, CH (2012).

[156] C. Winteler, R. Käppeli, A. Perego, A. Arcones, N. Vasset, N. Nishimura, M. Liebendörfer, and F.-K. Thielemann, Astrophys. J. Lett. **750**, L22 (2012).

[157] R. H. Cyburt *et al.*, Astrophys. J. Suppl. Ser. **189**, 240 (2010).

[158] A. J. Koning, S. Hilaire, and S. Goriely, *Talys 1.6 user manual,* *`http://www.talys.eu/fileadmin/talys/user/docs/talys1.6.pdf`* (2013).

[159] T. Rauscher, *NON-SMOKER code,* *`https://nucastro.org/websmoker.html`*.

[160] R. Crowter, Ph.D. thesis, University of Surrey (2007).

[161] T. Mayer-Kuckuk, *Kernphysik* (Vieweg+Teubner Verlag, 2002).

[162] P. Mohr, Phys. Rev. C **94**, 035801 (2016).

[163] A. Kumar, S. Kailas, S. Rathi, and K. Mahata, Nucl. Phys. A **776**, 105 (2006).

[164] S. Watanabe, Nucl. Phys. A **8**, 484 (1958).

[165] L. McFadden, and G. Satchler, Nucl. Phys. **84**, 177 (1966).

[166] P. Demetriou, C. Grama, and S. Goriely, Nucl. Phys. A **707**, 253 (2002).

[167] A. Kobos, B. Brown, R. Lindsay, and G. Satchler, Nucl. Phys. A **425**, 205 (1984).

[168] J. Bliss, A. Arcones, F. Montes, and J. Pereira, J. Phys. G: Nucl. Phys. **44**, 054003 (2017).

[169] J. Bliss, M. Witt, A. Arcones, F. Montes, and J. Pereira, Astrophys. J. **855**, 135 (2018).

[170] L. F. Roberts, S. Reddy, and G. Shen, Phys. Rev. C **86**, 065803 (2012).

[171] B. D. Metzger, T. A. Thompson, and E. Quataert, Astrophys. J. **659**, 561 (2007).

[172] T. A. Thompson, Astrophys. J. Lett. **585**, L33 (2003).

[173] C. J. Hansen, M. Bergemann, G. Cescutti, P. François, A. Arcones, A. I. Karakas, K. Lind, and C. Chiappini, Astron. Astrophys. **551**, A57 (2013).

[174] S. Wanajo, Astrophys. J. Lett. **770**, L22 (2013).

[175] I. U. Roederer, G. W. Preston, I. B. Thompson, S. A. Shectman, and C. Sneden, Astrophys. J. **784**, 158 (2014).

[176] M. Witt, *The neutrino-driven wind: From steady-state models to hydrodynamic simulations*, Master's thesis, TU Darmstadt (2016).

[177] J. M. Lattimer, and F. D. Swesty, Nucl. Phys. A **535**, 331 (1991).

[178] H. Shen, H. Toki, K. Oyamatsu, and K. Sumiyoshi, Nucl. Phys. A **637**, 435 (1998).

[179] A. W. Steiner, M. Hempel, and T. Fischer, Astrophys. J. **774**, 17 (2013).

[180] J. M. Lattimer, and M. Prakash, Phys. Rep. **442**, 109 (2007).

[181] B. Müller, H.-T. Janka, and A. Marek, Astrophys. J. **756**, 84 (2012).

[182] K. Sumiyoshi, S. Yamada, and H. Suzuki, Astrophys. J. **667**, 382 (2007).

[183] T. Kuroda, S. Wanajo, and K. Nomoto, Astrophys. J. **672**, 1068-1078 (2008).

[184] I. V. Panov, and H.-T. Janka, Astron. Astrophys. **494**, 829 (2009).

[185] A. Arcones, and G. Martínez-Pinedo, Phys. Rev. C **83**, 045809 (2011).

[186] R. D. Hoffman, S. E. Woosley, G. M. Fuller, and B. S. Meyer, Astrophys. J. **460**, 478 (1996).

[187] D. Martin, A. Perego, A. Arcones, F.-K. Thielemann, O. Korobkin, and S. Rosswog, Astrophys. J. **813**, 2 (2015).

[188] T. Rauscher, and F.-K. Thielemann, At. Data Nucl. Data Tables **75**, 1 (2000).

[189] G. Audi, O. Bersillon, J. Blachot, and A. Wapstra, Nucl. Phys. A **729**, 3 (2003).

[190] P. Möller, J. R. Nix, W. D. Myers, and W. J. Swiatecki, At. Data Nucl. Data Tables **59**, 185 (1995).

[191] I. A. Rizvi, M. K. Bhardwaj, M. Afzal Ansari, and A. K. Chaubey, Can. J. Phys. **67**, 870 (1989).

[192] M. Ismail, Phys. Rev. C **41**, 87 (1990).

[193] C. Sneden, J. J. Cowan, and J. E. Lawler, Nucl. Phys. A **718**, 29 (2003).

[194] S. Honda, W. Aoki, Y. Ishimaru, and S. Wanajo, Astrophys. J. **666**, 1189 (2007).

[195] A. Parikh, J. José, F. Moreno, and C. Iliadis, Astrophys. J. Suppl. Ser. **178**, 110-136 (2008).

[196] M. S. Smith, W. R. Hix, S. Parete-Koon, L. Dessieux, M. W. Guidry, D. W. Bardayan, S. Starrfield, D. L. Smith, and A. Mezzacappa, in *Classical Nova Explosions*, American Institute of Physics Conference Series, Vol. 637, edited by M. Hernanz, and J. José (2002) pp. 161–166.

[197] W. R. Hix, M. S. Smith, S. Starrfield, A. Mezzacappa, and D. L. Smith, Nucl. Phys. A **718**, 620 (2003).

[198] T. Rauscher, N. Nishimura, R. Hirschi, G. Cescutti, A. S. J. Murphy, and A. Heger, Mon. Not. R. Astron. Soc. **463**, 4153 (2016).

[199] N. Nishimura, R. Hirschi, T. Rauscher, A. S. J. Murphy, and G. Cescutti, Mon. Not. R. Astron. Soc. **469**, 1752 (2017).

[200] M. Mumpower, R. Surman, G. McLaughlin, and A. Aprahamian, Prog. Part. Nucl. Phys. **86**, 86–126 (2016).

[201] M. R. Mumpower, G. C. McLaughlin, R. Surman, and A. W. Steiner, J. Phys. G: Nucl. Phys. **44**, 034003 (2017).

[202] R. Longland, C. Iliadis, A. E. Champagne, J. R. Newton, C. Ugalde, A. Coc, and R. Fitzgerald, Nucl. Phys. A **841**, 1 (2010).

[203] R. Longland, C. Iliadis, and A. I. Karakas, Phys. Rev. C **85**, 065809 (2012).

[204] C. Iliadis, R. Longland, A. Coc, F. X. Timmes, and A. E. Champagne, J. Phys. G: Nucl. Phys. **42**, 034007 (2015).

[205] R. Longland, Astron. Astrophys. **604**, A34 (2017).

[206] K. Pearson, Proceedings of the Royal Society of London **58**, 240 (1895).

[207] C. Spearman, AJP **15**, 72 (1904).

[208] A. Arcones *et al.*, Prog. Part. Nucl. Phys. **94**, 1 (2017).

Acknowledgements

Im Folgenden möchte ich mich bei allen bedanken, die mich während meiner Doktorandenzeit und bei der Erstellung dieser Arbeit unterstützt haben.

Mein ganz besonderer Dank gilt meiner Doktormutter Almudena Arcones für die Aufnahme in die Arbeitsgruppe vor mehr als vier Jahren, die Übertragung des spannenden Forschungsthemas, die vielen anregenden Diskussionen, Ratschläge und die Unterstützung in vielen Gesprächen und E-Mails. Außerdem möchte ich Danke sagen, dass ich in internationalen Kollaborationen arbeiten durfte. Ich möchte mich auch für die Teilnahme an so vielen Konferenzen, Workshops und Schools bedanken.

Ich möchte mich bei Hendrik Schatz für die Übernahme des Zweitgutachtens sowie die Möglichkeit, die Michigan State University für zwei Forschungsaufenthalte zu besuchen, bedanken. Vielen Dank für die anregenden Gespräche während meiner Zeit an der MSU.

I want to say thank you to my collaborators Fernando Montes and Jorge Pereira for inspiring and fruitful discussions. I learned a lot in the collaboration with you. Thank you that I could visit you twice at MSU. It was a very productive time there.

Ich möchte mich bei allen derzeitigen und früheren Mitgliedern der Astrogruppe bedanken: Almudena Arcones, Marius Eichler, Camilla Juul Hansen, Takami Kuroda, Dirk Martin, Carlos Mattes, Paul Mekhedjian, Albino Perego, Moritz Reichert, Marcella Ugliano, Maximilian Witt und Hannah Yasin. Vielen Dank für die vielen fachlichen Gespräche sowie die schönen und unterhaltsamen Momente sowohl während der Arbeitszeit also auch während der Freizeitaktivitäten.

Außerdem möchte ich mich bei den Büros Nummer 1 und 302 für die angenehme Arbeitsatmosphäre bedanken. Herzlichen Dank Camilla, Carlos, Dirk, Hannah, Marc, Moritz, Sandra und Takami.

Thank you to Almudena, Dirk, Fernando, Jorge, Max, Moritz, and Takami for partial proof reading of this thesis. A special thank goes to Almudena and Dirk who read everything.

Ein ganz besonderer Dank geht an Alexander für die moralische Unterstützung und die nötige Ablenkung während meines Studiums und meiner Doktorandenzeit. Es ist unglaublich, wieviel Verständnis du in den letzten Wochen für mich hattest.

Ich möchte meinen Eltern und meiner Familie für die Unterstützung während meines Studiums und der Doktorandenzeit ganz herzlich danken.

Diese Arbeit wurde durch den Helmholtz-University Young Investigator Grant Nr. VH-NG-825 und den SFB 1245 unterstützt. I want to thank JINA-CEE for two research stays at the Michigan State University and the possibility to participate in the TALENT course ”Nuclear theory for astrophysics“. Darüber hinaus danke ich der Graduiertenschule MGK des SFB 1245 für das ”Theory Internship“. Außerdem war ich Mitglied in der HGS-HIRe Graduiertenschule, die mir die Teilnahme an Konferenzen und Softskill-Kursen ermöglicht hat. Ich bedanke mich bei NAVI für die Unterstützung zur Teilnahme an der Konferenz ”Nuclear Physics in Astrophysics VII“ und der Wilhelm-und-Else-Heraeus-Stiftung für die Bezuschussung der Teilnahmegebühren für die DPG Frühjahrstagungen und der Konferenz ”Nuclei in the Cosmos XII“.

Sämtliche Nukleosyntheseberechnungen wurden auf dem alten Cluster ”Prometheus“ und auf dem neuen Cluster ”Kronos“ an der GSI durchgeführt. Die (α, n) Reaktionsraten wurden mit dem TALYS 1.6 Code berechnet.

Curriculum Vitae

Julia Barbara Erika Bliss

August 10th, 1988	Born in Offenbach am Main, Germany
June 4th, 2008	Abitur, Otto-Hahn-Schule Hanau, Germany
2008 – 2012	Bachelor studies, TU Darmstadt, Germany
January 13th, 2012	Bachelor’s degree, thesis title: ”Konstruktion eines adaptiven Bremstargets für DHIPS“
2012 – 2014	Master studies, TU Darmstadt, Germany
February 19th, 2014	Master’s degree, thesis title: ”Nucleosynthesis in neutrino-driven winds“
2014 – 2017	Doctoral studies and member of the scientific staff, TU Darmstadt, Germany

Erklärung zur Dissertation

Hiermit versichere ich, die vorliegende Dissertation ohne Hilfe Dritter nur mit den angegebenen Quellen und Hilfsmitteln angefertigt zu haben. Alle Stellen, die aus Quellen entnommen wurden, sind als solche kenntlich gemacht. Diese Arbeit hat in gleicher oder ähnlicher Form noch keiner Prüfungsbehörde vorgelegen. Eine Promotion wurde bisher noch nicht versucht.

Darmstadt, den 1. August 2018

(Julia Bliss)